The Impact of the Snow-Darkening Effect on Snow Cover and the Atmosphere During a Major Dust Event Across Eurasia

Zur Erlangung des akademischen Grades einer

DOKTORIN DER NATURWISSENSCHAFTEN

von der KIT-Fakultät für

Bauingenieur-, Geo- und Umweltwissenschaften

des Karlsruher Instituts für Technologie (KIT)

genehmigte

DISSERTATION

von

M. Sc. Anika Rohde

aus Lörrach

Tag der mündlichen Prüfung:	07.05.2021
Referent:	Prof. Dr. Jan Cermak
Korreferent:	Prof. Dr. Christoph Kottmeier

Karlsruhe 2021

Abstract

The surface of snow has a high ratio of scattered to incident shortwave radiation, the so-called snow albedo. However, several processes strongly affect the snow albedo, resulting in high temporal and spatial variability. Models mostly use strong simplifications of the snow albedo, which introduce many uncertainties. One of the processes modifying the albedo is the deposition of mineral dust on snow. Since the albedo is embedded in the radiation budget of the earths surface, the perturbation of the mineral dust creates a feedback with the snow cover and in the atmosphere. In order to investigate this impact, the model system ICON-ART was extended by a parametrization of a spectral snow albedo that considers snow aging processes and the snow-darkening effect of mineral dust.

The aging of snow was evaluated using the optical equivalent snow grain size and the new spectral albedo against observations in Greenland. The spectral albedo has been shown to vary by several percent with atmospheric conditions over the course of the day. In addition, it was observed that aging strongly depends on snow temperature. Therefore, the parametrization was extended to include arctic conditions. The final parametrization of the snow metamorphism leads to a simulation of the optical grain size which is in agreement with the measurements. The modeled snow albedo is consistent with observations during cloudy days in Greenland, but an overestimation of the clear-sky albedo is observed.

The influence of mineral dust on snow albedo was investigated using the new model developments in a simulation of a large dust deposition event in spring 2018. The study area covers large parts of Europe and the western parts of Asia. Ten days from March 22, 2018 were simulated in the ICON-LAM setting at a horizontal resolution of 10 km.

An ensemble simulation with a total of 80 members was generated. It was found that the snow-darkening effect develops gradually and is overlaid by natural variability. In this context, the change in cloud cover plays a major role in determining the feedback as radiative forcing at the surface. The reduction in snow depth is veiled by the changes in snowfall patterns, whereas the feedback in surface temperature and 2m-temperature are masked by shifts of large-scale weather systems. Averaging over the ensemble and a significance analysis considerably assists in separating signals from mineral dust from the influence of natural variability.

Mainly mountainous regions turned out to be susceptible to the darkening effect. But also flat areas showed strong effects at the snow line despite lower concentrations. It was found that the snow cover fraction plays an important role in this context. In the Caucasus Mountains, where the snow pack is usually dense, the feedback manifests itself as increased snow melt. The correlation found here indicates

that a reduction in surface albedo by $-2.83\,\%$ is associated with a mean reduction in snow depth by $-1.36\,\mathrm{cm}$ on the eighth simulation day. Along the snow line, however, the feedback to mineral dust deposition is evident not only in the snow depth, but primarily in the warming of the surface. Here, a warming by $0.92\,\mathrm{K}$ is connected to a reduction in surface albedo by $-4.50\,\%$. On average, a surface albedo reduction by $-2.93\,\%$ is expected to result in a surface radiative forcing of $19.15\,\mathrm{W\,m^{-2}}$. This study shows that the feedback to mineral dust deposition on snow depends on several factors. Primarily, these are namely altitude, slope, snow depth, and snow cover fraction. Surface temperature responds most strongly to mineral dust at lower elevations, where the snow pack is still patchy and thin. At higher elevations, it is mainly the snow depth that responds to the albedo perturbation. Thus, the snow-darkening effect is case-dependent and the above-mentioned aspects must be taken into account.

Kurzfassung

Die Oberfläche von Schnee hat ein hohes Verhältnis von gestreuter zu einfallender kurzwelliger Strahlung. Allerdings beeinflussen verschiedene Einflüsse die sogenannte Schneealbedo erheblich. Modelle verwenden meist starke Vereinfachungen der Schneealbedo, die viele Unsicherheiten mit sich bringen. Einer der Prozesse, die auf die Albedo einwirken, ist die Ablagerung von Mineralstaub auf Schnee. Die Störung des Staubs erzeugt Rückkopplungen in der Schneedecke und in der Atmosphäre. Zur Untersuchung diesen Einflusses, wurde das Modellsystem ICON-ART um eine Parametrisierung einer spektralen Schneealbedo erweitert, die Alterungsprozesse des Schnees und den Verdunklungseffekt des Mineralstaubs berücksichtigt.

Die Alterung von Schnee wurde mittels der optisch äquivalenten Schneekorngröße, sowie der neuen spektralen Albedo anhand von Beobachtungen in Grönland ausgewertet. Es hat sich gezeigt, dass die spektrale Albedo mit den atmosphärischen Bedingungen im Tagesverlauf um mehrere Prozent variiert und dass die Alterung stark von der Schneetemperatur abhängt. Daher wurde die Parametrisierung dahingehend ergänzt, dass arktische Bedingungen ebenfalls berücksichtigt werden. Die resultierende Parametrisierung der Schneealterung ermöglicht die Simulation der optischen Schneekorngröße, die sich weitgehend mit den Messungen deckt. Die modellierte Schneealbedo stimmt mit den Beobachtungen an bewölkten Tagen in Grönland überein, aber es wird eine Überschätzung der Albedo bei klarem Himmel beobachtet.

Der Einfluss von Mineralstaub auf die Schneealbedo wurde mit den neuen Modellentwicklungen in einer Simulation eines großen Staubdepositionsereignisses im Frühjahr 2018 untersucht. Das Untersuchungsgebiet umfasst große Teile Europas und die westlichen Teile Asiens. Zehn Tage vom 22. März 2018 wurden in der ICON-LAM Konfiguration mit einer horizontalen Auflösung von 10 km simuliert. Es wurde eine Ensemble-Simulation mit einer Anzahl von 80 Mitgliedern generiert. Es wurde festgestellt, dass sich der Verdunklungseffekt sukzessiv entwickelt und von Einflüssen der natürlichen Variabilität überlagert wird. In diesem Zusammenhang interferieren modifizierte Wolkenmuster mit der Quantifizierung des Strahlungsantriebs an der Oberfläche, Änderungen der Niederschlagsmuster bei der Ermittlung des Einflusses auf die Schneehöhe und Verlagerungen großräumiger Wettersysteme bei der Untersuchung des Einflusses auf die Oberflächentemperatur und 2m-Temperatur. Die Mittelung über das Ensemble und eine Signifikanzanalyse hilft maßgeblich dabei, Signale des Mineralstaubs von dem Einfluss der natürlichen Variabilität zu trennen.

Hauptsächlich haben sich Gebiete in Gebirgen sowie flache Gebiete entlang der Schneegrenze als anfällig für den Verdunklungseffekt herausgestellt. Im Kaukasusgebirge manifestiert sich die Rückkopplung als verstärkte Schneeschmelze. Die hier gefundene Korrelation zeigt, dass am achten Simulationstag eine Reduktion der Oberflächenalbedo von $-2.83\,\%$ mit einer mittleren Reduktion der Schneehöhe um $-1.36\,\mathrm{cm}$ verbunden ist. Entlang der Schneegrenze zeigt sich die Rückkopplung auf die

Mineralstaubablagerung vor allem in der Erwärmung der Oberfläche. Hier ist eine Erwärmung um 0.92 K an eine Verringerung der Oberflächenalbedo um $-4.50\,\%$ gekoppelt. Im Mittel ist bei einer Verringerung der Oberflächenalbedo um $-2.93\,\%$ ein Strahlungsantrieb von $19.15\,\mathrm{W\,m^{-2}}$ an der Oberfläche zu erwarten. Diese Studie zeigt, dass die Rückkopplung auf den Einfluss der Mineralstaubablagerung auf Schnee von der Höhe, Ausrichtung des Hangs, Schneehöhe und dem Schneebedeckungsgrad abhängig ist. Die Oberflächentemperatur reagiert in niedrigeren Lagen am stärksten auf Mineralstaub, wo die Schneedecke noch lückenhaft und dünn ist. In höher gelegenen Gebieten wirkt sich die Albedoreduktion hauptsächlich auf die Schneehöhe aus.

Contents

1 Introduction: The Optical Properties of Snow

The surface albedo describes the relation of scattered to incident shortwave radiation. Therefore, it plays a significant role in the energy budget of the earth. Snow covered surfaces are characterized by exceptionally high albedo and therefore reduce the absorption and heating. In the visible spectrum, the albedo of pure snow is roughly 96–99 % (Wiscombe and Warren, 1980). The major features that determine the optical properties of snow are the snow micro-structure, snow depth, and the content of impurities.

Wiscombe and Warren (1980) were the first to introduce a model for the spectral albedo of snow. It shows that the snow albedo is highly variable over the shortwave spectrum. The reason for this behavior is the high spectral variability of shortwave radiation absorption of ice. In the shorter wavelengths, namely the visible range, ice behaves like a strong reflector but becomes more absorbent towards the infrared range. Fig. 1.1 shows a comparison of the proposed snow albedo model with measurements from O'Brien and Munis (1975).

1.1 Light-Absorbing Impurities in Snow

A contributing factor that has only recently become the focus of attention is the presence of impurities in snow (e.g., Wiscombe and Warren, 1980; Kuhn et al., 1997; Hansen and Nazarenko, 2004; Jacobson, 2004; Hansen, 2005; Flanner and Zender, 2005; Aoki et al., 2006; Flanner et al., 2009; Skeie et al., 2011; Bond et al., 2013; Meinander et al., 2013; Yasunari et al., 2013; Dumont et al., 2014; Peltoniemi et al., 2015; Yasunari et al., 2015; Svensson et al., 2016; Heintzenberg and Rummukainen, 2017; Tuzet et al., 2017; Skiles et al., 2018a,b; Zhang et al., 2018; Lau et al., 2018; Di Mauro et al., 2019; He et al., 2019; Jacobi et al., 2019; Marmureanu et al., 2019; Nagorski et al., 2019; Sarangi et al., 2019; Tuzet et al., 2019; Barkan and Alpert, 2020; Donth et al., 2020; Dumont et al., 2020; Rahimi et al., 2020; Sarangi et al., 2020; Shi et al., 2021; Usha et al., 2020). These light-absorbing impurities are mostly aerosols which either originate from the close surroundings or are transported over long distances via the atmosphere. These aerosols can have different compositions depending on their origin.

The current knowledge about the properties of snow albedo and how impurities interact with them is well summarized by Skiles and Painter (2018). Fig. 1.2 shows the basic understanding of the impact of aerosols on the snow albedo. It is necessary to distinguish between different states of the snow. Fresh snow has a very high albedo and therefore reflects almost all of the incoming solar radiation. Aged snow has less reflective properties, but still reflects most of the radiation. The given numbers in Fig. 1.2 serve only as examples and the transition between the albedo of new snow and old snow is seamless and dependent on various factors. When aerosols, also called light-absorbing impurities (LAI), come into play, the albedo is reduced according to the optical properties of the particular type of aerosol, because

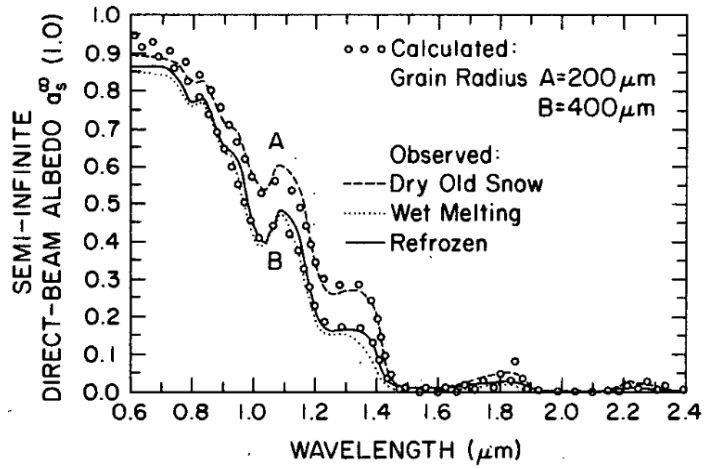

Figure 1.1: Computed spectral snow albedo for different grain sizes compared to measurements by O'Brien and Munis (1975) (adapted from Wiscombe and Warren, 1980).

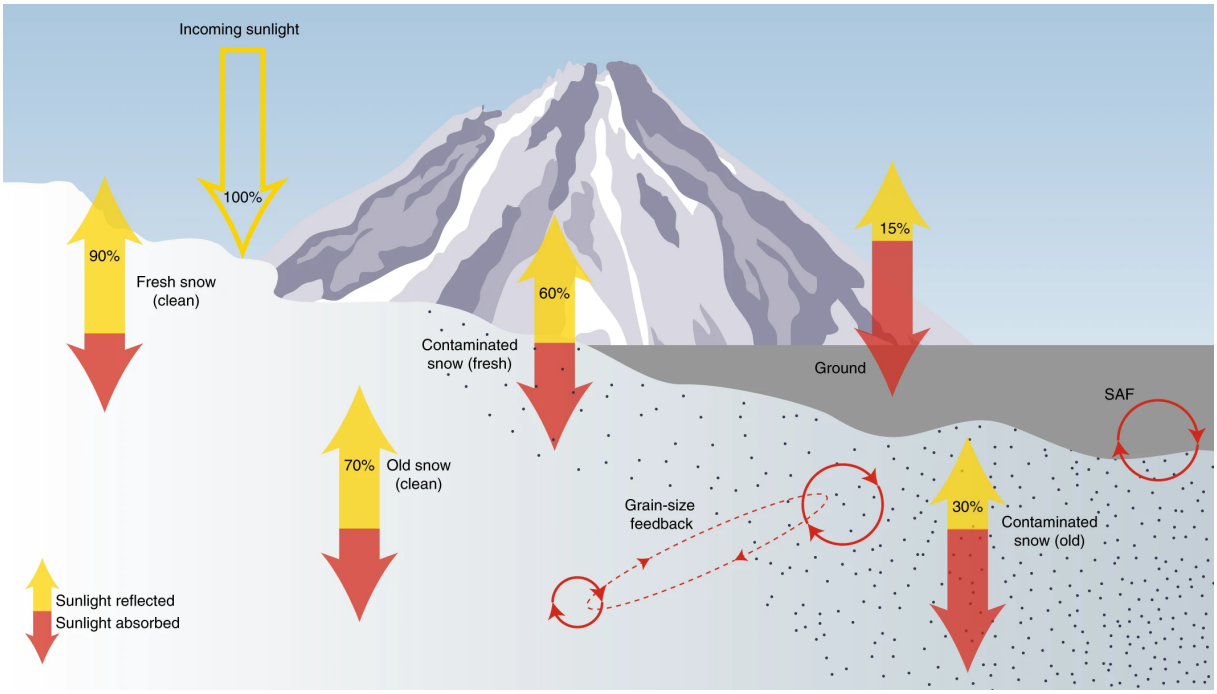

Figure 1.2: Diagram of the influence of snow albedo on shortwave radiation fluxes and interactions with light-absorbing impurities (adapted from Skiles et al., 2018a).

the particles absorb additional solar radiation. Thereby, the reduction of the albedo is larger for already aged snow. With this initial disturbance caused by aerosol in snow, further feedback develops between the two components. The age of the snow is described by the grain size. The grain size of new snow is small and with increasing age the grain size becomes larger. The impurities in the snow heat up more than the snow surrounding them, driving the temperature-dependent aging of the snow. This feedback is called indirect effect or grain-size feedback. There is another feedback also known as snow albedo effect (SAF), which is the lowering of the landscape-scale albedo. The ground beneath the snow cover is usually darker than the snow itself and absorbs more solar radiation in comparison. The reduction in snow albedo causes the snow to melt faster, which results in the ground emerging to the surface earlier in the season. This also results in a further reduction of the albedo, especially when examined from a temporal point of view.

As already mentioned, the snow albedo is spectrally highly variable. It is important to note that the LAI interact with a very specific wavelength region. Fig. 1.3 shows the change in spectral albedo with the concentration of impurities (a), the change in spectral albedo with the age of the snow (b), and the measured change in spectral albedo where both processes are present (c). On the one hand, the impurities mainly influence the very shortwave range, respectively the range of visible radiation. There, the albedo and the spectral radiation flux are at their highest and therefore the impact in this region is particularly significant. The age of the snow, on the other hand, mainly changes the signature in the near infrared. The measurements show that both processes are involved in the evolution of the optical properties of the snow. Therefore, it is important that both of these processes are taken into account.

The most frequently discussed aerosol is black carbon (BC). Due to the dark color it has the strongest impact on the snow properties. However, there are also natural aerosols that can strongly influence the snow albedo. Examples for these natural aerosols are volcanic ash, algae, microbes, and organic debris. Mineral dust takes a very special position, as it is one of the most abundant aerosols in the atmosphere. In many regions mountain ranges are located in proximity to arid regions, like deserts, which are the main source of mineral dust. Observations of mineral dust on snow surfaces have been documented for a long time. When snow falls and carries dust particles, the snow fall appears red which was being described as "blood rains" already in medieval times (White et al., 2012). Several studies showed that mineral dust transported to several regions (e.g., central asia mountains, Colorado in the U.S.) outweigh BC because of its great abundance (Painter et al., 2010; Gautam et al., 2013; Kaspari et al., 2014; Yasunari et al., 2015; Svensson et al., 2018). Furthermore, Sarangi et al. (2020) demonstrated that with altitude the impact of dust increases relative to the impact of BC. Since snow melt in high mountains often provides the water supply for many people, the timing and amount of melt water runoff is of great importance to the environment and residents throughout the catchment. Due to the disturbance through the aerosols this timing and amount can change significantly since snow melts out earlier in spring time (Fujita, 2007; Painter et al., 2010; Bryant et al., 2013; Deems et al., 2013; Skiles et al., 2015). Furthermore, the aerosols on snow and ice play an important role regarding the melting of glaciers, one of the most vulnerable components of our ecosystem (Xu et al., 2009; Gabbi et al., 2015; Li et al., 2017). As the awareness of the importance of aerosols on snow grew, efforts to study and quantify their influence with measurements and modeling increased.

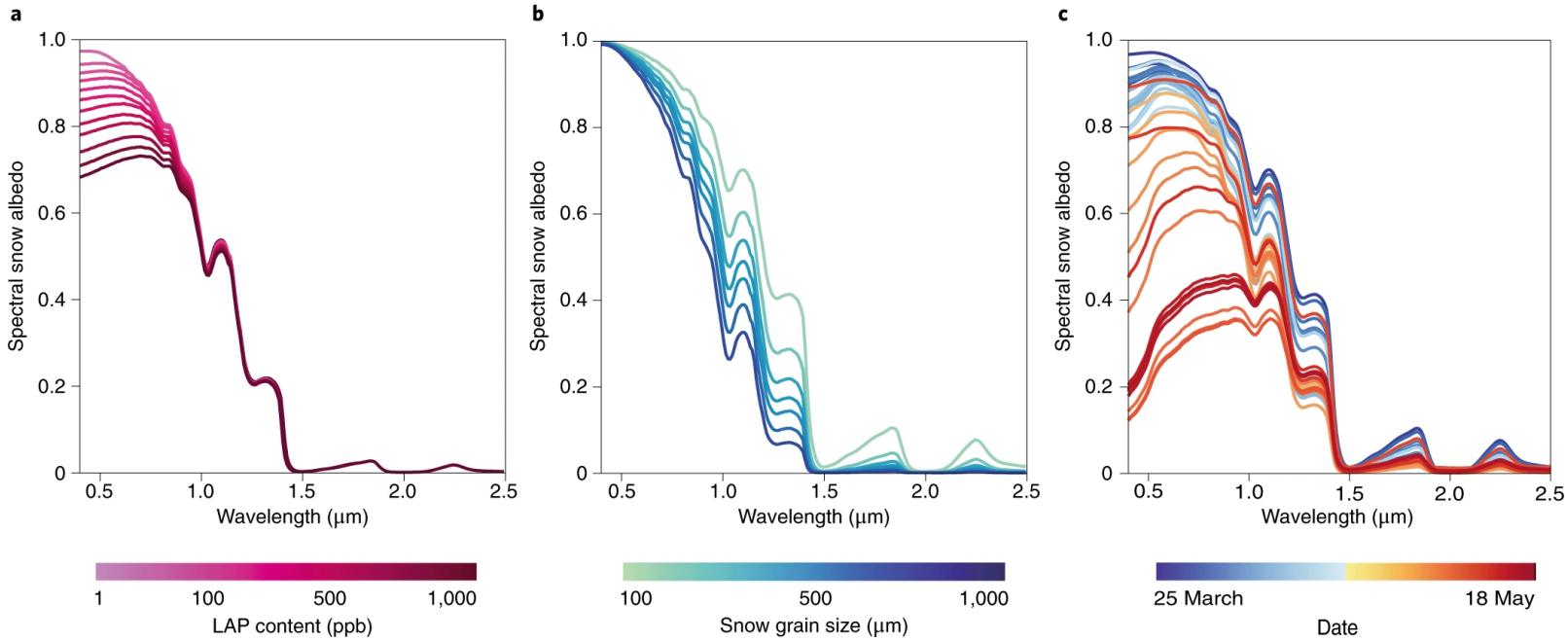

Figure 1.3: Spectral snow albedo with varying content of LAI, here denoted as LAP (a). Spectral snow albedo of different states of snow age described by the snow grain size (b). Daily time series of measurements showing the combined effect of impurities and aging on the spectral snow albedo (c) (adapted from Skiles et al., 2018a).

1.2 Previous Measurements

In order to examine the influence of aerosols on snow, it is essential to understand the optical properties of the snow itself and the contribution of aging. There are some studies about the aging of snow which is known as the snow metamorphism (e.g., Aoki et al., 2003; Domine et al., 2003; Schneebeli and Sokratov, 2004; Kaempfer and Schneebeli, 2007; Pinzer and Schneebeli, 2009; Slaughter et al., 2011; Ebner et al., 2016; Linow et al., 2017). Kaempfer and Schneebeli (2007), for example, found that there is a strong temperature dependence of the speed of metamorphism. In their laboratory experiments they observed that isothermal growth almost completely ceases at temperatures below $-54\,°C$. However, the metamorphism in the natural environment appears to be quite more difficult to determine. A separation must be made between wet and dry metamorphism since wet snow ages much faster than dry snow (Brun, 1989; Aoki et al., 2003; Lehning et al., 2002a). The term "wet" refers to the presence of a greater proportion of liquid water in the snow, which is usually the case when the temperature is above the melting point.

Moreover, there are also measurements that include the influence of aerosols on snow (e.g., Aoki et al., 2003; Negi et al., 2010; Hagenmuller et al., 2019). An exceptional study was carried out by Svensson et al. (2016), as they tried to apply different aerosols in the field and measure the change of albedo under natural conditions. The experiments were carried out in Finland and the project turned out to be relatively complicated. The main difficulty was the uniform spreading of the aerosols, for which they needed several attempts and tested different methods. In the end, they succeeded by using a custom made cylindrical chamber into which the aerosol particles were blown. Furthermore, they were confronted with a snowstorm during one experiment, which blew out the aerosols before the first measurement could be performed and the test area was covered with fresh snow. Hence, most measurements take place in the laboratory rather than in the outdoor landscape. By their method, however, Svensson et al. found that the measurements in the field show a smaller effect of soot on snow albedo compared to laboratory measurements. Another important finding of their outdoor measurements is that the albedo may increase abruptly after deposition of the soot, due to the sinking of the aerosols into the snow layer. This process occurs especially when the ambient temperature is above the melting point. This observation was also noted by Peltoniemi et al. (2015), who suggests that this process poses a difficulty for remote sensing methods. When the aerosols sink, they are still visible in the nadir through the sink holes. However, if the snow is examined at a lateral angle, the albedo of the snow is considerably higher.

Nevertheless, there are attempts to study the process of snow albedo reduction by aerosols via remote sensing (e.g., Gautam et al., 2013; Warren, 2013; Lee et al., 2016; Di Mauro et al., 2015). Often, the aerosol optical depth (AOD) is used to identify the presence of aerosols. Attempts are then made to find a correlation between AOD and the reduction of albedo. For example, Lee et al. (2016) performed a statistical analysis concerning the Himalayan region and found a correlation of the AOD with the deposition of dust and BC of about 0.5. However, as they state, this type of analysis holds uncertainties since the presence of aerosols does not necessarily mean that they will be deposited at this exact location. Furthermore, Lee et al. explain that the correlation that they have found does not imply that there is actually a causal relationship between the quantities.

Another common method is the investigation of the seasonal variation in spectral surface reflectance. Thereby, one focuses on the wavelengths in the visible range whereas the signal of the near infrared range ($> 1\,\mu m$) is considered to determine the influence by snow aging. Applying this method Gautam et al. (2013) investigated the gradient of the surface reflectance between visible and near infrared (0.47–0.86 µm) and found a gradient of about $-9\,\%$ during a dust outbreak in the Himalaya. They also discovered that a dust layer in the atmosphere above snow can reduce the top-of-atmosphere reflectance which they associate with the more frequent scattering and eventually enhanced absorption of shortwave radiation in the aerosol layer. Unfortunately this method is only a qualitative rather than a quantitative investigation. An estimate of the aerosol concentration can be obtained by further comparing the measurements to results of a bidirectional reflectance distribution function model, such as proposed by Kokhanovsky and Breon (2012). These models can estimate the signal that the satellite receives over snow surfaces under the assumption of the refractive index of the suspected impurity and different concentrations of the aerosol. However, the analysis of the aerosol impact on the snow albedo via satellites is limited because influences of the ground in patchy snow distort the results. This is why in many researches only snow pixel with a snow coverage close to unity are considered (e.g., Gautam et al., 2013; Lee et al., 2016). Some other sources of error can be the complex terrain effects, for example when the reflection of a flat surface is assumed by the satellite (Gautam et al., 2013).

Furthermore, Warren (2013) explains that the study of soot on snow comes with further uncertainties even with closed snow cover. The spectral signature of thin snow where the underlying ground shines through has a very similar signature to that of the deposition of impurities on the snow. Since the soot is usually present in small amounts, it cannot be easily detected by satellites. Estimating whether the impact is coming from the subsurface is usually not trivial, since the height of the snow pack is spatially quite variable and the snow pack is often not completely packed. Additional information is needed to determine whether the darkening of the snow albedo is actually caused by aerosols. Fig. 1.4 shows a typical situation in which especially wind drift causes a patchy snow cover and ground influences can be mistaken for impurities in the snow. Models can be helpful in determining if there is a deposition or if the snow pack is rather thin. Specifically, they can determine at which location and at which time the signal is more likely to originate from the aerosols, for instance during a predicted deposition event. In addition to that, models can help to identify what type of aerosol is involved, which is difficult for satellites to distinguish.

Figure 1.4: Thin and patchy snow cover in northeast Siberia (south of Tiksi) in early April 2008, about one month before the maximum snow depth (adapted from Doherty et al., 2010).

1.3 Previous Model Studies

One of the first attempts to quantify the impact of impurities on the snow albedo using a climate model is the study conducted by Hansen and Nazarenko (2004). They generally decreased the albedo in the Goddard Institute for Space Studies (GISS) climate Model (modelE) to investigate the impact of BC on snow. The mean decrease of albedo in their climate simulations was 1.5 % in the Arctic and 3 % in the Northern Hemisphere land snow resulting in a Northern Hemisphere radiative forcing of $0.3\,\mathrm{W\,m^{-2}}$. Further climate simulations were carried out, for example by Jacobson (2004), who used the Gas, Aerosol, Transport, Radiation, General-Circulation, Mesoscale, and Ocean Model (GATOR-GCMOM) to simulate time-dependent spectral snow albedo with a radiative transfer solution at a horizontal resolution of 4° S–N × 5° W–E. He treated BC and organic matter in his simulation and found an global average increase of near-surface temperature of 0.27 K in 10 years. The global reduction of albedo was ~ 0.4 % and 1 % in the Northern Hemisphere.

In a more recent study Lau et al. (2018) used the National Aeronautics and Space Administration (NASA) Goddard Earth Observing System, Version 5 (GEOS-5) climate model to simulate the impact of LAI on the Eurasian continent at a horizontal resolution of $2° \times 2.5°$ latitude-longitude. The impact of dust, BC, and organic carbon (OC) on snow was evaluated based on anomaly fields resulting of the comparison of 10 ensemble members (each 10 years) mean climatology. This included 10 members who considered the influence of aerosols on snow and 10 members who did not. They found an annual mean increase in surface skin temperature which is most pronounced in Western Eurasia, East Asia, and the Tibetan

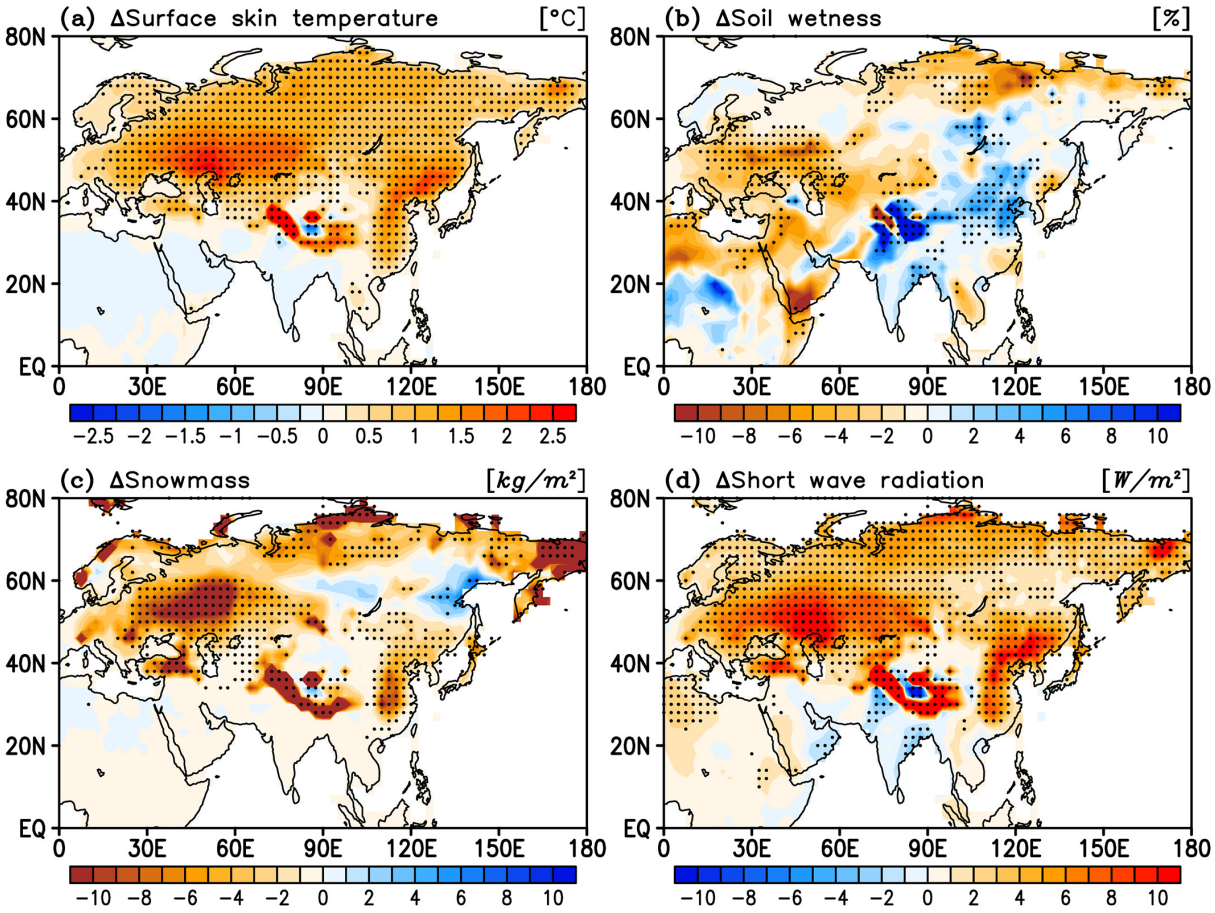

Figure 1.5: Annual mean climate anomaly in surface skin temperature (a), soil wetness (b), snowmass (c), and shortwave radiation (d) in Eurasia due to deposition of dust, BC, and OC (adapted from Lau et al., 2018).

Plateau where the difference is greater than 2 K (Fig. 1.5). The reduction in snow mass and the increase in shortwave radiation coincides well with these most heated regions. There is also a decrease in soil wetness, however, an increase is reported over India, China, and Southern Russia.

Lau et al. further observed a connection between changes in the hydroclimate and the deposition of LAI on snow, which they call the wet-first-dry-later modulation. A scheme is shown in Fig. 1.6. At the end of winter, due to earlier onset of snow melt, there is more runoff and the soil moisture content is higher. In late spring, soil warming and drought sets in and continues into summer. This promotes the formation of an atmospheric blocking, which leads to a dry and warm boreal summer. The result is an increased number of very hot days over Western and Northern Eurasia, with a tenfold increase in the number of top 1 % hottest days.

Higher resolution simulations over shorter time periods were also carried out with models to investigate the regional impacts. One example is the study carried out by Qian et al. (2009) using the Weather Research and Forecasting Chemistry model (WRF-Chem) and the National Emissions Inventory 1999. They focused on the impact of soot in a simulation of the Western United States at a grid spacing of 15 km along a year. One major finding of this study is that about half of the decrease in albedo is actually caused by the snow albedo. The other half can be accounted for by the disappearance of the complete snow pack caused by enhanced absorption of solar energy due to the lower snow albedo and revealing the even

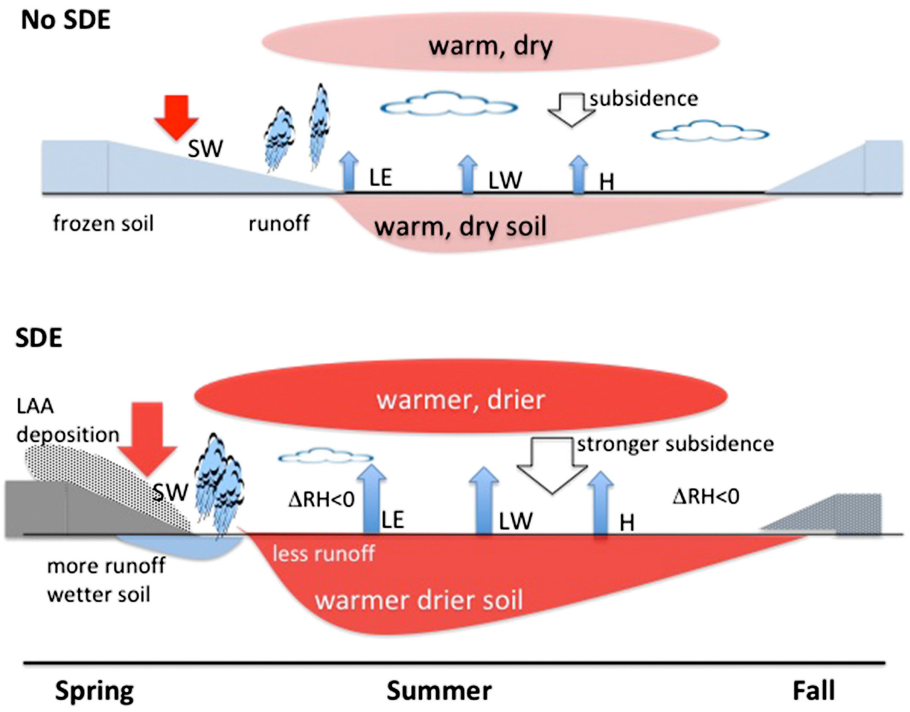

Figure 1.6: Wet-first-dry-later hydroclimate feedback mechanism on the Eurasian continent due to the snow-darkening effect by aerosols (adapted from Lau et al., 2018).

darker surface below the snow cover. The increase of net solar radiation flux due to the soot depositions is about 2–12 $\mathrm{W\,m^{-2}}$ in the study. The 2m-temperature increased 0.2 °C–1.4 °C. They also noted that the horizontal distribution is very heterogeneous and that the soot induced snow albedo perturbation is rather a regional effect and therefore greater uncertainties are to be expected with a coarser model resolution.

Flanner and Zender introduced the two-stream, multi-layer SNow, ICe, and Aerosol Radiation (SNICAR) model in 2005 which was thereafter used in many studies (e.g., Flanner et al., 2007, 2009, 2012; Kaspari et al., 2014; Zhao et al., 2014; Wu et al., 2018; Zhong et al., 2017; Nagorski et al., 2019; Sarangi et al., 2019). Coupled to a general circulation model, SNICAR calculates the snow albedo based on snow grain size and the theory of Wiscombe and Warren (1980) in one visible and four near-infrared bands. The optical properties of light-absorbing impurities were included to investigate the climate forcing of aerosols on snow (Flanner et al., 2007).

There are several studies that include highly sophisticated unidimensional snow pack models like the French snow model Crocus (Brun et al., 1992; Vionnet et al., 2012) or the Swiss model SNOWPACK (Lehning et al., 1999; Bartelt and Lehning, 2002; Lehning et al., 2002b,a). These snow schemes resolve multiple layers of snow and compute mass and energy exchange between the snow, the ground, and the atmosphere. Both of these models include a detailed parametrization of the snow metamorphism including shapes and sizes of the snow grains. SNOWPACK becomes a powerful tool when coupled with SNICAR. The coupling enables the simulation of radiative changes due to the impurities in snow and the detailed assessment of the effects on the snow cover energy balance.

For example, Skiles and Painter (2019) used this setup to simulate a snow cover in the San Juan Mountains in Colorado in spring to study the influence of dust on snow melt. They extended the model

with the ability to track the dust concentration in the snow to provide a dust stratification. In that sense, dust aerosols can reappear and concentrate at the surface when the snow layer melts. They performed two simulations of the snow pack where they used meteorological forcing data and assumed clean snow while the other simulation incorporated measured dust concentrations in snow. At model initialization, only small amounts of dust were present in the snow pack, but on four deposition events, these measured amounts of dust were added to the first snow layer. Skiles and Painter found an average daily mean radiative forcing of $30\,\mathrm{W\,m^{-2}}$ which varied between 2 and $109\,\mathrm{W\,m^{-2}}$. They considered not only the direct radiative impact which is caused by the dust, but also the indirect radiative effect which arises from the accelerated snow metamorphism triggered by the direct radiative effect. The indirect radiative effect reached a fraction of 20 % of the total radiative impact which is comparable to former studies (Tuzet et al., 2017). The change in snow albedo was quite low in the first half of the simulation with a reduction of 3 % in the dust scenario. However, as soon as melting commenced and aerosols resurfaced, the snow albedo dropped immensely resulting in a difference of 44 % between the two scenarios. The resulting radiative forcing lead to an advanced snow melt by 30 days. This study underlines the importance of a stratification of the aerosols in snow and the significant role that aerosols play in the process of snow melt in spring.

Similar capabilities come with the snow model Crocus which incorporates the Two-stream Analytical Radiative TransfEr in Snow model (TARTES) (Libois et al., 2013) that allows the model to simulate the radiative impact of LAI in snow. Dumont et al. (2020) used Crocus to investigate the impact of aerosols on the melting of snow during a major Saharan dust deposition event in the Russian Caucasus Mountains. They obtained Sentinel-2 reflectance data and compared them to a multitude of TARTES albedo simulations including different concentrations of aerosols in snow. In this manner they estimated the dust concentrations in the satellite pictures and used these aerosol concentrations as well as some in-situ measurements to evaluate the Crocus simulations. The aim of the study was to capture the snow pack evolution with and without the impact of aerosols and therefore the simulation was run from 1 June 2017 to 1 June 2018 for 4 different locations. Dust was deposited at a small constant rate whereas the dust event scenarios had one additional deposition on 23 March 2018. They found that depending on dust concentration, snow layer height, and altitude, the snow melt out advanced between 12–30 days. The daily averaged radiative forcing reached almost $35\,\mathrm{W\,m^{-2}}$ which is in the same range as the findings of (Skiles and Painter, 2019). Dumont et al. pointed out that the impact is more pronounced at higher elevation due to the fact that aerosols in snow cause a stronger absorption of shortwave radiation but sensible and latent heat fluxes are less impacted. The reason for this is the colder ambient temperature compared to lower elevations. This leads to an enhancement of the aerosol effect in higher elevations and furthermore, Dumont et al. emphasize that the relationship between shortening and aerosol concentration is neither linear nor logarithmic. As pointed out by Warren (2013) an assessment of aerosol concentration from satellite data is tricky. This study demonstrates how models can assist evaluating satellite data and vice versa.

Such sophisticated one-dimensional models like SNOWPACK and Crocus are truly powerful and allow a precise study of the energetic processes in a snow pack. However, they do not give us information about the spatial distribution, the influence of the terrain, and also the feedback with the atmosphere on a larger

scale. An ideal solution would be to couple such a complex snow model with an earth system model, but this is not possible due to the immensely high computational costs. Global models are therefore relying on more simplified snow models that give less information about the internal structure of the snow layer but allow a bit more insight into the interaction of other earth system components in return.

The study of Rahimi et al. (2020) is one example how such a model framework can be utilized to study the radiative impact of aerosols on snow. The base of their investigations is the WRF-Chem model in a convective-allowing grid (4 km) and additionally coupled with SNICAR. Similar to some previous studies, they focused on the radiative effect of the aerosols on the snow surface and the related feedback signals in 2m-temperature and snow water equivalent (SWE). In addition, they also studied the comparison of the aerosol effect in the atmosphere versus the aerosol effect at the surface. The investigation focused on the impact of the aerosols BC and mineral dust. In the atmosphere, mineral dust and BC had an opposite effect on the radiative forcing. Rahimi et al. argue that mineral dust is a good absorber and emitter of terrestrial radiation compared to BC because of its bigger size. Mineral dust in the atmosphere functions therefore as an isolater returning longwave radiation back to the surface, leading to a positive radiative effect at the surface. In contrast to that, BC holds its greatest influence on the radiation in the shortwave spectrum. It absorbs and scatters solar radiation in the atmosphere, leading to a negative radiative impact at the surface. However, the simulations showed that BC overrules the impact of mineral dust by far, leading to an overall negative radiative forcing in the atmosphere.

In addition, Rahimi et al. found that both, mineral dust and BC have a positive radiative impact when deposited on the snow surfaces. Dominant in this manner was BC with a positive radiative forcing of more than $2\,\mathrm{W\,m^{-2}}$. The positive radiative forcing of the aerosols in snow superimposed the negative radiative forcing of the aerosol in the atmosphere leading to an overall positive forcing. This conclusion was also supported by Usha et al., 2020. Furthermore, Rahimi et al. found a general increase in 2m-temperature by 0.15 K and an earlier snow melt out of 4 days. In this study, they found a 2 % reduction in snow albedo at high altitudes and an increased snow grain size by several microns due to the aerosols in snow. At some locations an increase in SWE could be observed despite a reduced snow albedo.

As pointed out by Rahimi et al., the primary influence in their model results was caused by BC. However, WRF-Chem showed a large underestimation of the deposition of dust in snow by a magnitude of 63 %. A sensitivity study showed that increasing the amount of dust in snow strongly enhances the significance of this aerosol type and the authors suspect that mineral dust can have similar effects compared to BC in snow when the deposition reaches a reasonable amount. Yet, as mentioned in the study, an increase of dust emissions is bound to changes in the atmosphere. Slight increases in cloud cover and general changes in meteorological variables could be observed in the sensitivity studies.

At several cases, Rahimi et al. found that 2m-temperature and SWE behaved contradictory to the expected feedback to a reduced snow albedo. They suggest that an increase in snow water equivalent or a decrease in temperature despite the positive radiative forcing of aerosols is caused by internal model variability. They stated that due to limited computational resources, it was not possible for them to further investigate internal model variability.

In this work, the model system ICOsahedral Nonhydrostatic (ICON) - Aerosol and Reactive Tracegases (ART) was extended by a parametrization of a spectral snow albedo which considers snow aging

processes and the darkening effect of mineral dust on snow. The snow albedo parametrization of pure snow was evaluated in a comparison with in-situ data. In this case study, the performance of the snow metamorphism parametrization and the most significant influences on the snow albedo were evaluated. Furthermore, the new developments were applied in a simulation covering Europe and western parts of Asia during a major mineral dust deposition event. The advantage over the majority of previous studies is that in the applied full three-dimensional model, the mineral dust was emitted, transported, and deposited online. Furthermore, the influence on the optical properties was implemented in order to operate online and to trigger feedback with the snow cover and in the atmosphere. The goal was to assess the spatial and temporal distribution of the mineral dust during this event and the resulting feedback. Thereby, the focus lied on the changes in surface albedo, the resulting radiative forcing, surface temperature, and 2m-temperature. In contrast to most studies which have addressed the effects of aerosols on seasonal or climate scales, this study aimed to determine how dust deposition affects the weather prediction at high resolution.
This study illustrates that certain regions are particularly vulnerable to the impact of mineral dust deposition. Through quantification of the feedback in the different variables, it was determined which responses are most pronounced and indications of possible causes were suggested. Furthermore, the study examines whether large-scale effects are formed during the weather forecast, due to the perturbation of the snow albedo by mineral dust. Model internal variability is a challenge in weather prediction, which is opposed in this study by the averaging of the results of an ensemble simulation. In conclusion, the following questions were addressed:

1. *Which processes have the most significant impact on the spectral albedo of pure snow which are not captured by a broadband albedo?*

2. *What is the spatial and temporal distribution of mineral dust deposition during a major Saharan dust deposition event in Eurasia and how large is the feedback resulting from the modified snow albedo?*

3. *Which kind of interference results from model internal variability and how significant are the effects?*

4. *Are there large-scale atmospheric changes due to the disturbance of the snow albedo?*

5. *Are there regions in Western Eurasia that are particularly susceptible to impacts from mineral dust on snow?*

2 Methods: The Model Framework

This section describes the basics of the applied and further developed model ICON-ART. This includes the structure of the model and the treatment of solar radiation. Furthermore, the applied multi-layer snow model is explained in detail. The ART module provides the treatment of the aerosol processes. The description of the mineral dust in ART is briefly presented here.

The ICON model is a weather and climate model developed by the German Weather Service (DWD) and the Max Planck Institute for Meteorology (MPI-M) (Zängl et al., 2015; Giorgetta et al., 2018). The model solves the full three-dimensional non-hydrostatic and compressible Navier-Stokes equations. The equations are discretized on an unstructured triangular grid that is based on a spherical icosahedron. This type of unstructured grid has several advantages over a standard rectangular grid. It has approximately the same horizontal resolution throughout all latitudes, and refining the resolution can simply be accomplished through splitting of the triangles.

The horizontal resolution is denoted by RnBk, where n is the initial amount of equal sections that the edges of the icosahedron is separated into, leading to n^2 triangles. Additional refinements are done by bisecting of the triangles where the number of bisecting steps is given by k. The total amount of horizontal cells is given by $20\ n^2\ 4^k$. Due to the flexible grid resolution, ICON is seamless and can be used at both coarse and very high resolution, as a global or regional model. It allows for multiple local grid refinements (nests) that allow for two-way interactions between the finer and the coarser grids. In such a nested setup, a larger grid refinement of a factor more than 2 is not advised. For a stronger refinement without the need of multiple nests, the Limited Area Mode (LAM) can be executed. It is the regional mode of ICON and applied in this study. The interaction is in this setting only one-way from the coarser grid to the finer but it still holds the advantage that the driving data can be obtained from a global run of the same model. Thereby the physics remain consistent. The LAM mode can be forced by ICON data but allows also other sources of meteorological data. A detailed description of the model physics can be found in Zängl et al. (2015) and Giorgetta et al. (2018).

In this study, the radiation in ICON is treated by the Rapid Radiative Transfer Model (RRTM) described by Mlawer et al. (1997). This radiative transfer model calculates the shortwave and the longwave radiation in 30 spectral bands between 0.2–1000 µm. This means, according to the atmospheric composition, such as trace gases and clouds, it computes how much and in which bands the solar radiation is reduced while passing through the atmosphere. In this manner the radiation that eventually reaches the land surface is calculated. 14 of these bands cover the shortwave radiation (up to 3.846 µm). The treated components that absorb this shortwave radiation are namely water vapor (H_2O), carbon dioxid (CO_2), methane (CH_4), nitrous oxide (N_2O), ozone (O_3), trichlorofluoromethane (CFC-11), dichlorodifluoromethane (CFC-12), and aerosols (Morcrette et al., 2008). The RRTM uses the correlated-

k method instead of a line-by-line model since its computing time is reduced in comparison. A detailed description of this method can be found in Mlawer et al. (1997).

2.1 The Snow Model in ICON

For the lower boundary of the atmosphere, ICON can be coupled with two different land surface models. One of these models is called JSBACH, which is used with climate physics. The other land surface and vegetation model is called TERRA_ML, which is used for operational numerical weather prediction, and also applied in this study. The land surface model serves as a transmitter of heat, moisture, and momentum between the atmospheric component and the land surface (Doms et al., 2018). Interactions include, for example, surface roughness length, vegetation-dependent evaporation, vertical heat, water transport in the soil, photosynthetic active radiation, surface albedo, and snow cover. The individual cells are treated thereby according to the tile approach after Avissar and Pielke (1989). For this approach, the surface in every cell is separated into proportions of different surface types to consider various attributes of the land surface.

TERRA_ML provides two different snow models. The first is used in operational weather forecast and is a single-layer snow model. As pointed out by previous studies (e.g., Jacobi et al., 2015) a single-layer snow model scheme is not capable to adequately represent the energy budget and the temperature profile in a snow pack. Usually, the snow layer tends to disappear too early in springtime in such models. Furthermore, the ability to create an aerosol stratification, which describes the vertical distribution of the aerosols in snow, is not possible when having only a single layer. As pointed out by Skiles and Painter (2019), the resurfacing of the aerosols plays a major role in the optical properties of the snow. These are the main aspects why in this study an experimental snow model is used that was developed at DWD. It is also incorporated in the TERRA_ML surface scheme and the number of snow layers is adjustable (Machulskaya and Lykosov, 2008). The application of multiple snow layers allows for vertical profiles of snow temperature, water content, and snow density.

In this experimental snow model of Machulskaya and Lykosov, the snow depth is updated for each time step, and the thickness is redefined for the individual layers. This happens, on the one hand, when new snow falls, or water freezes on the top layer. On the other hand, the change of snow density due to phase changes can vary and influence the snow depth. Furthermore, mass exchange via percolation water among the layers also takes place. Lastly, at the end of each time step, the thickness of each snow layer is adjusted in such a way that they all have the same thickness. However, it can be specified that the top snow layer does not exceed the thickness up to a certain limit. In the simulations of this study, the model operates three layers, and the top layer of snow is limited to a depth of 10 cm. We chose this threshold because snow samples are often taken from the top 10 cm. This value of the top snow layer height also affects the interactions between snow and aerosol, which is explained in section 3.4.

The snow albedo in TERRA_ML is a broadband albedo that varies between a maximum $a_{snow,max} = 0.85$ and minimum value $a_{snow,min} = 0.5$ (values differ between ICON and Community Consortium Small-scale Modelling (COSMO)). In Doms et al. (2018), the snow albedo a_{snow} is given by

$$a_{snow} = a_{snow,max} S_{age} + a_{snow,min} (1 - S_{age}), \tag{2.1}$$

where S_{age} is an aging factor dependent on snow fall rate, temperature, rain, and wind. There is no spectral information and the snow albedo is applied for visible as well as the near infrared band in the RRTM.

2.2 The Aerosol Model ART

The extension ART developed at the Karlsruhe Institute of Technology (KIT) is able to simulate aerosols, trace gases, and related feedbacks (Rieger et al., 2015; Schröter et al., 2018). This module can treat various aerosol types including sea salt, volcanic ash, mineral dust, and several gaseous tracers. A detailed description of the treatment of aerosol transport can be found in Rieger et al. (2015). In this work, we use the two-moment aerosol description. The mineral dust is represented in three log-normal modes. The model considers the barycentric mean of a tracer Ψ which is here denoted by a hat ($\widehat{\Psi}$). The specific number of a tracer $\widehat{\Psi_{0,l}}$ with mode l is thereby defined with

$$\widehat{\Psi_{0,l}} = \frac{\overline{\rho_a \frac{N_l}{\rho_a}}}{\overline{\rho_a}} = \frac{\overline{N_l}}{\overline{\rho_a}} \tag{2.2}$$

and the mass mixing ratio $\widehat{\Psi_{3,l}}$ with

$$\widehat{\Psi_{3,l}} = \frac{\overline{\rho_a \frac{M_l}{\rho_a}}}{\overline{\rho_a}} = \frac{\overline{M_l}}{\overline{\rho_a}}. \tag{2.3}$$

The number concentration is denoted by N_l, the mass concentration by M_l, and the air density by ρ_a. The variables with overline are Reynolds averaged variables (e.g., $\overline{\rho_a}$).
The specific number $\psi_{0,l}(\ln d_p)$ and the mass mixing ratio $\psi_{3,l}(\ln d_p)$ for a lognormal distribution of a mode l is defined at diameter d_p by

$$\psi_{0,l}(\ln d_p) = \frac{\widehat{\Psi_{0,l}}}{\sqrt{2\pi}\ln(\sigma_l)} \exp\left(-\frac{\left(\ln d_p - \ln \overline{d}_{0,l}\right)^2}{2\ln^2\sigma_l}\right) \tag{2.4}$$

and

$$\psi_{3,l}(\ln d_p) = \frac{\widehat{\Psi_{3,l}}}{\sqrt{2\pi}\ln(\sigma_l)} \exp\left(-\frac{\left(\ln d_p - \ln \overline{d}_{3,l}\right)^2}{2\ln^2\sigma_l}\right). \tag{2.5}$$

The median diameter of the number distribution $\overline{d}_{0,l}$ and the median diameter of the mass distribution $\overline{d}_{3,l}$ of a dust mode l are diagnostic variables that are calculated from the prognostic specific number and mass mixing ratio. The standard deviations σ_l of the three modes are kept constant and are 1.7, 1.6, and 1.5. The dust emission is calculated online and based on soil type, soil moisture content and wind speed. The parametrization is based on Vogel et al. (2006) and accounts for emission due to saltation. At

emission, the three initial median diameters of the number distribution are 0.644, 3.453, and 8.671 µm. The initial median diameters of the mass distribution are 1.5, 6.7, and 14.2 µm.

During transport, the equations for the two prognostic variables, $\widehat{\Psi_{0,l}}$ and $\widehat{\Psi_{3,l}}$, need to be solved. The transport equations are defined by

$$\begin{aligned}\frac{\partial(\overline{\rho_a}\widehat{\Psi_{0,l}})}{\partial t} &= -\nabla(\widehat{\upsilon}\overline{\rho_a}\widehat{\Psi_{0,l}}) - \nabla(\overline{\rho_a \upsilon'' \Psi''_{0,l}}) \\ &\quad - \frac{\partial}{\partial z}(\upsilon_{sed,0,l}\overline{\rho_a}\widehat{\Psi_{0,l}}) - W_{0,l} + E_{0,l}\end{aligned} \tag{2.6}$$

and

$$\begin{aligned}\frac{\partial(\overline{\rho_a}\widehat{\Psi_{3,l}})}{\partial t} &= -\nabla(\widehat{\upsilon}\overline{\rho_a}\widehat{\Psi_{3,l}}) - \nabla(\overline{\rho_a \upsilon'' \Psi''_{3,l}}) \\ &\quad - \frac{\partial}{\partial z}(\upsilon_{sed,3,l}\overline{\rho_a}\widehat{\Psi_{3,l}}) - W_{3,l} + E_{3,l},\end{aligned} \tag{2.7}$$

respectively. The barycentric mean velocity is $\widehat{\upsilon}$. The turbulent flux of specific number is denoted by $\nabla(\overline{\rho_a \upsilon'' \Psi''_{0,l}})$ and the turbulent flux of mass mixing ratio by $\nabla(\overline{\rho_a \upsilon'' \Psi''_{3,l}})$. Deviations from the barycentric mean are denoted by inverted commas ($\upsilon'' = \upsilon - \widehat{\upsilon}$, $\Psi'' = \Psi - \widehat{\Psi}$). The sedimentation velocity of the specific number and mass mixing ratio of a tracer with mode l are denoted by $\upsilon_{sed,0,l}$ and $\upsilon_{sed,3,l}$, the loss of specific number and mass mixing ratio by $W_{0,l}$ and $W_{3,l}$, and the respective emission fluxes by $E_{0,l}$ and $E_{3,l}$.

Mineral dust can leave the atmosphere via sedimentation as well as dry and wet deposition. The sedimentation is the removal process caused by gravitational forces. In this process, mainly large particles are impacted and removed from the atmosphere. The treatment of sedimentation in ICON is comprehensively described by Riemer (2002). The dry deposition processes are discussed by Rieger et al. (2015). It covers the discharge of aerosols due to the influence of turbulence at the lower boundary of the atmosphere. The wet deposition covers the washout processes of aerosols by precipitation. A detailed overview is provided by Rinke (2008). When the aerosols are removed from the atmosphere via the named processes, they reach the land surface. As it is described in section 3.3, we add these aerosols to the snow cover, if such is present. The particles are finally removed from the system as soon as the snow cover disappears.

The aerosol model provides optical properties of spherical and non-spherical mineral dust particles. Hoshyaripour et al. (2019) found an increase of the AOD of 28 % due to non-spherical representation of dust particles in the atmosphere. Future studies may include the influence of nonsphericity of the mineral dust in snow, but this study treats the mineral dust as spherical particles. The RRTM can account for dust concentrations in the atmosphere. Therefore, it needs the optical properties of dust in form of three different coefficients. These are namely the mass-specific extinction coefficient k_e, the single-scattering albedo $\widetilde{\omega}$, and the asymmetry parameter g for every mode. The mass-specific extinction coefficient is defined by

$$k_e = \frac{N \sigma_{ext}}{M}, \tag{2.8}$$

where σ_{ext} is the extinction cross section. The single-scattering albedo is defined as the ratio of scattering to extinction and can be calculated via the scatter cross section σ_{sca} with

$$\widetilde{\omega} = \frac{\sigma_{sca}}{\sigma_{ext}}. \tag{2.9}$$

These optical properties of the aerosols are stored in look-up-tables (LUTs) with values for each spectral band. The treatment of the optical properties in this study is described in section 3.2.1.

3 Methods: New Model Developments

The basic paramametrizations in ICON-ART are explained in section 2. They constitute the foundation of our further developments introduced and tested in this study. In this section, the processes which we newly implemented in ICON-ART to describe the influence of mineral dust on snow albedo are explained step by step. As pointed out in section 1, it is well known that the snow albedo is strongly dependent on the age of snow. Furthermore, it is strongly variable in the solar spectrum. Therefore, a parametrization of the snow metamorphism is described in the first part (section 3.1). Then the parametrization of the spectral albedo of clean snow is explained (section 3.2), which is based on the aging parametrization. The second half of this section describes the treatment of mineral dust in snow (section 3.3) and presents how the optical properties of snow and mineral dust interact (section 3.4).

3.1 Snow Metamorphism

The optical properties of snow are determined by the microphysical structure of the individual ice crystals. The post depositional processes that the individual crystals undergo are strongly dependent on the environment and are difficult to predict. For example, at low temperature, the snow grains grow slowly, forming rounded crystals. In contrast to the aging of the cold and dry snow, wet snow at higher temperature forms clusters of ice crystals (Colbeck, 1987). The post depositional aging includes processes like settling of the snow layer, melting, sublimation and refreezing. All processes together can be described as aging of the snow, which is also known as the snow metamorphism.
The scattering of shortwave radiation occurs at the surface of the ice crystals that separates the ice matrix from the ambient air. The geometrical shape of individual crystals is quite complex. For example, ice crystals often grow into small and fine tubes or form abstract facets. Rather than describing each shape of the crystals, a possibility is to compare the scatter properties with a theoretical spherical snow grain. This theoretical snow grain has the same surface to volume ratio as the complex shape of the true ice crystal. This snow grain is referred to as an optical equivalent snow grain. Here, it is important to emphasize that not only the outer surface is relevant for the scattering of radiation but also the surface that is facing the inner side of the crystal. This optical equivalent snow grain can be described by using two different physical values which can be transformed from one to another. The first value is the specific surface area *SSA* that is either described as the ratio of the surface area A_{ice} to the mass M_{ice} of an ice crystal (e.g. Hoff et al., 1998; Domine et al., 2001) or the ratio of the surface area A_{ice} to the volume V_{ice} of an ice crystal (e.g., Schneebeli and Sokratov, 2004). Therefore, SSA_M and SSA_V are defined by

$$SSA_M = \frac{A_{ice}}{M_{ice}} = \frac{4\,\pi\,{r_{snow}}^2}{\frac{4}{3}\,{r_{snow}}^3\,\rho_{ice}} \tag{3.1}$$

and

$$SSA_V = \frac{A_{ice}}{V_{ice}} = \frac{4\,\pi\,{r_{snow}}^2}{\frac{4}{3}\,{r_{snow}}^3}. \tag{3.2}$$

The density of ice is $\rho_{ice} = 917\,\mathrm{kg\,m^{-3}}$. Another way to express the scatter properties of snow is to specify the radius of the optical equivalent snow grain r_{snow}. The grain radius can be calculated from the *SSA* with

$$r_{snow} = \frac{4\,\pi\,{r_{snow}}^2}{\frac{4}{3}\,{r_{snow}}^3\,\rho_{ice}} = \frac{3}{\rho_{ice}\,SSA_M} \tag{3.3}$$

and

$$r_{snow} = \frac{3}{SSA_V}, \tag{3.4}$$

respectively. The optical equivalent snow grain radius is highly dependent on the meteorological conditions and the age of the snow. Fresh snow is characterized by very small snow grains, mostly ranging between 50 and 100 µm. During snow metamorphism the snow grains grow larger and the scatter properties change. Main drivers of the snow metamorphism can be divided in equi-temperature metamorphism processes and temperature-gradient metamorphism processes (Sommerfeld and LaChapelle, 1970). Under isothermal conditions water vapor moves from small crystals to larger snow grains. This leads to a rounding of the complex facets of the snow crystals in order to minimize the surface free energy. The temperature is key point in the speed of this process. Low temperatures slow down the process while a snow temperature close to the melting point causes a rapid metamorphism.
The main process that governs the temperature-gradient metamorphism is the transport of water vapor from warmer temperatures to colder and therefore the transport from the bottom to the top snow layer. There can be alternating melting and freezing cycles during these metamorphism processes that even further affect the shape of the snow grains (Sommerfeld and LaChapelle, 1970; Colbeck, 1987).
In this study, we introduced a new prognostic variable r_{snow} into the multi-layer snow model to characterize the state of snow metamorphism. The parametrization of the aging processes follow the equation of the Met Office Surface Exchange Scheme (MOSES) 2.2 (Essery et al., 2001) and is defined by

$$r_{snow} = \left[{r_{snow,t-1}}^2 + \frac{G_r}{\pi}\,\Delta t\right]^{\frac{1}{2}} - \left[r_{snow,t-1} - r_0\right]\frac{S_f\,\Delta t}{d_0}. \tag{3.5}$$

The optical equivalent snow grain radius r_{snow} is calculated from the optical equivalent snow grain radius of the last time step $r_{snow,t-1}$, the initial grain radius during snowfall ($r_0 = 50\,\mu\mathrm{m}$), and the snow fall rate S_f. The snow grain size is set to the initial value when the amount of snowfall reaches $d_0 = 2.5\,\mathrm{kg\,m^{-2}}$. The empirical snow aging growth rate G_r for the optical snow grain radius is dependent on snow temperature T_{snow} and differentiates between two temperature ranges. The equation relationships

$$G_r = \begin{cases} 0.6\,\mu m^2\,s^{-1} & T_{snow} \geq 273.15\,K \\ & \text{(melting snow)} \\ 0.06\,\mu m^2\,s^{-1} & T_{snow} < 273.15\,K,\ r_{snow} < 150\,\mu m \\ & \text{(cold fresh snow)} \\ A\,\exp(-E/R\,T_{snow}) & T_{snow} < 273.15\,K,\ r_{snow} > 150\,\mu m \\ & \text{(cold aged snow)} \end{cases} \tag{3.6}$$

where G_r in $\mu m^2\,s^{-1}$, A in $\mu m^2\,s^{-1}$, E in $J\,mol^{-1}$, R in $J\,K^{-1}\,mol^{-1}$, T_{snow} in K, r_{snow} in µm

apply to melting snow and cold snow. The growth rate in cold snow also depends on the grain size itself. For cold aged snow, G_r is parametrized based on T_{snow}, the constants $A = 0.23\,10^6\,\mu m^2\,s^{-1}$ and $E = 3700\,J\,mol^{-1}$, and the universal gas constant $R = 8.314472\,J\,K^{-1}\,mol^{-1}$. The range of optical equivalent grain radius in Essery et al. (2001) is between 50 and 2000 µm.

The presented metamorphism parametrization does not include the impact of rain fall. Due to the fact that wet snow ages more quickly (e.g., Brun, 1989), we add an acceleration due to rain. The extended parametrization is described by

$$\begin{aligned} r_{snow} = &\left[{r_{snow,t-1}}^2 + \frac{G_r}{\pi}\,\Delta t \right]^{\frac{1}{2}} - \left[r_{snow,t-1} - r_0 \right] \frac{S_f\,\Delta t}{d_0} \\ &+ \left[r_{max} - r_{snow,t-1} \right] \frac{z_{rain}\,\Delta t}{z_{rain,max}}. \end{aligned} \tag{3.7}$$

Here, z_{rain} stands for the rain fall rate, $z_{rain,max}$ for the amount of rain fall which is needed to maximize the acceleration of metamorphism due to rain fall. Unfortunately, there are no measurements on the growth of the equivalent snow grain size during rain known to us. It is recommended to adjust this value if there are any measurements on the behavior of the grains depending on the rainfall in the future. The applied value currently corresponds to the amount of rain that was used in ICON-ART already prior to this study in order to completely age the snow albedo. In section 4, a case study is conducted showing that the parametrization suffers from weaknesses in the arctic regime. As described in more detail in that section, we extended the range of the growth factor in order to cover a broader temperature range. We expanded the range of values for the optical equivalent snow grain radius to cover a span of 40 to 2500 µm. By considering the study of Kaempfer and Schneebeli (2007), we extended growth rate G_r by the conditions

$$G_r = \begin{cases} 0.6 & T_{snow} \geq 273.15\,\mathrm{K} \\ 0.06 & 271.55\,\mathrm{K} < T_{snow} < 273.15\,\mathrm{K},\ r_{snow} < 150\,\mu\mathrm{m} \\ A\,\exp(-E/R\,T_{snow}) & 271.55\,\mathrm{K} < T_{snow} < 273.15\,\mathrm{K},\ r_{snow} > 150\,\mu\mathrm{m} \\ \dfrac{1}{0.644\,r_{snow}} + 0.01 & 264.85\,\mathrm{K} < T_{snow} \leq 271.55\,\mathrm{K} \\ 11.78\,{r_{snow}}^{-1.54} + 0.01 & 254.05\,\mathrm{K} < T_{snow} \leq 264.85\,\mathrm{K} \\ 0.009\,{r_{snow}}^{-0.2} + 0.008 & 219.15\,\mathrm{K} < T_{snow} \leq 254.05\,\mathrm{K} \\ 0 & T_{snow} \leq 219.15\,\mathrm{K} \end{cases} \tag{3.8}$$

where G_r in $\mu\mathrm{m}^2\,\mathrm{s}^{-1}$, A in $\mu\mathrm{m}^2\,\mathrm{s}^{-1}$, E in $\mathrm{J\,mol}^{-1}$, R in $\mathrm{J\,K}^{-1}\,\mathrm{mol}^{-1}$, T_{snow} in K, r_{snow} in µm.

The initialization of the snow grain size turns out to be a difficult task. There are no global data on the optical snow grain size. As shown in studies like Aoki et al. (2003), the measurements of optical snow grain size using remote sensing techniques suffer from a lot of uncertainties and depend on many assumptions. Rather than relying on selective measurements, we use a relationship between snow density ρ_{snow} and snow grain size. Several studies report a relationship between snow density and grain size but emphasize that this relationship is complex and case dependent. Nevertheless, there are empirical parametrizations available in Legagneux et al. (2002) and Domine et al. (2007) or Narita (1971) and adapted by Yasunari et al. (2011). The parametrization of Domine et al. (2007) is defined by

$$r_{snow} = \frac{3}{\rho_{ice}\,(-308.2\,\ln(\rho_{snow}) - 206.0)}, \tag{3.9}$$

where r_{snow} in µm, ρ_{ice} in $\mathrm{kg\,m}^{-3}$, ρ_{snow} in $\mathrm{kg\,m}^{-3}$.

We incorporated Eq. 3.9 in ICON-ART to enable a spatially variable approximation of the initial optical equivalent snow grain size. This parametrization is exclusively used for the initialization at the beginning of the simulation.

3.2 The Spectral Snow Albedo

Although snow appears white to our eyes, it is not reflective at all wavelengths. The strongest reflection takes place in the visible range, which explains the white color. What we cannot see with our eyes is that snow becomes more absorbent in the near infrared. Therefore, it is important to look at the optical properties of snow in the entire wavelength range of shortwave radiation. Furthermore, the impact of external influences is also wavelength-dependent, so that the calculations of the optical properties must

be performed individually for different ranges. Since it is assumed that the snow grains are spherical, we can use the Mie theory according to Mie (1908). This is an approximation since we know that especially freshly deposited ice crystals are in fact not spherical. Dang et al. (2016) compared nonspherical to spherical snow grains in an radiative transfer model and found that the albedo of nonspherical grains is slightly higher. They found an increase of 3.2 % compared to a snow pack of spherical snow grains with an optical equivalent grain radius of 100 µm. An increase of 5.0 % can be seen when considering an optical equivalent grain radius of 1000 µm. However, they state that the albedo of nonspherical snow grains can be mimicked by simply using smaller grains with spherical shape.

3.2.1 Mie Calculations

The optical equivalent snow grain size described in section 3.1 is the requirement for the calculations of the optical properties of snow based on the Mie-Theory (Mie, 1908). The input for the Mie scattering computations is the dimensionless size parameter x for wavelength λ which is defined by

$$x = 2\,\pi\, r_{snow}/\lambda\,. \tag{3.10}$$

Furthermore, the computations require the imaginary and the real refractive indices of ice. Fig. 3.1 shows the interpolated values from Warren and Brandt (2008), which are revised values from the collection of Warren (1984). We used the revised indices in this study for the Mie calculations of optical properties of various snow grains. The results of these Mie calculations are the dimensionless and wavelength dependent parameters Mie extinction efficiency Q_{ext}, Mie scatter efficiency Q_{sca}, asymmetry parameter g, and Mie backscatter efficiency Q_{back}. The latter is not needed in this study. Subsequently, we obtained the extinction cross section σ_{ext} and scatter cross section σ_{sca} with

$$\sigma_{ext} = \pi\, {r_{snow}}^2\, Q_{ext} \tag{3.11}$$

and

$$\sigma_{sca} = \pi\, {r_{snow}}^2\, Q_{sca}. \tag{3.12}$$

We computed the single-scattering albedo $\widetilde{\omega}$ by applying Eq. 2.9. These coefficients are needed for the snow albedo calculation, described in section 3.2.2 in detail.

We performed Mie calculations for grain sizes ranging from 20–2450 µm for a wavelength range of 0.2–5.0 µm in 10 nm wavelength intervals. The grain radius intervals increase with grain size since the smaller grains differ in the optical properties stronger than larger grains. The calculations were carried out in steps of 10 µm between 20 µm and 100 µm, 20 µm between 100 µm and 200 µm, 25 µm between 200 µm and 300 µm, 50 µm between 300 µm and 550 µm and in steps of 100 µm between 550 µm and 2450 µm.

When performing the Mie calculations for one grain size only, a quasi oscillatory "ripple" effect (Wiscombe and Warren, 1980) can be observed in all Mie parameters (Q_{ext}, Q_{sca}, g, and Q_{back}). These

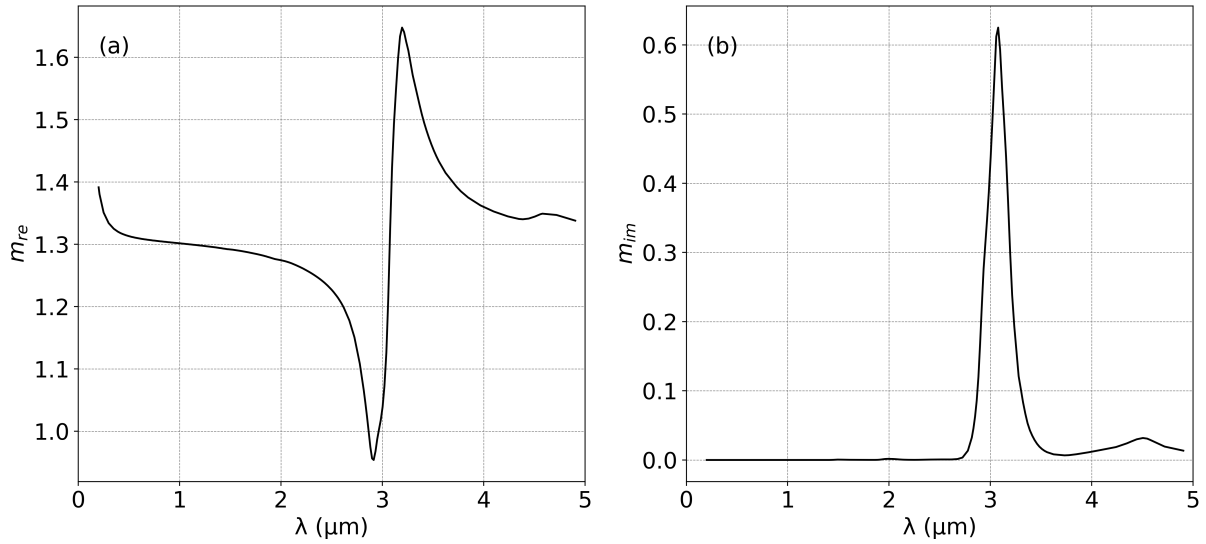

Figure 3.1: Real refractive index of ice m_{re} (a) and imaginary refractive index of ice m_{im} (b) proposed in Warren and Brandt (2008).

fluctuations are unrealistic due to the fact that a snow sample never contains only one snow grain size. To minimize the ripple effect, we performed 21 calculations in 1 % steps (10 % above and 10 % below the respective grain size) and averaged the results. For example, for a grain size of 100 µm, Mie calculations between 90 µm and 110 µm were performed with a 1 µm interval and then averaged. Fig. 3.2a shows the ripples of the Mie extinction efficiency when only one grain size of $r_{snow} = 100\,\mu m$ is taken into account. In contrast, Fig. 3.2b shows the result for $r_{snow} = 100\,\mu m$ when averaged over a range of 90 µm and 110 µm. At a wavelength of $\lambda = 3.0\,\mu m$ a sharp dip occurs where the real refractive index of ice approaches 1. However, this range is not included in our calculations, as explained below.

Our calculated optical properties of snow have a very high spectral resolution of 10 nm which is very detailed in comparison to the spectral bands in ICON-ART (section 2). By averaging over the RRTM bands, most of this spectral information would get lost. As pointed out by many studies (e.g., Wiscombe and Warren, 1980, Skiles and Painter, 2018), the impact of aerosols is crucial at shorter wavelengths where the solar irradiance varies strongly over the spectral range. For this reason, we assembled a new set of spectral bands, focusing only on the shortwave spectrum at a higher resolution. These bands are later integrated to the corresponding radiation bands of ICON-ART, as described in section 3.2.3.

The compilation of wavelength bands contain 18 bands ranging from 0.30–1.65 µm. The reason for this range is that at longer wavelengths the solar energy is comparatively low and plays only a minor role. Furthermore, measurement instruments for the shortwave spectrum, such as those used on satellites, are usually not sensitive up to 5 µm. This reduction saves computing time and makes the results more comparable. We use the bands that originate from the atmospheric radiative transfer model Streamer (Key and Schweiger, 1998). Tab. 3.1 gives an overview of the Streamer bands and their spectral range. We used Steamer to calculate weighting factors for a cloud free location in mid-latitude winter, which describe the fractions of solar irradiance among the individual bands. In other words, the weighting factors are the respective shortwave energy fluxes divided by the sum of the energy flux of all 18 bands. These weighting factors are also listed in Tab. 3.1, as well as the number of the associated band in the

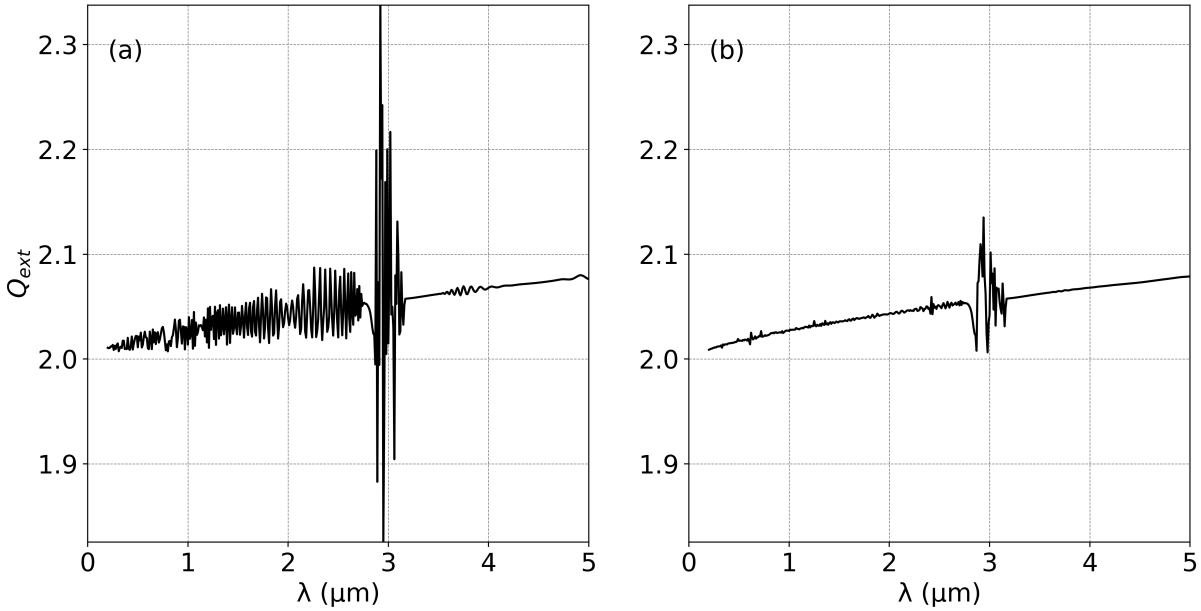

Figure 3.2: Mie extinction efficiency Q_{ext} for an optical equivalent snow grain radius of 100 µm at a wavelength range λ between 0.2 µm and 5.0 µm, considering only one precise grain size (a) and considering the average of a range of $\pm 10\,\%$ (b).

RRTM. The spectrally highly resolved results of the Mie calculation were averaged over the streamer bands (e.g., band 1: 0.30–0.33 µm) and put together in LUTs. The LUTs contain the Mie extinction efficiency, the Mie scatter efficiency and the asymmetry parameter for each of the 18 bands for the snow grain sizes 20–2500 µm as described above. These values are all required for the calculation of the spectral snow albedo, as described in the following section.

Table 3.1: Streamer bands, corresponding lower wavelength boundary λ_{min} and upper wavelength boundary λ_{max}, weighting factors calculated with Streamer for a cloud free location in mid-latitude winter, and number of the associated RRTM bands in ICON-ART.

Streamer Band No.	λ_{min} (μm)	λ_{max} (μm)	**weight**	**RRTM Band No.**
1	0.30	0.33	0.0078	28
2	0.33	0.36	0.0273	27
3	0.36	0.40	0.0325	27
4	0.40	0.44	0.0535	27
5	0.44	0.48	0.0661	26
6	0.48	0.52	0.0639	26
7	0.52	0.57	0.0832	26
8	0.57	0.64	0.1083	26
9	0.64	0.69	0.0706	25
10	0.69	0.75	0.0780	25
11	0.75	0.78	0.0270	25
12	0.78	0.87	0.0879	24
13	0.87	1.01	0.0902	24
14	1.01	1.10	0.0647	24
15	1.10	1.19	0.0340	24
16	1.19	1.28	0.0410	23
17	1.28	1.53	0.0355	22
18	1.53	1.65	0.0279	22

3.2.2 Snow Albedo Computation

The first who introduced a model for the calculation of the spectral snow albedo, were Warren Wiscombe and Stephen Warren. They proposed a model for clean snow and snow containing impurities (Wiscombe and Warren, 1980; Warren and Wiscombe, 1980). Their computations are still valid and used in many models (e.g., SNICAR). For this study, we implemented the model for the diffuse albedo a_d as well as the direct albedo a_s from Wiscombe and Warren (1980). In ICON-ART, diffuse and direct albedo are computed in two different steps. First, the diffuse albedo is calculated for the visible spectrum and the near infrared. In a next step, the direct albedo (VIS and NIR) is calculated from the diffuse albedo under consideration of the solar zenith angle μ_0.We replace the VIS and NIR snow albedo in both of these steps with the parametrizations described in the following of this section. The merge of direct and diffuse albedo in the visible and the near infrared range happens in the RRTM.

The solar radiation can deeply penetrate a layer of snow, especially the direct radiation. Hence, it is important to differentiate between a semi-infinite snow layer and an optically thin snow layer. The first scatters or absorbs the solar radiation completely without transmittance. The latter partly transmits the

radiation down to the ground where additional absorption and scattering can occur. In this case, the ground beneath the snow changes the joint surface albedo. According to Wiscombe and Warren (1980), the spectral snow albedo for a semi-infinite snow layer a^{∞} for diffuse radiation is defined by

$$a_d^{\infty} = \frac{2\,\widetilde{\omega}^*}{1+P}\left\{\frac{1+b^*}{\xi^2}\left[\xi - \ln\left(1+\xi\right)\right] - b^*/2\right\} \tag{3.13}$$

and the spectral snow albedo for a semi-infinite snow layer for direct radiation by

$$a_s^{\infty}(\mu_0) = \frac{\widetilde{\omega}^*}{1+P}\frac{1-b^*\,\xi\,\mu_0}{(1+\xi\,\mu_0)}. \tag{3.14}$$

In this computation, the single-scattering albedo $\widetilde{\omega}$ and the asymmetry parameter g are transformed into $\widetilde{\omega}^*$ and g^* with

$$\widetilde{\omega}^* = \frac{(1-g^2)\,\widetilde{\omega}}{1-g^2\,\widetilde{\omega}} \tag{3.15}$$

and

$$g^* = \frac{g}{1+g}. \tag{3.16}$$

In addition, the abbreviations P, ξ, a^*, and b^* are used, which are defined with

$$P = \frac{2\,\xi}{3\,a^*}, \tag{3.17}$$

$$\xi = \left[3\,a^*(1-\widetilde{\omega}^*)\right]^{1/2}, \tag{3.18}$$

$$a^* = 1 - \widetilde{\omega}^*\,g^*, \tag{3.19}$$

$$b^* = \frac{g^*}{a^*}. \tag{3.20}$$

For a thin snow layer with an equivalent depth of liquid water in snowpack L and a ground albedo of a_{gr} below the snow, the diffuse snow albedo a_d is defined by

$$a_d = \frac{Q a_d}{(1+P)\,Q^+ - (1-P)\,Q^-)} \tag{3.21}$$

and the direct snow albedo a_s, considering the solar zenith angle μ_0, by

$$a_s(\mu_0) = \frac{Qa_s(\mu_0)}{(1+P)\,Q^+ - (1-P)\,Q^-)}. \tag{3.22}$$

The terms Qa_d and Qa_s are given by

$$\begin{aligned} Qa_d = {} & 2P\left[(1-\gamma+\widetilde{\omega}^*\,b^*)(1-{\tau_0}^*) - \frac{\gamma\,\widetilde{\omega}^*(1+b^*)}{1-\widetilde{\omega}^*}\right]\exp(-{\tau_0}^*) \\ & - 2P\left[\widetilde{\omega}^*(1+b^*)\left(\frac{2}{\xi^2}+\frac{\gamma\,{\tau_0}^*}{1-\widetilde{\omega}^*}\right) + (1-\gamma+\widetilde{\omega}^*\,b^*)\,{\tau_0}^{*2}\right] \\ & \cdot\ \mathrm{Ei}(-{\tau_0}^*) + \frac{2\,\widetilde{\omega}^*\,(1+b^*)}{\xi^2}\left[Q^+\{\mathrm{Ei}\,[-(1+\xi)\,{\tau_0}^*] \right. \\ & + \xi - \ln(1+\xi)\} - Q^-\{\mathrm{Ei}\,[-(1-\xi)\,{\tau_0}^*] - \xi \\ & \left. - \ln|1-\xi|\}\right] - \widetilde{\omega}^*\,b^*\,(Q^+ - Q^-) \end{aligned} \tag{3.23}$$

and

$$\begin{aligned} Qa_s(\mu_0) = {} & 2\left[P\,(1-\gamma+\widetilde{\omega}^*\,b^*) + \widetilde{\omega}^*\,(1+b^*)\frac{\gamma\xi\,\mu_0 - P}{1-\xi^2\,{\mu_0}^2}\right] \\ & \cdot\exp\,(-{\tau_0}^*/\mu_0) - \widetilde{\omega}^*\,b^*\,(Q^+ - Q^-) + \widetilde{\omega}^*\,(1+b^*) \\ & \cdot\left(\frac{Q^+}{1+\xi\,\mu_0} - \frac{Q^-}{1-\xi\,\mu_0}\right). \end{aligned} \tag{3.24}$$

The optical depth τ_0 is defined by

$$\tau_0 = \frac{3\,L\,Q_{ext}}{4\,r_{snow}\,\rho_{ice}} \tag{3.25}$$

and the corresponding transformation into ${\tau_0}^*$ is computed with

$${\tau_0}^* = (1-\widetilde{\omega}\,g^2)\,\tau_0. \tag{3.26}$$

In addition, the abbrevations Q^+, Q^-, and γ are used which represent

$$Q^+ = (\gamma+P)\,\exp(\xi\,{\tau_0}^*), \tag{3.27}$$

$$Q^- = (\gamma-P)\,\exp(-\xi\,{\tau_0}^*), \tag{3.28}$$

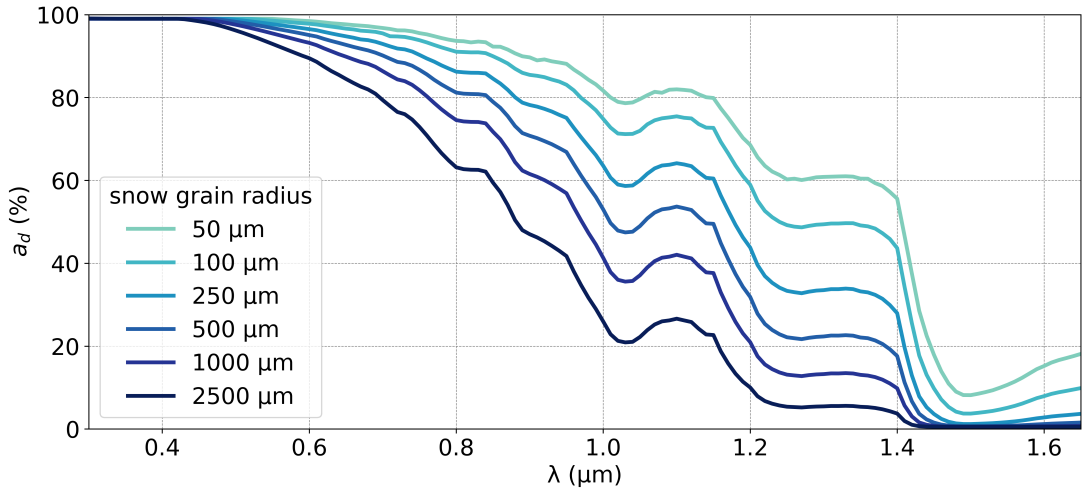

Figure 3.3: Diffuse albedo a_d of a semi-infinite snow layer with various optical equivalent snow grain radii at wavelengths λ between 0.30 µm and 1.65 µm.

$$\gamma = \frac{1 - a_{gr}}{1 + a_{gr}}. \tag{3.29}$$

The exponential integral Ei is defined by

$$\mathrm{Ei}(x) = \begin{cases} -\int_{-x}^{\infty} e^{-t}\, t^{-1}\, dt, & x < 0 \\ -\lim\limits_{\varepsilon \to 0^+} \left[\int_{-x}^{-\varepsilon} + \int_{\varepsilon}^{\infty} \right] e^{-t}\, t^{-1}\, dt, & x > 0. \end{cases} \tag{3.30}$$

Fig. 3.3 shows the spectral snow albedo for diffuse radiation between 0.30 µm and 1.65 µm for different snow grain sizes of a semi-infinite snow layer using Eq. 3.13. The spectral albedo for direct radiation is similar to the curve for diffuse radiation. An increase in the zenith angle leads to an increase in the snow albedo. The diffuse albedo is equivalent to the direct albedo at a solar zenith angle of 50°, as shown in Fig. 3.4.

Fig. 3.5 shows the impact of the ground albedo below the snow on the spectral diffuse snow albedo by application of Eq. 3.21. Here, the snow is assumed to have an optical equivalent snow grain radius of 100 µm, a snow density of 100 kg m^{-3}, and various snow depths. We determined that the decision whether to use Eq. 3.13 or Eq. 3.21 for the calculation of diffuse snow albedo is made by considering the optical depth. As long as $\tau_0 < 50$ it is assumed that the snow albedo could be influenced by the albedo beneath the snow and Eq. 3.21 is chosen for the computation. The Beer–Lambert law describes the attenuation of light when traveling through a material with

$$I(\lambda) = I_0(\lambda)\, e^{-\tau_0}, \tag{3.31}$$

where I_0 is the irradiance at entry and I is the irradiance at exit from the medium at wavelength λ. Following this definition, an optical thickness of 50 leads to a transmission of irradiance less than e^{-50} times the irradiance at entry. As shown in Fig. 3.5, the results of Eq. 3.21 and Eq. 3.13 converge for

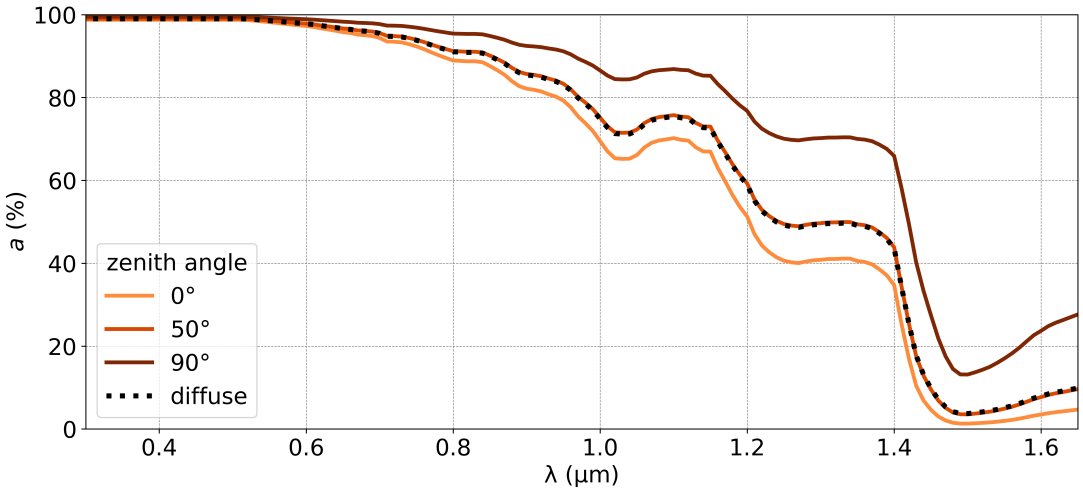

Figure 3.4: Spectral snow albedo a of a semi-infinite snow layer with a snow grain size of 100 µm, for direct radiation at different zenith angles (orange-brown) and for diffuse radiation (black, dotted) at wavelengths λ between 0.30 µm and 1.65 µm.

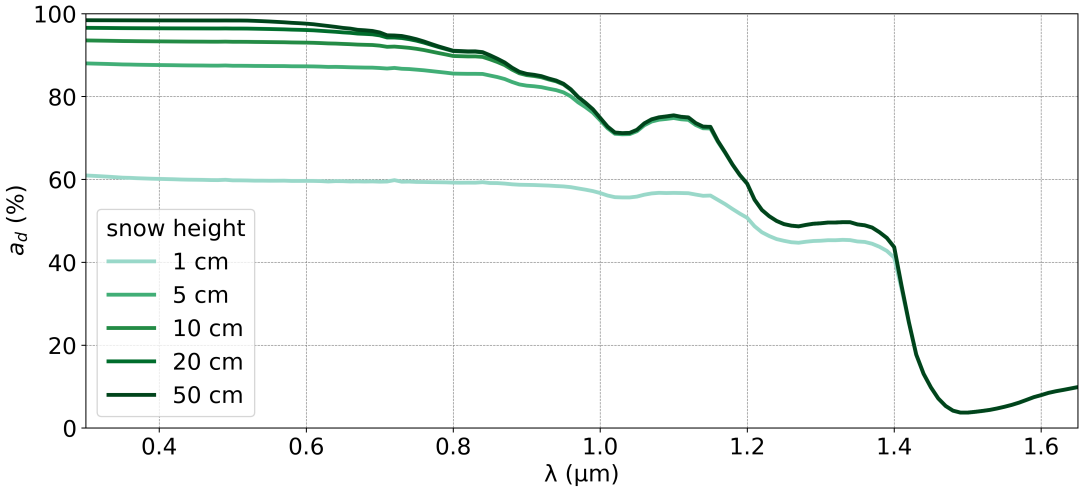

Figure 3.5: Diffuse snow albedo a_d of optically thin snow layers with various snow heights, snow density of 100 kg m^{-3} (fresh snow), optical equivalent radius of 100 µm, and ground albedo below the snow of 10 % at wavelengths λ between 0.30 µm and 1.65 µm.

deep snow layers (large optical thickness). We chose the comparatively high threshold of $\tau_0 = 50$ for precautionary reasons, but the threshold can be adjusted in the future to save computing time.

3.2.3 Merging and Weighting of Spectral Bands

As pointed out in section 3.2.1 the new implemented optical properties of snow are merged into 18 bands to save computation time (Tab. 3.1). For this reason the result of the online albedo caculation consists of 18 values associated with these bands. Fig. 3.6 shows an example of the spectral albedo for a semi-infinite snow cover with an optical grain radius of 100 µm at high spectral resolution and the respective averaged values for the 18 bands.

The RRTM in ICON-ART requires the surface albedo in two relatively broad bands. One of them is the albedo for the visible range and the other one is the albedo for the near infrared range. For the transfer of the 18 values to the two broad band values, the albedo must be spectrally integrated. For this purpose, we use the weighting factors of Tab. 3.1. As mentioned in section 3.2.1, these weighting factors were calculated with the raditative transfer model Streamer and describe the ratio of the energy fluxes among the bands for a certain time and location. In this case, a clear sky in mid-latitude winter was chosen. However, the ratio of the spectral solar energy changes depending on the atmospheric conditions. With a fixed weighting, uncertainties would be introduced to the integration. Therefore, we first merge the albedo values of the 18 bands to the matching RRTM bands as specified in Tab. 3.1 (e.g., Streamer bands 2 to 4 for RRTM band 27). Fig. 3.7 shows the transformed albedo values of Fig. 3.6 in the RRTM bands (optical grain radius of 100 µm, semi-infinite snow layer).

In the last step, the RRTM bands are combined to form the bands of the VIS and the NIR range. Here, the actual online calculated energy fluxes of the RRTM are included in the integration. Thereby, the weighing of the RRTM bands changes depending on the atmospheric conditions. Fig. 3.8 shows an example of the merged albedo values of Fig. 3.7 for the visible range and the near infrared range (optical grain radius of 100 µm, semi-infinite snow layer).

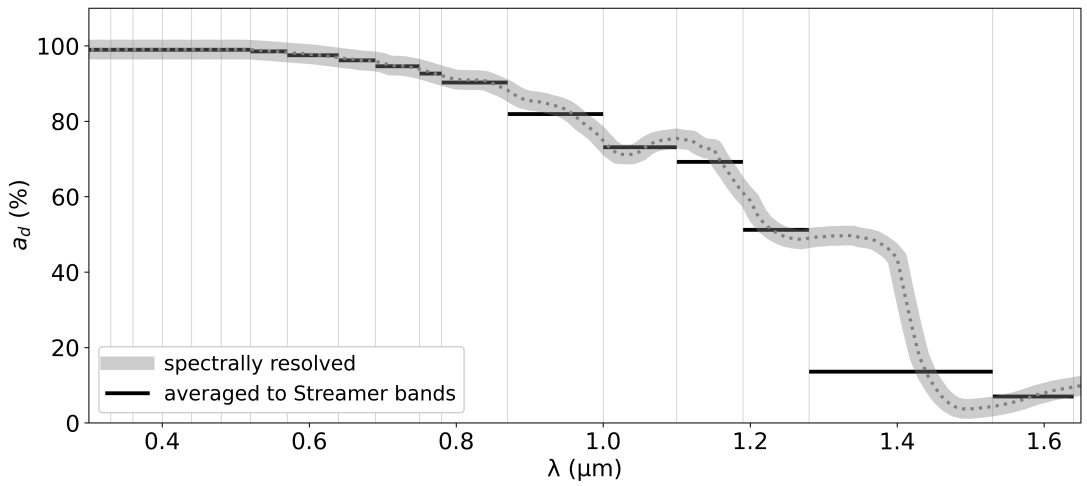

Figure 3.6: Diffuse snow albedo a_d of a semi-infinite snow layer with an optical equivalent snow grain radius of 100 µm at high spectral resolution following Wiscombe and Warren (1980) (gray) and averaged to match the 18 Streamer bands (black) at wavelengths λ between 0.30 µm and 1.65 µm.

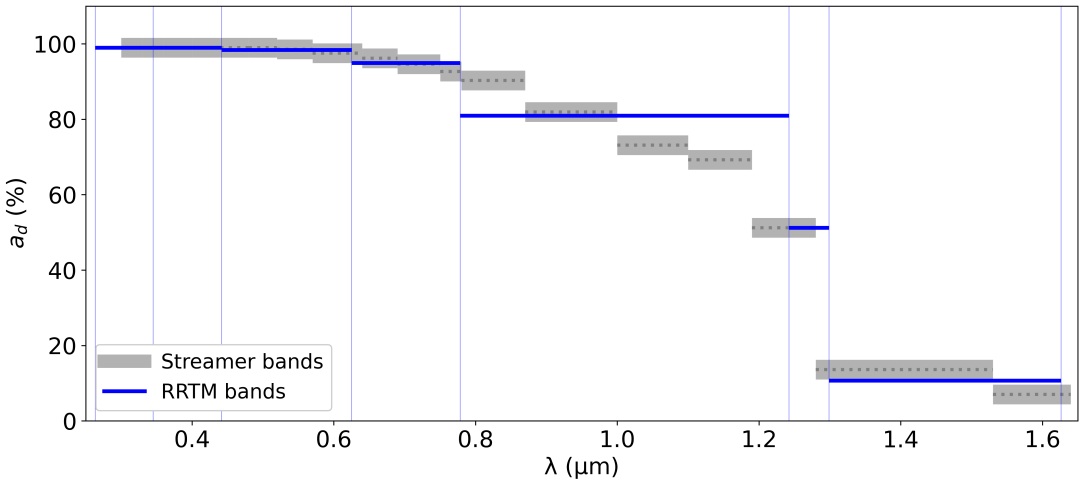

Figure 3.7: Diffuse snow albedo a_d of a semi-infinite snow layer with an optical equivalent snow grain radius of 100 µm spectrally integrated to match the 18 Streamer bands (gray) and spectrally integrated to the RRTM bands (blue) at wavelengths λ between 0.30 µm and 1.65 µm.

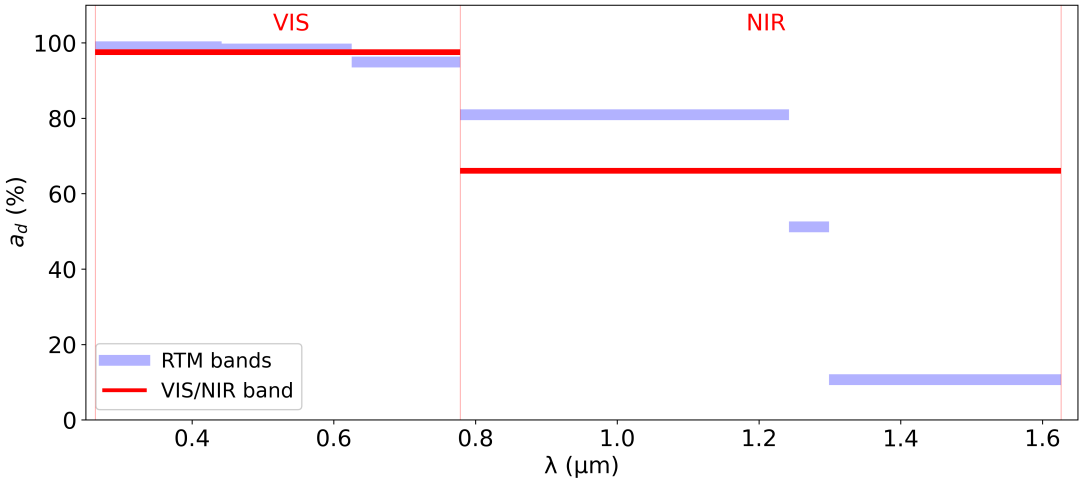

Figure 3.8: Diffuse snow albedo a_d of a semi-infinite snow layer with an optical equivalent snow grain radius of 100 µm spectrally integrated to match the RRTM bands (blue) and the broad band ranges of visible wavelengths VIS and infrared range NIR (red) at wavelengths λ between 0.30 µm and 1.65 µm.

3.3 Mineral Dust Concentration in Snow

In section 2.1, the snow model was briefly described and it was outlined that the snow properties are calculated anew for every time step. The thickness of the snow layers is therefore also adjusted in every time step. The layers are forced to have the same thickness between each other, except for the top layer, which can be limited to a maximum thickness set by the user. Hence, aerosol deposition cannot be tracked by assigning them to a specific layer. The numbering of layers is kept constant over the simulation and the aerosols would always remain in the top layer.

Consequently, we introduce mineral dust tracking by a locking of the dust mass to a certain height in snow above the ground. Thereby, the mass is distributed evenly within a layer since the exact information about the location cannot be stored. A shifting of aerosols is only introduced to the system when the total snow height changes. Snowfall, compression and other physical processes are neglected in this approach. We assume that both snow melt and accumulation of snow occur at the upper boundary toward the atmosphere. These are considerable simplifications, but sufficient for a first estimation of top layer aerosol concentration in this study.

Fig. 3.9 illustrates an example of a snow cover with 3 layers, with the same thickness. It shows how the aerosols accumulate in the snow layers and how they are transferred to other layers as the total snow depth changes. We calculate the amount of new deposition using the accumulated deposition since simulation start. The accumulation at the current time step that has built up on the surface results from the difference to the accumulation of the last time step. This new deposition is always allocated to the uppermost snow layer. The aerosols do not stay on top of the snow layer but directly transfer into it. This means that the optical properties of those aerosols are always diluted by the optical properties of the snow mass in the first snow layer (kept at 10 cm in this study). However, this behavior is not unrealistic in many cases, as the sinking of aerosols into the snow within the first minutes is observed on several occasions (Peltoniemi et al., 2015; Svensson et al., 2016). The total mass and number of the dust tracer is stored for each snow layer. We assume that snow melts always from the top. In this way the aerosols can resurface an concentrate at the top. If the snow cover disappears completely in a cell, the aerosols leave the system. This happens exclusively when the snow cover disappears.

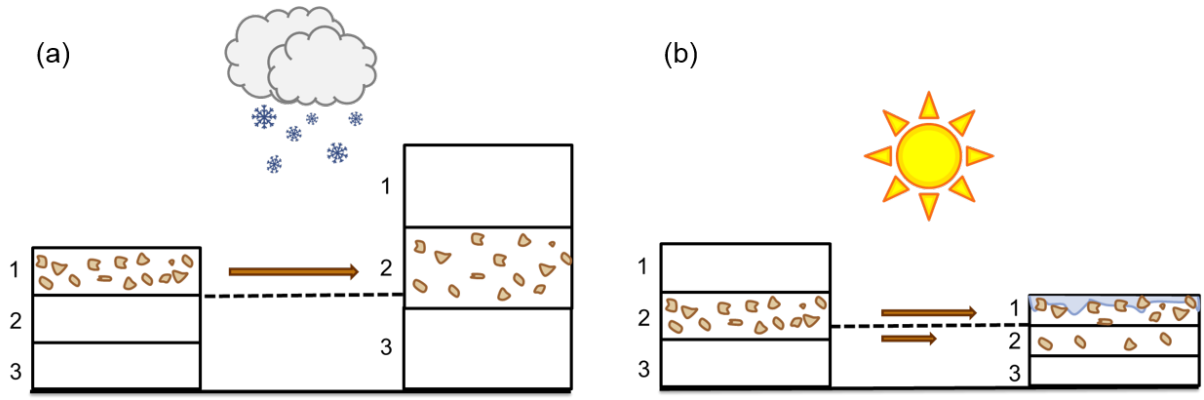

Figure 3.9: Shifting of aerosols between layers when snow accumulates and aerosols sink into deeper layers due to snow fall (a) and melting occurs where aerosols move into higher snow layers and resurface (b).

During the transfer of aerosols from one layer to another, we calculate a concentration for each layer considering the snow layer thickness and the stored dust tracer information of the last time step. This concentration is then fixed to the height above the ground and assigned to the corresponding new layer which is located at the same height above the ground. This means that if a snow layer moves higher, then the portion that belongs in the next time step to the layer below is assigned to the layer below. In this way the aerosols "sink" into a deeper layer. Fig. 3.9a shows an example of the "sinking" of mineral dust from the first into the second layer. In case of large amounts of snowfall, the aerosols can also "jump" over adjacent layers. Here, it must be pointed out again that the aerosols do not actually migrate by themselves, but are pushed up and down among the layers by the change in snow layer height. We further emphasize that the dust concentration in the snow layer is significantly reduced when the layer thickness increases significantly. This results from the assumption of equal distribution of the dust tracer within a layer. However, the total mass and number remains consistent. Fig. 3.9b shows an example of a melting snow pack where aerosols resurface and accumulate in the top snow layer.

3.4 Embedding the Interaction of Snow and Aerosol

We incorporate the interaction of the optical properties of mineral dust and snow at the top of the snow pack, adjoining the atmosphere. This interaction happens in the model from the top to a defined snow depth dzh_{snow}. The thickness of the top snow layer can be adjusted by defining a threshold of the top snow layer (dz_{max}) in the simulation settings (namelist parameter: max_toplaydepth). The depth of the interactions of optical properties of mineral dust and snow is linked to this thickness ($dzh_{snow} = dz_{max}$). We made this decision to reduce computation time and to combine all required properties for further calculations in a single snow layer for most of the snow covered surfaces. If the top snow layer is, however, less then dz_{max}, the layers below are also taken into account to fill dz_{max} ($dzh_{snow} = dz_{max}$). If the sum of all snow layers h_{snow} is still less than dz_{max}, then the complete snow cover is considered for the optical interaction ($dzh_{snow} = h_{snow}$). In this study, the top layer is restricted to a height of $dz_{max} = 10\,\text{cm}$. According to Wiscombe and Warren (1980), the modification of the snow albedo due to aerosols is carried out by weighted averaging of the extinction cross sections and scatter cross sections using the total cross sections as weighing factors. The new averaged extinction cross section $\sigma_{ext,mix}$ is therefore defined by

$$\sigma_{ext,mix} = \frac{\sum_{l=1}^{3} k_{e,l} M_l + \sigma_{ext,snow} N_{snow}}{N_{snow} + \sum_{l=1}^{3} N_l}. \tag{3.32}$$

Here, we consider all three dust modes denoted by l. The aerosol properties are discussed in section 2.2. The number of optical equivalent snow grains N_{snow} is defined by

$$N_{snow} = \frac{\rho_{snow}\, dzh_{snow}}{4/3\,\pi\, {r_{snow}}^3\, \rho_{ice}}. \tag{3.33}$$

Combining Eq. 2.8 and 2.9 the averaged scatter cross section of the snow-dust mixture $\sigma_{sca,mix}$ is analogous to $\sigma_{ext,mix}$ defined by

$$\sigma_{sca,mix} = \frac{\sum_{i=1}^{4} \sigma_{sca,i} N_i}{\sum_{i=1}^{4} N_i}, \tag{3.34}$$

where i denotes every component (each dust mode and the snow) and N_i the number of the component. The asymmetry factor of the snow-dust mixture g_{mix} is averaged using the ratios of the individual total scatter cross sections of each component i in the total scatter cross section of the snow-dust mixture and the individual asymmetry factor g_i, where

$$g_{mix} = \sum_{i=1}^{4} \frac{\sigma_{sca,i} N_i}{\sigma_{sca,mix} N_{mix}} g_i. \tag{3.35}$$

The total number of dust and snow particles is denoted by N_{mix}. The averaged single-scattering albedo $\widetilde{\omega}_{mix}$ is calculated from the cross sections following Eq. 2.9. We calculate the averaged coefficients $\sigma_{ext,mix}$, $\widetilde{\omega}_{mix}$, and g_{mix} for the 18 Streamer bands, for every cell in which aerosols are present in snow. These variables replace the clean snow counterparts in the albedo calculation described in section 3.2.2. The result is the averaged albedo of mineral dust and snow per spectral band, as illustrated in Fig. 3.10. These spectral albedo values are then integrated to the two broad band albedos (VIS and NIR).

The single-scattering albedo $\widetilde{\omega}$ describes the relationship of scattering compared to the total extinction of a particle. This means that the albedo is high when $\widetilde{\omega}$ has a value close to 1. In contrast, if $\widetilde{\omega}$ is below 1, this means that the extinction of radiation energy is partly caused by absorption. Fig. 3.11 shows the single-scattering albedo of snow with an optical equivalent snow grain radius of 100 µm and the single-scattering albedos of the 3 mineral dust modes in ICON-ART (dust a, dust b, dust c). The figure shows that snow and mineral dust have opposite behaviors regarding the spectral range of shortwave radiation. Snow has a high single-scattering albedo at shorter wavelengths but a decrease towards longer wavelengths. Mineral dust particles have a lower single-scattering albedo at shorter wavelengths and a higher scattering-albedo at longer wavelengths. This is the reason why the impact of mineral dust is the strongest at shorter wavelengths.

Our computations relate to an external mixing of snow and mineral dust. It needs to be pointed out that the external mixing is mostly apparent when dust deposits under dry conditions. In the case of wet deposition, internal mixing occurs. A couple of studies investigated the snow-darkening effect of internally mixed aerosols in snow and found out that the darkening is further enhanced due to internal mixing (Flanner et al., 2012; Shi et al., 2021). This study does not account for internal mixing.

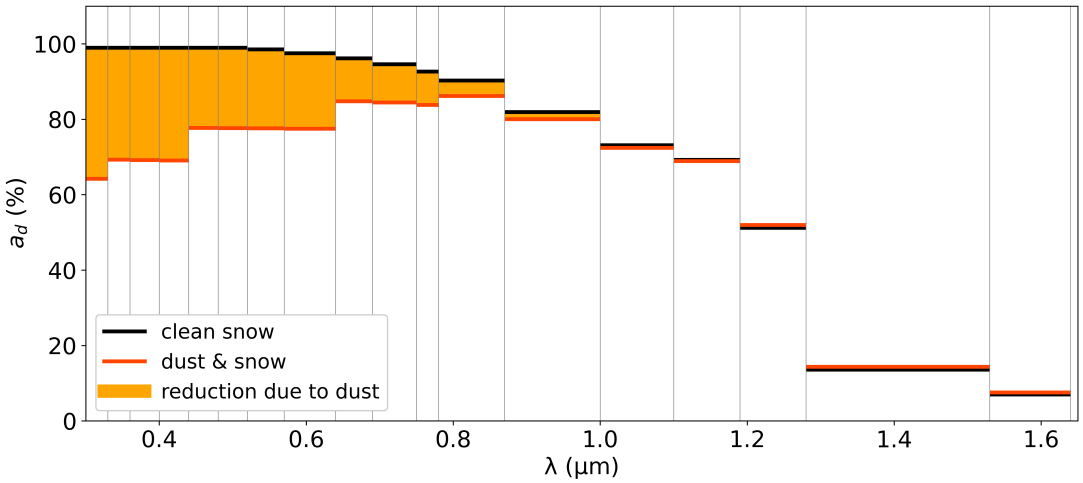

Figure 3.10: Diffuse snow albedo a_d in the 18 Streamer bands for clean snow (black) and a mixture of 7.2 g m^2 dust in the upper 10 cm of a semi-infinite snow layer with a snow density of 100 kg/m^3 and an optical snow grain radius of 100 µm at wavelengths λ between 0.30 µm and 1.65 µm.

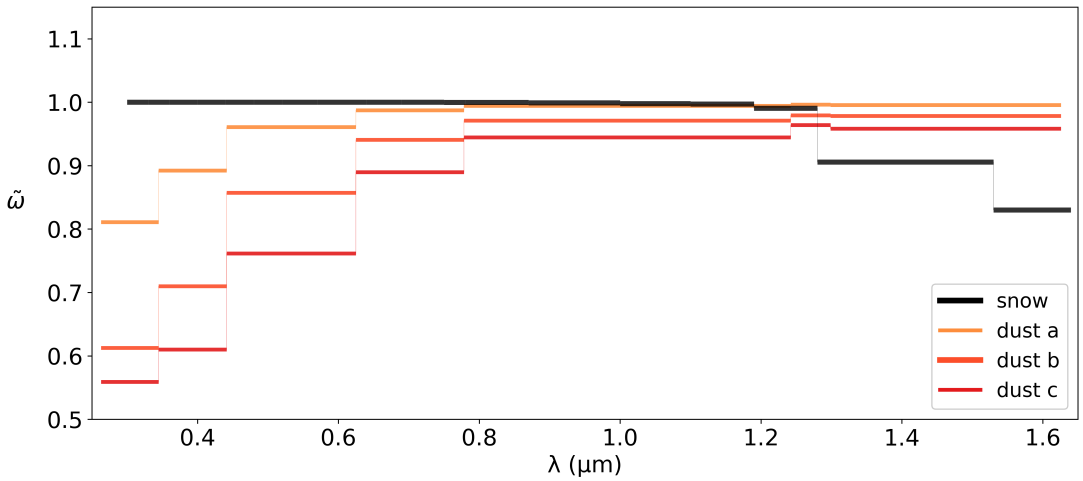

Figure 3.11: Example of the single-scattering albedo $\widetilde{\omega}$ of snow with an optical equivalent snow grain radius of $r_{snow} = 100$ µm (black) and dust particles (orange-red) at wavelengths λ between 0.30 µm and 1.65 µm.

4 Evaluation of the Optical Properties of Pure Snow

Prior to the investigation of the influence of dust on the snow albedo, in this section the newly implemented parametrization of the aging of snow and the spectrally integrated albedo of clean snow is tested against observational data. Snow aging has a considerable impact on the snow albedo, especially in the near-infrared region. Comprehensive long-term measurements of the optical properties of snow are rare. Especially when it comes to the optical equivalent snow grain size. The 2018 Polar Airborne Measurements and Arctic Regional Climate Model Simulation Project (PAMARCMiP) represents a special opportunity. The reason is that extensive measurements of the optical properties of snow were performed over three weeks in the framework of this project. These are recent measurement data, which were carried out with state-of-the art measuring instruments. The influence of the ground albedo and rainfall can be excluded in this case. The simulated snow aging is compared using the optical equivalent snow grain radius. Furthermore, the spectrally integrated snow albedo is compared with broadband albedo measurements conducted at the same site.

4.1 Measurements and Climate Model Simulation Project PAMARCMiP

PAMARCMiP was conducted in Greenland in 2018 with the purpose to gather information on snow and sea ice properties from measurements and models to quantify the interaction of aerosol, optical properties, and clouds in the Arctic region (http://www.ac3-tr.de/overview/observations/pamarcmip-2018). Many different measurement methods and techniques as well as model simulations were applied, focusing on the period from March 10 to April 8, 2018 at the Villum Station (81°36′ N, 16°40′ W) in Greenland. This included the application of ground measurements and airborne measurements, which were further evaluated against satellite data (e.g., Carlsen et al., 2020; Nakoudi et al., 2020). The ground-based measurements regarding the optical properties of snow were conducted using an IceCube instrument (Gallet et al., 2009).

The instrument illuminates a snow sample with a laser diode at a wavelength of 1310 nm. The radiation is reflected by the snow sample and then redirected via an integrating sphere to a photodiode which generates a voltage from the incoming signal. A calibration curve is then used to determine the ratio of the reflected to the emitted radiation. This ratio is then used to determine the SSA_M using a radiative transfer model. For the comparison of the simulation results, the SSA_M is transformed into the optical equivalent snow grain radius r_{snow} via Eq. 3.3. The accuracy of the obtained SSA_M with this technique for a range below $60\,\mu m^2\,kg^{-1}$ is about 10 % (Gallet et al., 2009).

The SSA_M measurements took place between March 19, 2018 and April 4, 2018, where 50 samples were taken each day along a 100 m line in close proximity to the Villum station (about 2 km away). In addition, a pair of pyranometers, one pointing downward and one pointing upward, were used to measure the broadband surface albedo. The instruments were located close to the SSA_M measurements.

4.2 ICON-LAM Simulation of Greenland

The simulation of the evolution of the snow grain radius was run in an ICON-LAM setup. The novel implemented parametrization of the snow albedo from section 3.2 was applied here as well. The developments described in section 3.4 do not contribute in this case and no mineral dust was emitted in the simulation. Only the parametrization of the aging of the snow grains, as well as the new optical properties of unpolluted snow were tested in this case study. The initial data as well as the boundary data are remapped data from the Integrated Forecast System (IFS) of the European Centre for Medium-Range Weather Forecasts (ECMWF). The interval between the forcing of the boundary data is 6 hours. The simulation domain extends along longitude degrees from 92° W to 12° E and along latitude degrees from 89° N to 55° N. The simulation was run at two different horizontal resolutions, namely R3B08 ($\sim 6.6\,\mathrm{km}$) and R3B09 ($\sim 3.3\,\mathrm{km}$). Both simulations had very similar results and therefore only results of the simulation with higher resolution (R3B09) are presented here.

In this evaluation, different parametrizations were tested to fit the observations obtained during PAMARCMiP. First, a slightly modified version of the parametrization of Essery et al. (2001) was applied, corresponding to Eq. 3.6 and Eq. 3.7. The impact of rainfall on the growth of snow grains was also included but does not play a role in this simulation because of the fact that the 2m-temperature was constantly below $-25\,°\mathrm{C}$ during measurements. The mean optical grain radius obtained from the measurement on the first day (March 19, 2018) is $44.03\,\mu\mathrm{m}$, and the original parametrization does not allow values below $50\,\mu\mathrm{m}$. Therefore, we modified the allowed range of the optical snow grain radius. Briefly before the first measurement, there was heavy snowfall, allowing the assumption that on the day of March 19 the surface was covered by fresh snow, with very small snow grains. Therefore, we lowered the range of values for the optical equivalent snow grain radius to $40\,\mu\mathrm{m}$, and the snow in the Arctic region was initialized with $43\,\mu\mathrm{m}$ at the start of the simulation. Another modification is the reduction of the required snow mass d_0 for the refreshment of the snow grain size. This was reduced to $1\,\mathrm{kg\,m^{-2}}$ (instead of $2.5\,\mathrm{kg\,m^{-2}}$) in order to reunite measurement and simulation during snowfall.

As the case study results below show, these efforts of adjusting the parametrization are unfortunately not sufficient to provide a satisfactory fit of the modeled snow grain size to the observations. Consequently, instead of fitting d_0, we extended the growth factor G_r (Eq. 3.6) using data from a measurement study for a temperature range that applies to the Arctic region. Kaempfer and Schneebeli (2007) performed X-ray microtomography to measure SSA_V of 4 samples that were kept at 4 different constant temperatures (-1.6, -8.3, -19.1 and $-54.0\,°\mathrm{C}$) for almost a year. The values were measured 7 times and fitted to an aging parametrization that can be found in Figure 6 of Kaempfer and Schneebeli (2007). For the comparison with the parametrization in ICON-ART, the SSA_V was transformed into the optical equivalent snow grain radius using Eq. 3.2. Fig. 4.1 shows the measurements, translated to optical snow grain size, where markers show the individual measurements, and lines indicate the fit by Kaempfer and Schneebeli (2007).

The snow samples were kept in a temperature controlled cold room which eliminates the impact of rain or snow fall and leaves only the equi-temperature metamorphism. Therefore, the growth factor G_r can be reduced to

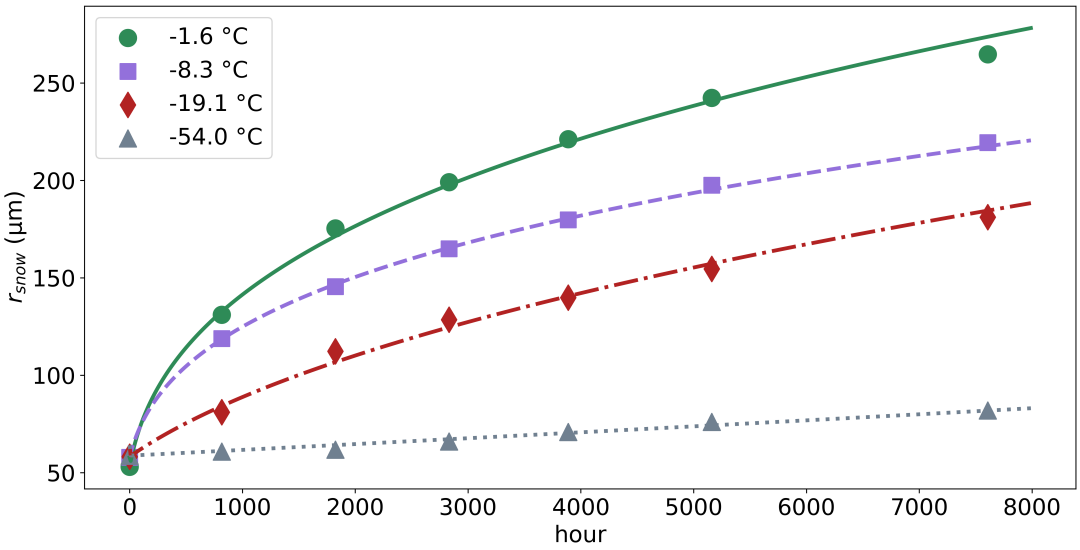

Figure 4.1: Converted optical equivalent snow grain radius r_{snow} of four snow samples that were kept at constant -1.6, -8.3, -19.1, and $-54.0\,°C$ (sample 1, sample 2, sample 3, sample 4) from 7 SSA_V measurements (markers) during a year and respective fit (lines) (modified from Kaempfer and Schneebeli, 2007).

.

$$G_r = \frac{\pi({r_{snow}}^2 - {r_{snow,t-1}}^2)}{\Delta t}. \tag{4.1}$$

To acquire G_r from the fit shown in Fig. 4.1, we extrapolated two optical equivalent snow grain radii $r_{snow,t-1}$ and r_{snow} for every time step Δt from the fit. This gives the needed data to insert in Eq. 4.1 to obtain G_r for every timestep Δt. Since the growth factor dependent on current grain radius is needed for the parametrization in ICON-ART rather than the time dependent growth of this particular experiment, we sorted the growth factor by the respective grain radius. Fig. 4.2a shows the fitted functions of growth rate for the four samples dependent on the respective snow grain radius r_{snow}.

In a third simulation, the newly derived growth factors were raised in turn for a temperature range between $-54.0\,°C$ and $-19.1\,°C$ by $0.008\,\mu m^2\,s^{-1}$ and in the temperature range between $-19.0\,°C$ and $-1.6\,°C$ by $0.01\,\mu m^2\,s^{-1}$. The straightforward use of the derived growth factors lead to an underestimation of the optical grain size which is discussed below. Furthermore, the last modification lead to the best agreement with the observations with the measurements in Greenland. The resulting final growth factors were already mentioned in section 3 and are implemented in ICON-ART for further simulations. The temperatures -1.6, -8.3, -19.1, and $-54.0\,°C$ correspond to 271.55 K, 264.85 K, 254.05 K, and 219.15 K. An illustration of the final growth factors as a function of optical grain radius and dependent on snow temperature can be found in Fig. 4.2b. If data are available, this parametrization should be revisited with additional temperature ranges and environmental conditions.

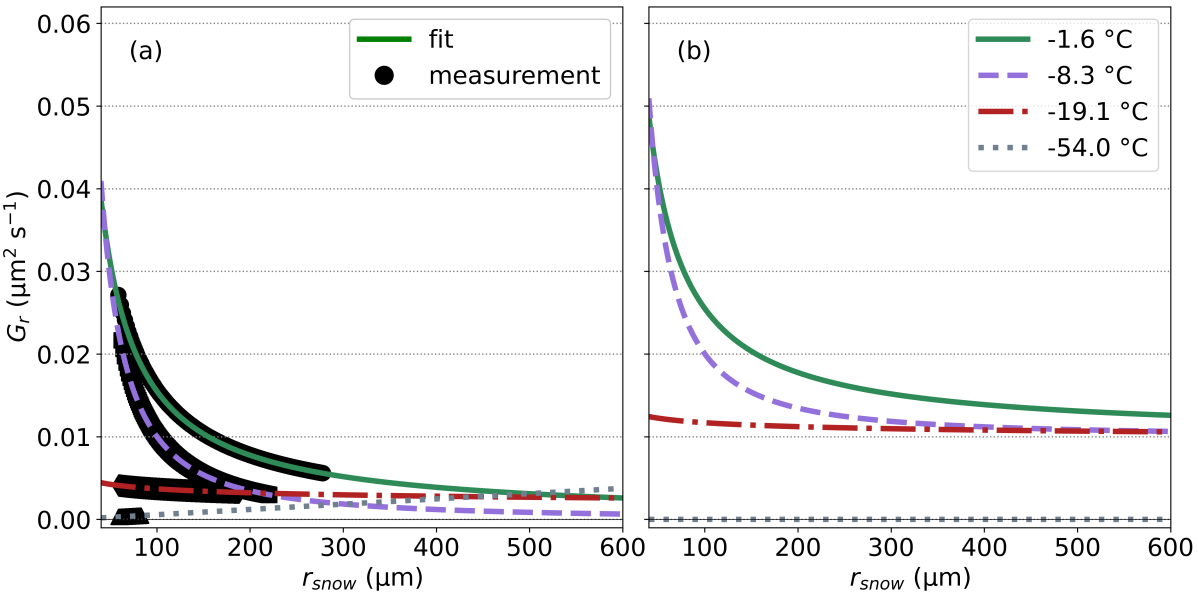

Figure 4.2: Growth rates G_r in µm^2 s^{-1} dependent on snow grain radius r_{snow} in µm at four snow temperatures (−1.6, −8.3, −19.1, and −54.0 °C) calculated on the basis of measurements from Kaempfer and Schneebeli (2007) (a) and modified growth rates leading to best agreement of the evolution of optical equivalent snow grain radius to observations in Greenland (b). Markers show the growth rates calculated in the measured range and the lines show the fit for a snow grain radius range between 50 and 600 µm.

4.3 Comparison of Measurements and Simulation Results

Fig. 4.3 shows the simulated evolution of the optical equivalent snow grain radius (simulation 1) using the slightly modified parametrization that originate from Essery et al. (2001). On the one hand, the red dashed curve shows the simulated optical equivalent snow grain radius for the cell where the Villum station is located in. The black dots, on the other hand, show the mean value of the IceCube measurements near the station. The corresponding bars represent the range of all measurements along the 100 m line on the particular day. During the measurements, two periods were noted during which no snowfall was observed. These periods of time are shaded in gray color. For comparison with the simulated snowfall, there are blue bars representing the snowfall rate in the corresponding cell among the simulation.

The simulated periods of snowfall and the observed snowfall days correspond relatively well. The absence of snowfall makes the equi-temperature metamorphism emerge as the dominant influence on the optical grain size. The observed average snow grain radius increases by a few micrometers on March 19 before it decreases again through March 24 as a result of new snowfall. After that, the first phase of the growth of the mean snow grain radius begins and persists until March 30. Snowfall was again observed throughout one and a half day to the morning of April 1 before the second phase of growth begins. The simulation results show a similar behavior of the optical snow grains. The first growth phase starts slightly earlier, already in the night from March 22 to 23 and ends slightly earlier than the observations in the night from March 29 to 30. After that, the time window of precipitation until April 1 is similar in the two data, and the second growth phase starts also on April 1. Again, snow fall starts slightly earlier

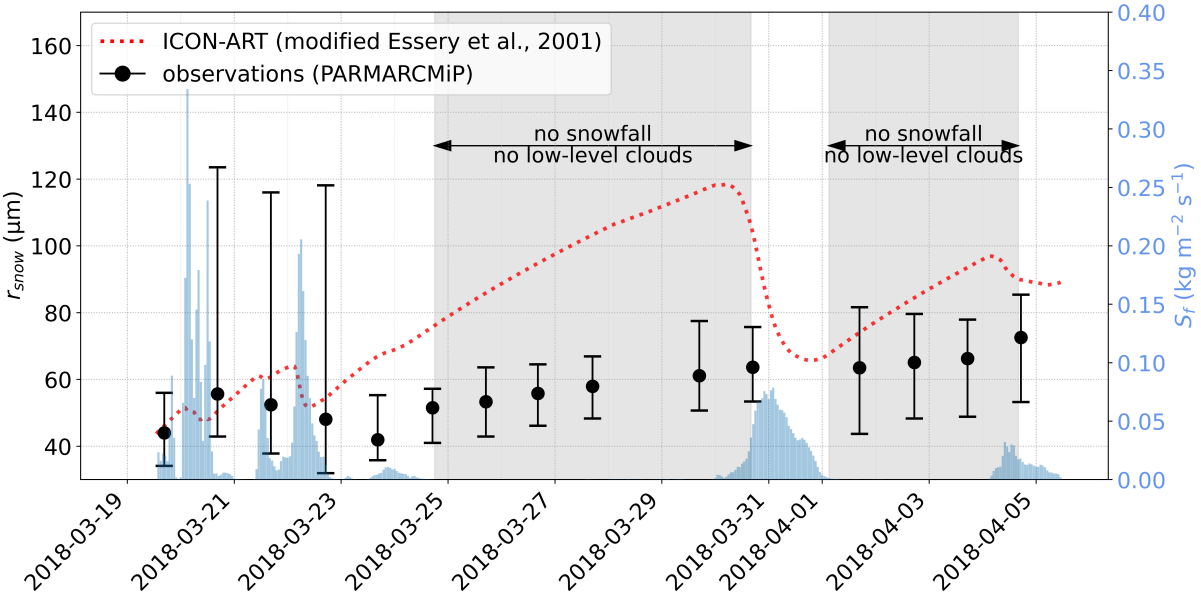

Figure 4.3: Simulated evolution of the optical snow grain radius r_{snow} as red dotted line in comparison to the measurements during the PAMARCMiP campaign. The black dots mark the average of 50 measurements during the day along a 100 m line. The gray areas indicate the periods of time during which there was no precipitation observed while the blue bars show the snowfall rate S_f in the simulation.

in the simulation in the morning of April 4, whereas observations of snow fall are first noted at the end of April 4.

The first simulation results show that the inital parametrization of snow aging with growth rates by Essery et al. (2001) overestimate the growth of the snow grains. While the mean value of the daily observations of the optical grain radius ranges from 41.9 to 72.6 µm, the simulated values range from 43.7 to 118.5 µm. The two sets of data correlate with a Pearson correlation coefficient $R_{pears} = 0.62$ and the root-mean-square error RMSE is 28.6 µm. The results of the simulation using the growth factors derived from Kaempfer and Schneebeli (2007) (simulation 2) as well as the results of the simulation considering the final growth factors (simulation 3) are additionally displayed in Fig. 4.4. The direct application of the derived growth factors (simulation 2) leads to an underestimation of the optical grain sizes. The correlation coefficient of $R_{pears} = 0.85$ for this data set is significantly better in comparison to the observation, as is the RMSE (10.4 µm). However, the third simulation with the use of the complete modified set of growth factors (Eq. 3.8) results in the best agreement. The correlation coefficient is 0.83 and the RMSE is reduced to 4.8 µm.

The simulated diffuse broadband albedo of the cell containing the Villum station (red curve) and the total broadband albedo measured on site (black dots) are depicted in Fig. 4.5. All simulated hourly values at daytime are shown and for ease of comparison, the red dots mark the simulated value at the corresponding observation time. As described in section 3.2.3, the albedo is required by the RRTM for the spectral bands VIS and NIR. The newly introduced spectrally higher resolved snow albedo is therefore integrated to these bands before being passed to the RRTM. The radiation fluxes at the surface calculated by the RRTM are considered in the integration. In this manner, a new weighting of each spectral band of the

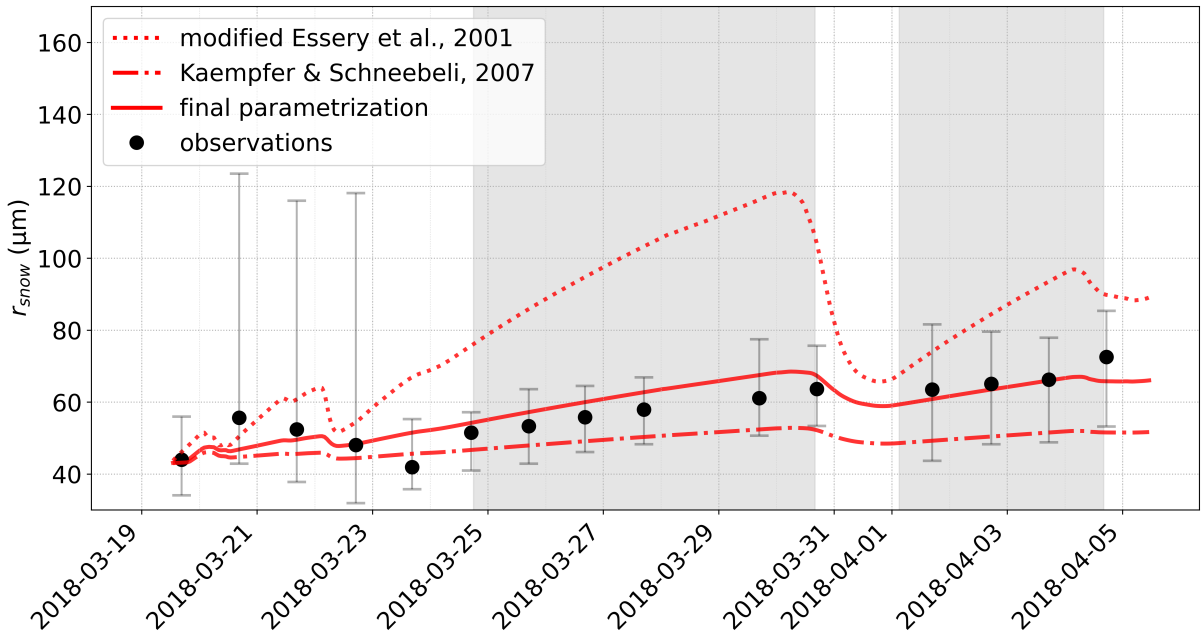

Figure 4.4: Simulated evolution of the optical snow grain radius r_{snow} with different growth rates in comparison to measurements from PAMARCMiP. The red dotted line shows the evolution considering a modified version of the parametrization of Essery et al. (2001), the dashed line shows the evolution with adapted growth rates from measurements conducted by Kaempfer and Schneebeli (2007), and the solid line shows the evolution of the set of growth rates with the best fit. The black dots mark the mean of the observations and the gray areas indicate the periods of time during which there was no precipitation observed.

snow albedo is computed for each update of the radiation in the model. Over the course of the day, the snow albedo therefore varies strongly with the diurnal cycle and atmospheric conditions.

The measured broadband albedo varies over the observation period between 79.6 and 91.7 %. The simulated diffuse broadband albedo varies between 80.4 and 90.3 %. The observed broadband albedo during snowfall is relatively high and during the non-precipitation periods significant lower. The variability during the snowfall phases after the third day agrees well with the observations. The RMSE calculated without the gray shaded periods results in 3.2 %. During the growth phases (gray shaded area), there is less agreement, and the simulated diffuse snow albedo is strongly overestimated with an RMSE of 6.8 %.

To demonstrate the aspect of online integration of the spectral snow albedo, an alternative snow albedo (red curve and red dots) is presented in Fig. 4.6. The observations (black dots) are also shown for comparison. For this alternative snow albedo, the energy fluxes of the RRTM are not considered in the integration. Instead, fixed weighting factors are used, which can be found in Tab. 3.1. These weighting factors are used for the dummy albedo at night. Furthermore, these weighting factors are used for the integration from the Streamer to RRTM bands. The model does not calculate this alternative albedo in the case of solar irradiance. The results presented here provide a theoretical albedo for comparison.

The figure shows that the evolution of the alternative snow albedo solely results from the age parametrization. Here, the albedo changes step wise due to the growth of the snow grains. When the grains reach a size that is associated to another category of the implemented LUT, the optical properties of snow change instantly. The fluctuations that occur during the day in Fig. 4.5 do not occur here. The

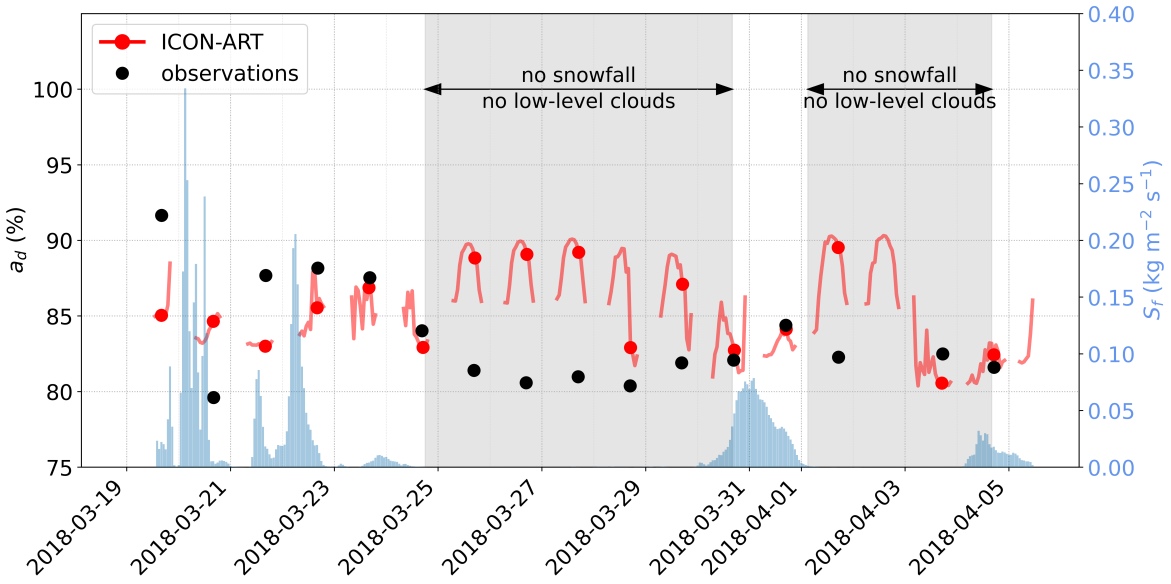

Figure 4.5: Online spectrally integrated diffuse snow albedo a_d (red line) compared to PAMARCMiP observations (black dots). Gray areas indicate the precipitation free periods. Blue bars show the simulated snowfall rate S_f.

overestimation on days without precipitation is less pronounced. Fig. 4.6 shows that the diffuse albedo is greater during phases of snow fall, when only considering the grain size influence. This behavior is also present in the observations. However, the variability in observational data is greater. During the first snowfall phase, the modeled diffuse snow albedo is approximately at a value of 87.7 % and decreases to 86.3 % during the first growth phase. During the second snowfall phase the snow albedo rises again to 86.9 % and reaches the lowest value of 86.3 % again towards the end. In this sensitivity study, the root-mean-square error of the modeled snow albedo compared to the observations is 4.5 µm with a correlation coefficient of $R_{pears} = 0.73$.

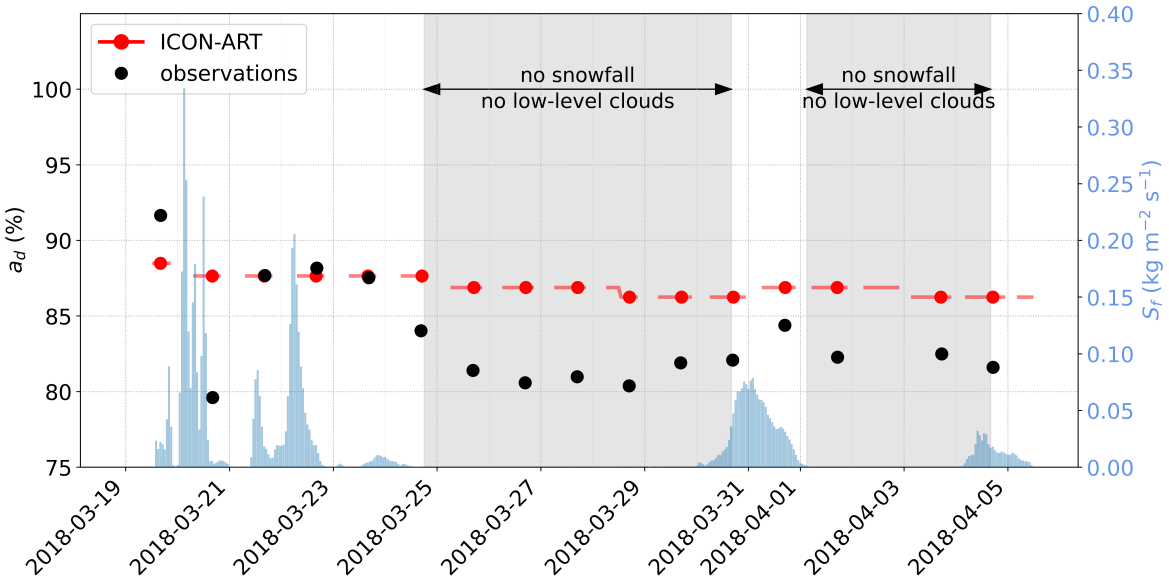

Figure 4.6: Alternative diffuse snow albedo a_d without online spectral integration (red line) compared to PAMARCMiP observations (black dots). Gray areas indicate the precipitation free periods. Blue bars show the simulated snowfall rate S_f.

4.4 Discussion

The measured optical snow grain radius was surprisingly small, with a minimum of the daily averages of 41.9 µm. This grain size range is not represented in many snow models (Essery et al., 2001; Flanner and Zender, 2005). Therefore, the parametrization had to be adapted to the Arctic conditions. The parametrization as described by Essery et al. (2001) distinguishes only between growth below and above the melting point at a grain radius smaller than 100 µm. Already Kaempfer and Schneebeli (2007) showed in their study that the isothermal growth of snow grains is strongly dependent on the snow temperature. The results of their experimental study is significant for understanding the part of metamorphism concerning isothermal growth, which was the main purpose of their study. However, snow metamorphism involves several other processes that are not present in the sterile environment of a cold room. A few examples of these processes are namely the absorption of solar radiation, the vertical temperature gradient, the humidity, the wind and snow compaction (e.g., Colbeck, 1987; Brun et al., 1992; Flanner and Zender, 2006). This fact explains why the derived growth rates of Kaempfer and Schneebeli (2007) lead to a strong underestimation of the growth in the outdoor environment. However, the adaptation of the classification of the growth rates according to the different temperature ranges leads to a much better correlation and a closer alignment with the observations. Increasing the growth rates by 0.008 µm^2 s^{-1} (between −54.0 °C and −19.1 °C) and by 0.01 µm^2 s^{-1} (between −19.0 °C and −1.6 °C) leads to the best agreement of the simulated evolution of the grain size with the observations.

Fig. 4.5 demonstrates that there is a great spatial variability in the first days of the measurements. For example, on March 22, the largest difference within the sampling area of 100 m (50 samples) is 86.2 µm. It must therefore be emphasized that the comparison of the model result at a horizontal resolution of 3.3 km to a sampling area of 100 m, with a quite large variability, is not trivial. Nevertheless, ICON-ART is able to simulate the precipitation events and thus, the growth phases are relatively accurate. With

an RMSE of 4.8 µm and a correlation coefficient $R_{pears} = 0.83$, ICON-ART is also able to reproduce the evolution of the optical equivalent snow grain radius. If available, the growth rates can be further adjusted for other temperature ranges.

In this case study, the simulated diffuse snow albedo can be divided into two categories with respect to its agreement with the measured values. The simulated diffuse albedo is relatively close to the observed broadband albedo during the phases of snowfall and cloud cover. The online weighting of the individual spectral bands used for the integration of the spectral albedo plays an important role here. Using only the fixed weighting, listed in section 3.2.3, the albedo does not vary over the course of the day due to the atmospheric conditions (alternative albedo). In this case, the solitary determining factor is the optical snow grain size of the snow. The simulated alternative snow albedo does not fall below a value of 86 %, and therefore greatly overestimates the albedo compared to the measurements. Considering the alternative albedo, the variability is much smaller, but the influence of snow aging is visible, and the snow albedo decreases during the precipitation-free phases. However, since the fixed weighting was calculated for a specific location and time of year (midlatitude winter), these values are only approximately valid for that specific location during that specific atmospheric condition. The weighting will vary depending on atmospheric conditions and location. The purpose of the fixed weights is to prevent model errors in the case that not enough radiation reaches the surface to perform the online calculation of the spectral weights.

Throughout the day, the diffuse albedo with online integration varies over several percent. The snow albedo increases with cloud cover, since the clouds absorb mainly in the near-infrared region where the snow albedo is quite low (Warren and Wiscombe, 1980; Warren, 1982; Gardner and Sharp, 2010). The result is that relatively more radiation at shorter wavelengths reaches the surface, and as shown in section 3.2.3, the weights shift to a range where the snow albedo is very high. Furthermore, Freese and Kottmeier (1998) tested the wavelength-dependent changes in albedo with a 4-band model in relation to different cloud types. The focus of their study is the importance of multiple scattering between stratus clouds and polar marine surfaces. They found that for thick clouds (400 and 900 m), the optical properties differ by less than 1 %. However, for thin clouds (100 m), the errors of snow optical properties become larger. For the asymmetry factor, the errors increase up to 1.5 %. Warren (1982) and Grenfell et al. (1981) pointed out that under overcast, the albedo can be about 1–9 % higher than under clear-sky conditions.

Furthermore, there is a strong dependency of the snow albedo on the solar zenith angle. The spectral snow albedo increases with solar zenith angles since the radiation penetrates less deep into the snow at a low angle and more radiation is scattered. The effective solar zenith angle of the diffuse albedo is 50°. Under cloudy conditions with especially high zenith angle as in the Arctic region almost all direct radiation is transformed into diffuse radiation, and therefore counteracting the increase in albedo through cloud cover (Warren and Wiscombe, 1980). This feature is not represented in the shown simulated snow albedo, since only the diffuse snow albedo was presented here. This effect could be present in the results of the measurements and explain the deviations of the modeled albedo in the first days. Furthermore, a thin crust of ice was reported on the first day, with a thin layer of fresh snow forming on top. It cannot be ruled out that reflections from ice, comparable to a mirroring effect which occurs at low sun, contributed to the extremely high measured snow albedo on the first day. On the second day, it was reported that the

ice crust was uncovered. Ice has a much lower albedo as it is a stronger absorber which explains the low albedo on the second day. Unfortunately, ICON-ART is not able to capture the impact of forming ice crusts.

The modeled diffuse snow albedo agrees poorly with observations during the phases when low-level clouds and snowfall are absent (March 25 – March 29 and April 1). The simulated albedo clearly overestimates the measurements and is actually higher than the simulated values during cloudy periods. This may be due to a number of reasons. One might be that the high clouds in the simulation differ from the apparent conditions, and therefore the absorption in the atmosphere occurs in different bands. Another reason could be that the composition of the atmosphere in the Arctic region is not well represented, so that the absorption spectra of the components lead to a different weighing of the spectral bands. When too much absorption takes place in the near infrared range relative to the shorter wavelengths, then the spectral albedo is higher. A small test of the different predefined ICON-ART aerosol and gas concentration settings showed a difference of several percent in the spectral albedo during the hours where the online weighting is applied. Further investigations regarding the absorption of gases and evaluation with albedo measurements at other locations may provide more insight into what is causing the deviation in the clear-sky spectral albedo in Greenland. Due to the large amount of data required for this, which is unfortunately not available to us, the deviation cannot be completely explained at this point.

In conclusion, the modeled diffuse snow albedo during cloud cover and snowfall is promising and fits relatively well with the observations. The online weighting of the individual spectral bands is extremely important, since the diurnal cycle and atmospheric conditions as described above have an influence on the spectral albedo. The new parametrization is in addition considerably more realistic, since the broadband albedo in ICON-ART was limited in the previous parametrization to a maximum value of 85 %. In both the observations and the simulation, snow albedo is observed to exceed 90 %.

5 Case Study: Saharan Dust Outbreak in Spring 2018

The validation of the developments requires many parameters and data, which so far are only available for individual cases. To investigate the feedback of dust deposition on snow, a particularly intensive event was selected. In March 2018 pictures from a major dust deposition event flooded the news. One of the regions that got the most attention was the Caucasus where many Ski Resorts reported red or pink snow. A few studies followed this event that investigated the meteorological phenomenon that caused this event (Solomos et al., 2018; Barkan and Alpert, 2020). Barkan and Alpert (2020) used the National Center for Atmospheric Research (NCAR) reanalysis, the Moderate Resolution Imaging Radiospectrometer (MODIS) on board the TERRA satellite and the Hysplit back trajectory model for 60 h. A cold through extended from Scandinavia to Western Sahara. This caused a severe dust storm that lifted huge amounts of Saharan dust in the air. Southwesterly flows transported the mineral dust particles within two days to Eastern Europe. In the morning of March 23, 2018, the dust deposited together with snow which led to the phenomenon of a red snow cover. Samples taken near Bucharest in Romania on March 24, allowed the source of the dust to be identified through a chemical composition analysis as the Northern Sahara (Marmureanu et al., 2019).

The transport of Saharan dust to Europe is quite common in spring time (Kutuzov et al., 2013). This event was unique in the sense that the dust was carried particularly far to the east, where a greater amount of snow is present compared to Western and Central Europe. Dumont et al. (2020) used this opportunity to investigate the impact of the dust on the spring snow melt in the Caucasus Mountains. They report on two snow samples of the top 10 cm at a station at Roza Pik (2300 m a.s.l.) in the Russian Caucasus. They were obtained on March 27, 2018, and contained mineral dust concentrations of 606 and 786 ppm. Furthermore, they investigated this event using the one-dimensional snow model scheme Crocus to simulate the snow cover and the impact of the mineral dust during this extreme event at different locations in the Caucasus. Since their model was not coupled to an atmosphere model but rather forced by meteorological data, the dust was introduced to the snow layers at a small constant rate and one additional wet deposition event on March 23.

In contrast to the previous studies, the analysis presented here is the first to use a fully coupled atmosphere-land-snow system with an online aerosol transport model to investigate the dust event in March 2018. The interaction of the optical properties of snow and mineral dust is calculated online and the advantage of this is that the interactions have a direct influence on the atmosphere and feedback can be studied. In contrast to the study by Dumont et al. (2020), the focus is on short-term impacts on the snow cover. Moreover, not only the shortwave radiation impact and the snow melt out is considered but also the surface temperature and the 2m-temperature. In addition, different from climate modeling, this study uses the ICON-ART LAM setup to achieve high spatial and temporal resolution so that local effects can be investigated.

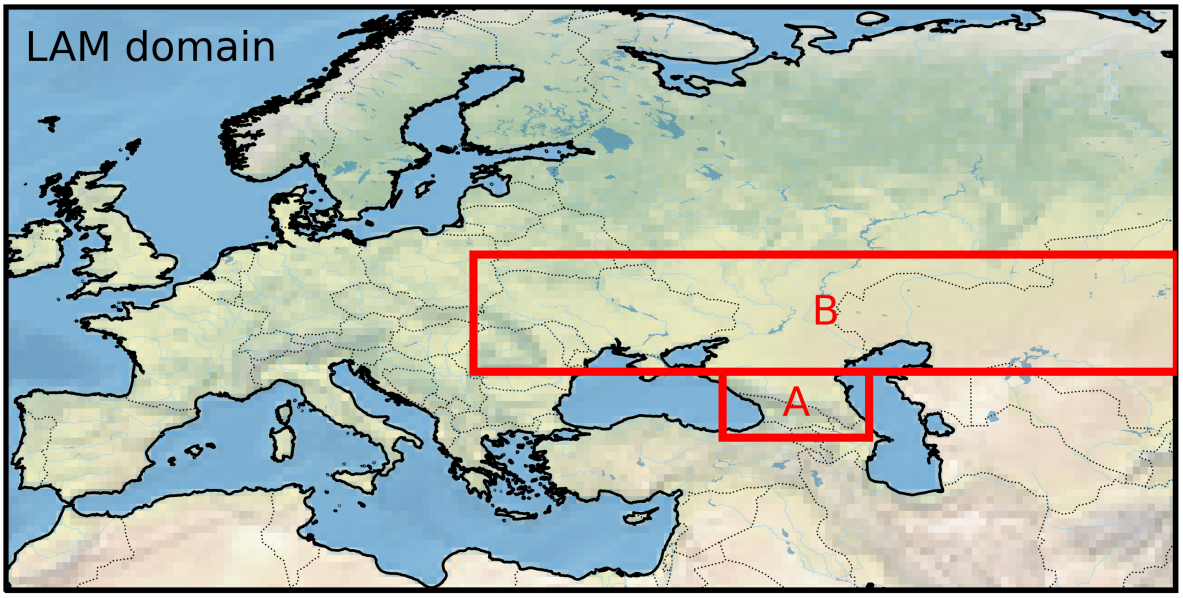

Figure 5.1: ICON-LAM study region with outlines of region A including the Caucasus Mountains and region B containing the moving snow line during spring time melt in March 2018.

5.1 Ensemble Simulation Setup

The simulation of the dust event ran in a global set up with a horizontal resolution of about 40 km (R2B06) and covered the time period of March 22, 0 UTC, 2018 to April 1, 0 UTC, 2018 (10 days). At start of the simulation, the model was initialized using two different sources. The meteorological state was initialized using ECMWF IFS data from March 22, 2018 0 UTC. The mineral dust data originates from the Experiment 10517 of the ICON-ART mineral dust forecast by the DWD. The simulation ran independently throughout those 10 days without reinitialization. Due to the fact that both the deposition and the snow cover are strongly dependent on the terrain and are spatially highly variable, the resolution of 40 km was further increased. For this purpose, the LAM setup was used for further investigation. The hourly results of the meteorological variables as well as the mineral dust of the global R2B06 simulation were used to force the smaller domain. The ICON-LAM domain extends over large parts of the snow-covered areas of Europe and Asia between 30°–70° N and 10° W–140° E. Since the impact of the dust event is expected in Eastern Europe and the western parts of Asia, only results up to 70° E longitude are presented here.

Fig. 5.1 shows the study region of the ICON-LAM domain and the two smaller regions where certain processes are investigated in more detail. Major mountain ranges of the simulation domain are labelled in Fig. 5.2. Region A covers the Caucasus Mountains, where the severe dust deposition event was reported (Barkan and Alpert, 2020; Dumont et al., 2020). Region B covers the snow line which moves towards the north due to spring melting processes. Here, the term does not refer to the snow line which indicates the lower limit of the snow cap at high terrain. Instead, the term meant here is the ever-changing equatorward limit of the snow cover. This snow line migrates due to seasonal changes. In cold seasons, this boundary lies further south, and in warm seasons, it lies in northerly territories. The ongoing melting

Figure 5.2: ICON-LAM study region with markings of the major mountain ranges.

during springtime makes the snow especially receptive for the influence of aerosol particles (Skiles and Painter, 2019). According to Lau et al. (2018), this is one of the main vulnerable regions to aerosol deposition on the Eurasian continent (see Fig. 1.5). The horizontal resolution of the LAM domain is approximately 10 km (R2B08) and the simulation covers 10 days from March 22, 2018 to April 1, 2018. To investigate the influence of mineral dust, the experiment was performed twice. There is the reference simulation (REF) that includes the aging of the snow and the newly implemented snow albedo described in section 3.1 and section 3.2 but not the interaction of the optical properties of mineral dust and snow described in section 3.4. In other words, dust is present in the reference scenario but it does not change the albedo. The snow is assumed to be clean. The second simulation has the same set up as the reference case but represents the snow-darkening simulation (SDS). Here, the interaction of dust and optical properties of snow is included.

As pointed out by e.g., Rahimi et al. (2020), the impact of aerosols on the snow albedo can be superimposed by model internal variability. To eliminate the effect, the pairwise LAM simulations were performed multiple times and bundled into one ensemble. The application of ensemble simulations is a well-established method, especially in the numerical weather prediction, where short time periods are computed at high resolution. An ensemble is used to generate a range of different possible outcomes and estimate the initial condition and model uncertainties. There are several ways to create an ensemble, such as changing the initial conditions, using different models, or as in this case, changing model internal parameters. In the following, a brief summary of the ICON in-built feature of the ensemble generation process and the application in this study is presented.

All members of the ensemble have the same initial meteorological conditions and start time, but the difference between the members is that the predefined set of physical tuning parameters of ICON-ART are perturbed at the beginning of the simulation. The ensemble generation process uses a random number generator that introduces a perturbation initiated by a seed. This seed can be defined for every single

member. Using the same seed for two simulations generates the same perturbations in these experiments. The perturbed tuning parameter p_{pert} is calculated from the default tuning parameter p_{def} in a variable specific threshold r_{pert}. The perturbed parameters are defined by

$$p_{pert} = p_{def} + 2\,(R_{seed} - 0.5) \cdot r_{pert}. \tag{5.1}$$

The random number R_{seed} ranges between 0 and 1 and is drawn from a uniform distribution, initialized by the individual ensemble member seed. Using the same seed for one REF and one SDS, generates the same perturbation and allows for a comparison of the scenarios. In this way, 40 pairs are generated with a total of 80 simulations. For the interpretation of the ensemble simulation, the average of the difference between the respective pairs is considered and shown in the figures below (SDS − REF).

The results are presented in three parts, each with a directly included discussion section. First, the overall temporal evolution of the ensemble simulation extending over the regions A and B will be presented. Region A covers the area between 40.5°–45° N and 39°–49° E. This area of investigation focuses on the influence of mineral dust during an extreme event in complex terrain. Region B extends over the area between 45°–53° N and 22°–70° E and includes the snow line. This region was chosen to study the general influence of the aerosol on the snow melt, as it is expected to be particularly strong here (Lau et al., 2018).

Subsequently, the spatial distribution and the elevation dependency will be investigated in more detail to reveal regional influences. The third part concentrates on the dependency of the feedback to the reduction in snow albedo and on the method to reduce the noise caused by natural variability. The whole study region between 30°–70° N and 10° W–70° E will be taken into account. For the second and third part, one specific point of time is considered in detail. The time frame t_{176} (at 176 hours simulation time) is on March 29, 2018, 8 UTC. A more detailed explanation for the selection of this date is given in the first section of results.

All variables with the exception of cloud cover and precipitation refer only to cells where at least one ensemble member off all SDS or REF simulations contains snow. Other cells that are completely snow free in all ensemble members are masked.

5.2 Temporal Variations of the Impact of Mineral Dust

The model starts with clean snow at the beginning of the simulation. Therefore, the progression of the deposition event and the short-term effects can be determined in the timeline of the results. Fig. 5.3 shows the hourly ensemble mean (line) and the respective standard deviation (shading) of the mineral dust mass in the top snow layer m_{dust}, the ensemble mean differences in SDS compared to REF (lines) and respective standard deviations (shading) in diffuse surface a_d, snow height h_{snow}, and precipitation rate P. The figure presents the temporal results of the smaller regions, which are separated in region A extending over the Caucasus Mountains (red) and region B focusing on the area of the snow line (blue).

The reported dust deposition event in region A is quite noticeable in the results. The dust loading starts to grow on March 23 and reaches the first maximum on March 24, 13 UTC with a mean dust loading of $0.63\,\mathrm{g\,m^{-2}}$. The precipitation rate increases after this point, but less dust is deposited leading to a

decrease in dust loading in the first layer. Despite the higher precipitation rate, the overall snow height decreases, which implies that snow free cells are newly covered by a thin snow layer. The decrease in snow albedo in SDS compared to REF increases simultaneously with the dust loading, reaching a value of $-1.19\,\%$ at the first local maximum of the dust loading. The albedo difference increases further throughout the following days and reaches the largest difference on March 28, 9 UTC with a mean reduction compared to REF of $-1.74\,\%$. The snow albedo difference varies during the day which is the result of the online weighting of the spectral albedo as well as the change in surface properties. The surface albedo is not shown for nighttime since it is only relevant during the day for the reflection of sunlight. The largest difference in albedo is mostly not developed around noon but has the largest value in the evening hours. Only on March 28 and 29, the largest difference forms during the middle of the day in region A. The mean reduction in albedo in region A is $-0.80\,\%$ and the strongest daily reduction in surface albedo is on March 28 with an averaged difference of $-1.50\,\%$.
After March 25, the precipitation rate decreases and the dust loading increases again. The mean dust loading of the cell close to Roza Pik during March 27 is $1.10\,\mathrm{g\,m^{-2}}$. The daily mean dust loading over the whole region A reaches a maximum on March 28 at 9 UTC ($0.92\,\mathrm{g\,m^{-2}}$), shortly before the snow height reaches its maximum value of 73.67 cm at 17 UTC at that day. A comparable local maximum is reached on the next day (March 29, 9 UTC) with a snow height of 73.05 cm. In the evening of March 29, the precipitation rate increases again and a thin clean snow layer builds up on top of the dust-contaminated snow as well as on former snow free cells. This is the reason why the overall snow height of the snow covered cells decreases rapidly and the mean dust loading of the top snow layer decreases at the same time. After that, the dust loading in the top snow layer does not exceed a value of $0.42\,\mathrm{g\,m^{-2}}$.
Region B shows less variability because it was far less affected by the Saharan dust event. The dust loading starts to build up on March 24 and keeps building up quite constantly reaching its maximum on March 31, 14 UTC with an average amount of $0.15\,\mathrm{g\,m^{-2}}$. The mean dust loading over the whole simulation in the top snow layer is $0.08\,\mathrm{g\,m^{-2}}$. The reduction in diffuse albedo of the snow cells of SDS compared to REF starts as well on March 24 simultaneously with the dust loading. The magnitude of the difference is much smaller compared to region A since region B covers a much larger area and the ratio of polluted snow to clean snow is a lot smaller. The results show a pronounced difference in surface albedo in the morning hours. This could be a model artifact because a fraction of the region is still dark in the morning and a different weighting of the albedo applies. During the night, fixed values are used for the weighting of the albedo to avoid model errors but do not affect the surface shortwave net flux. The largest daily difference in surface albedo is reached on March 30, with a mean reduction in SDS of $-0.93\,\%$. The snow height in region B is quite constant compared to region A but with a slight decreasing tendency. The maximum snow height is on March 24, 14 UTC (21.51 cm) and the most shallow mean snow height on March 31, 3 UTC (13.75 cm). The precipitation rate in region B is more evenly distributed over time. There is a slight decrease of the precipitation rate at the first simulation day from $0.08\,\mathrm{mm\,h^{-1}}$ to $0.06\,\mathrm{mm\,h^{-1}}$ and then an increase to a precipitation rate of $0.09\,\mathrm{mm\,h^{-1}}$ on March 24, 7 UTC. After reaching the maximum, the precipitation rate decreases until the end of the simulation where the precipitation rate is again $0.07\,\mathrm{mm\,h^{-1}}$.

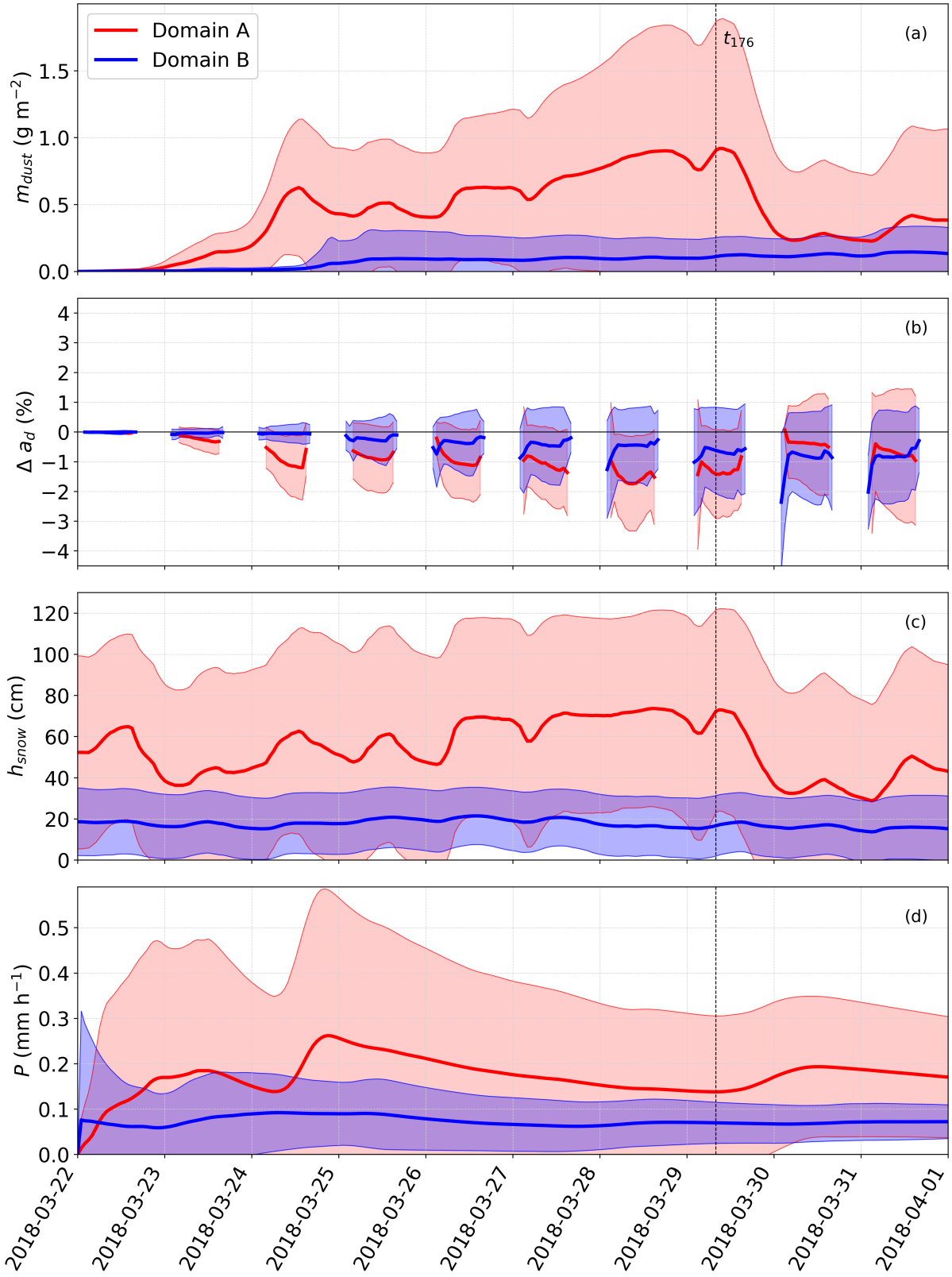

Figure 5.3: Hourly ensemble means (lines) and standard deviations (shading) of mineral dust loading in the top snow layer m_{dust} (a), the differences (SDS−REF) in diffuse surface albedo a_d (b), snow height h_{snow} (c), and precipitation rate P (d) on all snow covered cells across region A (red) and B (blue).

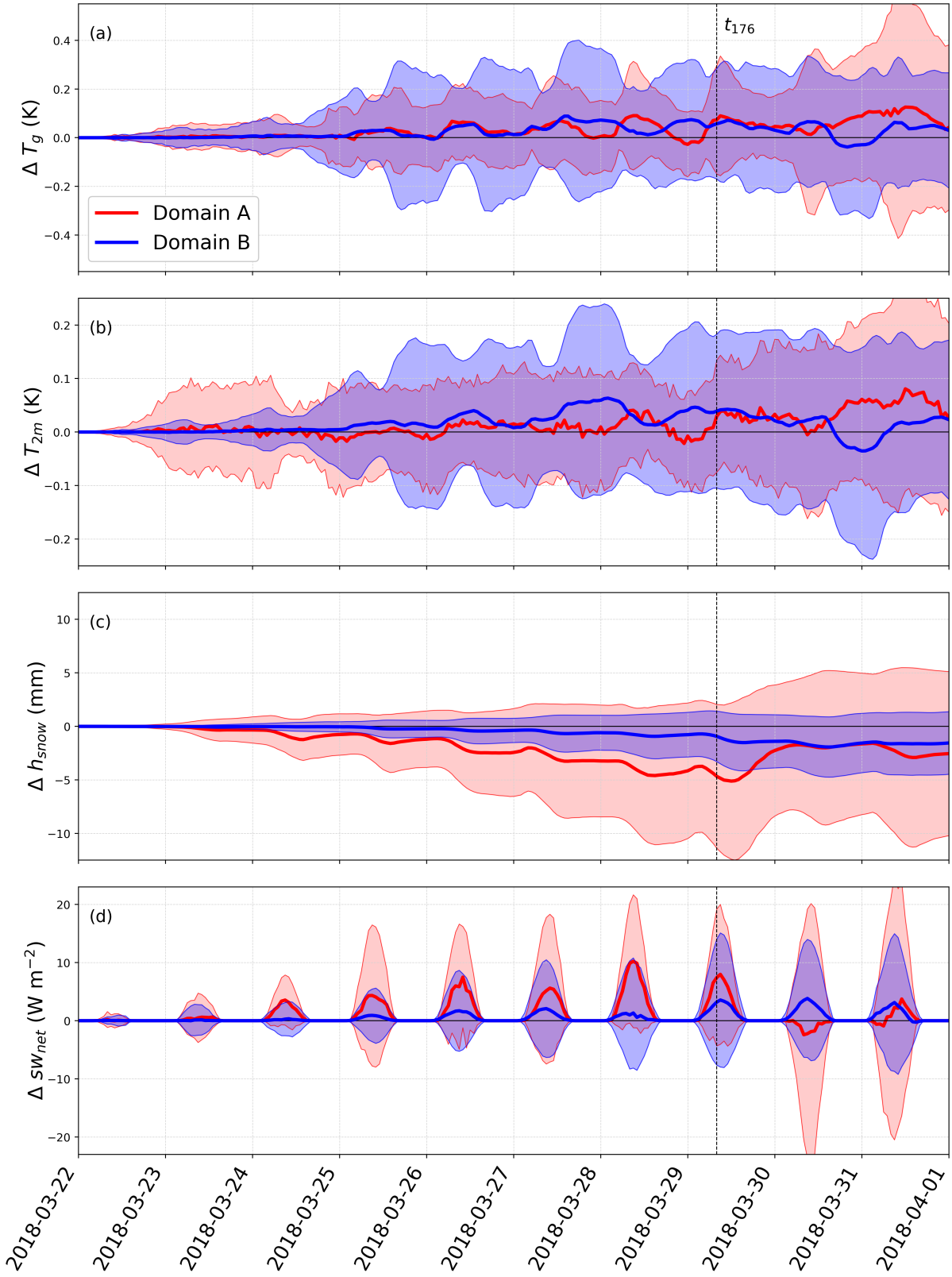

Figure 5.4: Hourly ensemble means (lines) and standard deviations (shading) of the differences (SDS−REF) in surface temperature T_g (a), 2m-temperature T_{2m} (b), snow height h_{snow} (c), and surface shortwave net radiation flux sw_{net} (d) on the snow covered cells across region A (red) and B (blue).

Fig. 5.4 shows the feedback to the changed snow albedo in the surface temperature T_g, 2m-temperature T_{2m}, snow height h_{snow}, and surface shortwave net radiation flux sw_{net} in region A (red) and region B (blue). The average of the ensemble differences between SDS and REF are shown as lines and the respective standard deviations are illustrated as shading in the respective color. Only cells containing snow cover are taken into account.

The feedback in surface temperature needs a lead time until it becomes visible in both regions. At the beginning of the fourth simulation day, the surface temperature starts to increase in SDS compared to REF. A daily cycle is visible where the largest difference coincides with the daily maximum of the difference in surface shortwave net radiation flux between SDS and REF. The largest increase in surface temperature in region A is observed on March 31, 12 UTC (0.13 K) while the largest effect in region B occurs on March 27, 14 UTC (0.09 K). There are occurrences of a decrease in surface temperature in both regions during night time. Region A reaches the strongest reduction in surface temperature in SDS compared to REF in the night from March 28 to March 29 (-0.03 K) and region B in the night from March 30 to March 31 (-0.04 K). The diurnal variation is less pronounced after March 28, suggesting that other effects outweigh the albedo effect on the surface temperature.

The 2m-temperature shows a similar behavior as the surface temperature in region B, although the influence is significantly smaller. On average, the 2m-temperature is increased by 0.02 K in SDS and reaches a maximum of 0.03 K on March 28, 2 UTC. After a spin-up time of 3 days, a positive effect in 2m-temperature is also visible in region A during daytime reaching a maximum difference on March 31, 12 UTC with 0.08 K between SDS and REF. An exception is March 30, when the 2m-temperature in SDS drops below the 2m-temperature in REF around noon. The mean difference in 2m-temperature in region A is 0.01 K for the whole simulation.

The snow height decreases in SDS compared to REF after a lead time of one day in region A and roughly three days in region B. During the day, the difference grows, while at night a slight counterbalancing takes place. The largest difference between SDS and REF occurs on March 29, 12 UTC with a lowered snow height in SDS of -0.51 cm. After that, the difference is balanced by the new snow in region A and the reduction does not drop lower than -0.3 cm in SDS.

The shortwave net radiation flux is affected already from the second day. In SDS, mainly a positive feedback is evident with a mean radiative forcing during the sunlight hours of 2.38 $\mathrm{W\,m^{-2}}$ averaged over region A. The largest difference between SDS and REF is on March 28, 9 UTC where the magnitude of the ensemble mean difference is 10.24 $\mathrm{W\,m^{-2}}$ in region A. March 30 is exceptional because the shortwave net radiation flux in SDS is -2.41 $\mathrm{W\,m^{-2}}$ lower than in REF. This is probably because of changes in atmospheric conditions instead of changed surface properties, because the albedo in SDS is still lower than REF. Region B shows a similar behavior, but has a less pronounced effect. The mean radiative forcing for the sunlight hours is 0.81 $\mathrm{W\,m^{-2}}$ and has a maximum on March 30, 9 UTC with a mean increase of 3.82 $\mathrm{W\,m^{-2}}$ in SDS.

Considering the whole simulation domain, the decrease in snow albedo is constantly present and increases throughout the simulation. The feedback to the changes in snow albedo is also evident but is averaged over the whole domain relatively small and therefore the temporal evolution of the variables in region A and B are shown only. A respective figure for the whole domain can be found in the

appendix (Fig. A.1), covering the evolution of the mean difference in diffuse albedo, snow height, surface temperature, 2m-temperature, surface shortwave net radiation flux and the overall cloud cover between SDS and REF during the whole simulation. There is no remarkable difference in the degree of cloud cover between SDS and REF. Here, it also becomes apparent that the formation of feedback in the different variables requires a certain leading time. An important note is that the two scenarios averaged over the entire simulation domain regarding the surface albedo and the snow height diverge more and more with time, so that the reduction in surface albedo and the snow height occurs on the last day.

The temporal evolution of the mineral dust deposition and the surface variables were presented in the above. These results will now be discussed in the remainder of this section. It was shown that the effect of mineral dust in the snow cover continuously increases in terms of the albedo difference, the snow depth and the shortwave net radiation flux between SDS and REF. However, the presence of these effects also depend on the large-scale weather conditions. For example, the radiative effect at the surface can also be negative despite the reduced surface albedo. This happens when the cloud cover or the precipitation differs in the two scenarios. This appears to be the case on the ninth simulation day in region A. The difference in the shortwave net radiation flux is an estimate for the comparability of the atmospheric conditions between SDS and REF. A strong variability in the difference in shortwave net radiation flux is apparent when the cloud cover differs. After March 29, the shortwave net radiation flux shows that both scenarios diverge in the atmospheric conditions and therefore the days after March 29 are not considered for the more detailed spatial analysis.

It is apparent that the formation of feedback in the different variables requires a certain leading time. The largest differences between SDS and REF appear in the results on the last day, indicating that no threshold has been reached within the 10 days of simulation and the effect is expected to grow further. A follow-up study that considers a longer period of time, for example over an entire year, would provide more information on whether the effect continues to increase or stagnates after a certain time. Dumont et al. (2020) ran the model three years prior to their main simulation due to settlement of the ground temperature and then ran the simulation for a full year where the dust event occurs at the end. There was no such a spin-up simulation in this study and the snow was completely aerosol free at the beginning of the simulation. This could lead to an underestimation of the dust loading in snow, since background concentration that accumulated before the big dust event could not be captured. Furthermore, Dumont et al. (2020) reported that the dust deposition was covered by clean snow after a few days which is also observed in this study. However, Dumont et al. (2020) stated that with snow melting after a few weeks, the aerosols were again exposed and concentrated at the snow surface. As a result, the deposited mineral dust again had an impact on the snow melt. This shows that the effects of an extreme dust deposition event are not only of short duration but can have far-reaching consequences for the snow cover.

The difference between SDS and REF of surface temperature and 2m-temperature indicate that the relationship to mineral dust deposition is somewhat more complicated compared to the coupling of surface albedo or radiation flux to the dust. The growth in the difference by the eighth day indicates that the weather is consistent over large areas and regional effects can develop. The feedback to the reduced albedo is masked thereafter by other effects, possibly large scale weather changes from the ninth day onward. In other words, from day to day, the strength of the repercussions caused by the mineral

dust on the snow varies, whereby the average amount of dust on the snow naturally plays a role but is not the determining factor. Atmospheric conditions play a huge role in whether the disturbance can develop in the surface and propagate to the lower atmosphere.
The amounts of cloud cover between the two scenarios are almost identical. This means that the disturbance of the surface properties by the mineral dust does not have much influence on the cloud cover amount. In comparison to the investigations of Rahimi et al. (2020), the dust is not completely excluded in the reference simulation, but rather the impact on the snow albedo is simply switched off. However, there could be a redistribution of the cloud pattern which is not visible in the averaged results. Therefore, in the next sections, the spatial distribution will be discussed. March 29, 8 UTC is presented for the whole domain and the two sub-regions, as this date ensures a start-up time for the perturbation of the snow albedo and the evolution of the feedback. Furthermore, at this specific time, the shortwave net radiation flux shows the daily maximum of the response and is close to the highest dust mass loading in region A.

5.3 Spatial Distribution and Elevation Dependence

The benefits of an ensemble simulation can be demonstrated by comparing the averaged results with those of individual simulations. Fig. 5.5 shows the difference in diffuse albedo between a single SDS and a single REF at t_{176} (March 29, 2018, 8 UTC). The mean diffuse snow albedo reduction in SDS is $-0.43\,\%$, $-1.77\,\%$ in region A and $-1.05\,\%$ in region B. Thus, there is a clear mean reduction in snow albedo due to mineral dust deposition in all areas at this point of time. However, the standard deviation is very large. There is a lot of noise, which is characterized by constant sign changes of the difference even at very small distances. In section 4, it was already pointed out that the spectral albedo is strongly dependent on the atmospheric conditions, especially the clouds and gas composition of the atmosphere. The variability is clearly visible on the Russian territory since the difference patterns follow the movements of clouds and only appear during sunlit hours. The small scale variability can account for several percent of the difference in snow albedo. The standard deviations of the three regions are 3.74 %, 4.55 % in region A and 6.01 % in region B.
Fig. 5.6 shows the respective mean difference in snow albedo at t_{176} of all ensemble members between SDS and REF. The local signals are far less strong, but the noise reduction is clearly evident. Small-scale variability is greatly reduced, and the sign of the change is homogeneous over large areas. Especially along the snow line, a clear reduction in diffuse surface albedo due to dust deposition in snow is visible (blue arrow) with the exception of an area in Russia northeast of the Black Sea (red arrow). The area of the Caucasus Mountains shows a clear negative signal in the diffuse surface albedo as well. Furthermore, areas in the northwestern corner of the Black Sea as well as some areas in Belarus are characterized by a reduced snow albedo in SDS. The ensemble mean reduction in snow albedo in SDS is $-0.38\,\%$ over the whole area, $-1.42\,\%$ in region A and $-0.62\,\%$ in region B. The corresponding standard deviations are 1.23 %, 1.50 % in region A and 1.45 % in region B.
Fig. 5.7 shows the mean dust loading in the top snow layer of all SDS ensemble members that induce the snow albedo reduction at t_{176}. Dust deposition is mainly observed where mountain ranges act as obstacles to the air flows from the source areas. This is clearly visible on the south-facing slopes of the

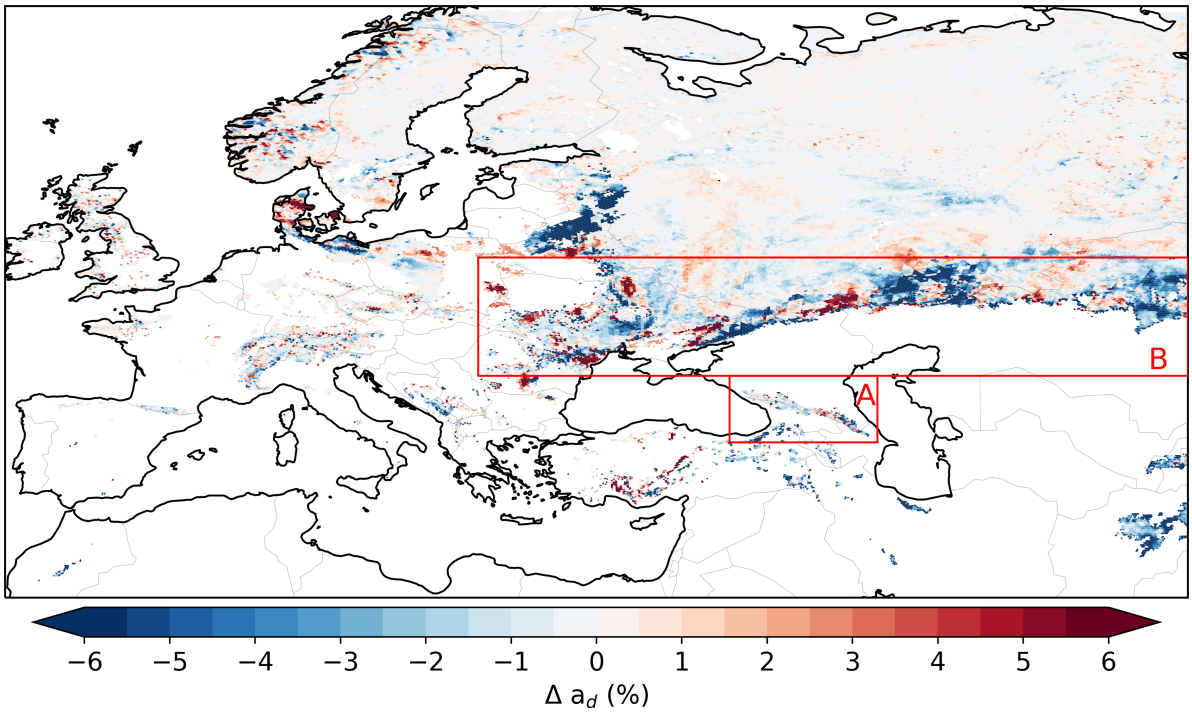

Figure 5.5: Spatial distribution of the difference in diffuse surface albedo a_d between a single simulation pair (SDS and REF) on March 29, 2018, 8 UTC.

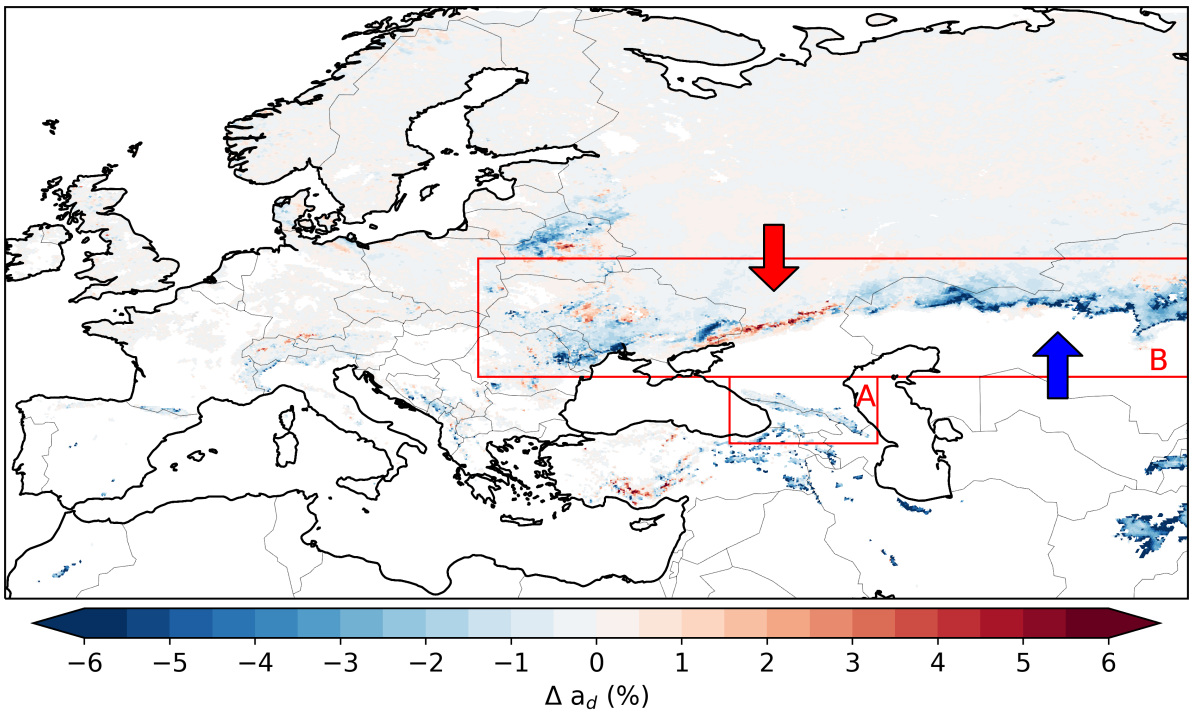

Figure 5.6: Spatial distribution of the Ensemble mean difference between SDS and REF of the diffuse surface albedo a_d on March 29, 2018, 8 UTC.

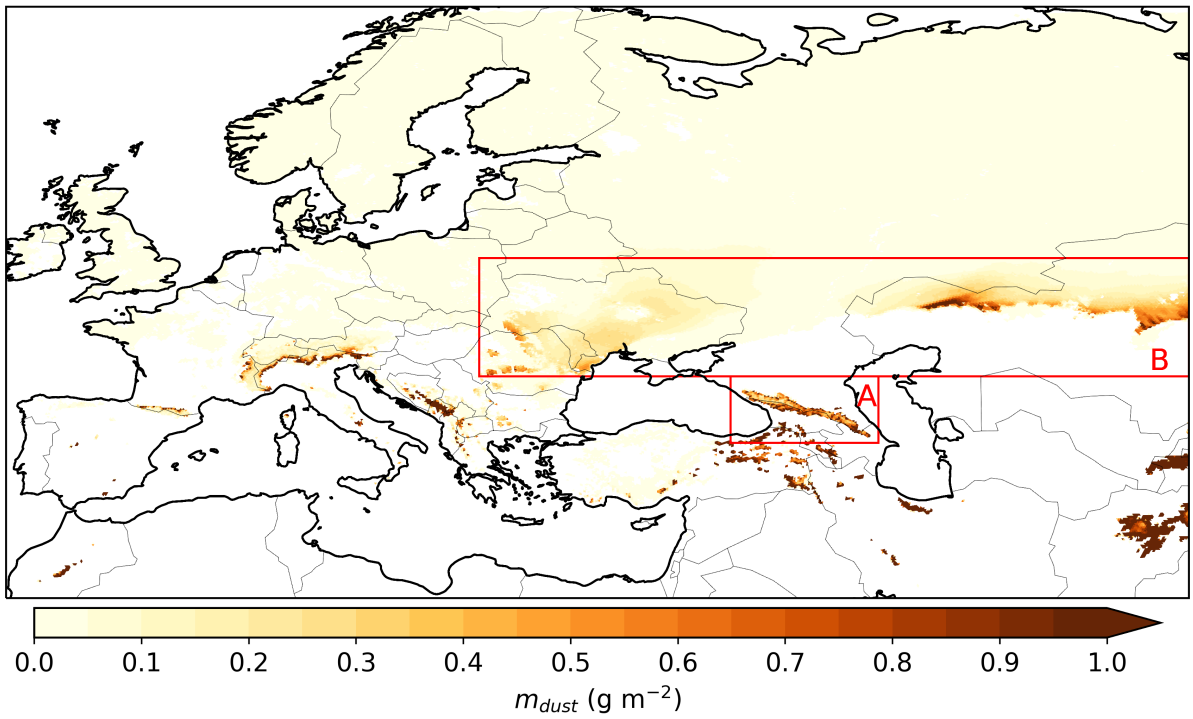

Figure 5.7: Ensemble mean (SDS simulations) of the dust loading m_{dust} in the top snow layer on March 29, 2018, 8 UTC.

Pyrenees, the Alps, the Dinaric Mountains, and the Carpathians. In addition, the Caucasus Mountains and parts of the Pontic Mountains adjacent to them in the south have high levels of mineral dust in snow. The snow line in Kazakhstan east of the Caspian Sea also shows higher values at the Mugodzhar Hills and the Kazakh Uplands. In the southeast of this section of the map, parts of the Hindu Kush and the Pamirs are identifiable, which also show a high influence of mineral dust, but do not constitute the focus of this study. In the area northeast of the Black Sea, where an increase in albedo is observed in SDS, dust levels are very low. The mean dust loading of the whole map at t_{176} is $0.10\,\mathrm{g\,m^{-2}}$ with a local maximum of $32.94\,\mathrm{g\,m^{-2}}$ (Baba Mountain range, western extension of the Hindu Kush). Region A holds a mean dust loading of $0.90\,\mathrm{g\,m^{-2}}$ and a local maximum of $11.67\,\mathrm{g\,m^{-2}}$ at this point. Region B shows a mean dust loading of $0.11\,\mathrm{g\,m^{-2}}$ and a local maximum of $1.66\,\mathrm{g\,m^{-2}}$.

The ensemble mean difference at t_{176} of the total precipitation since model start on snow covered surfaces P_{tot} and of the snow height is shown in Fig. 5.8. The pattern of the differences in snow height is very similar to the pattern of difference in total precipitation. This can be seen especially on the Russian territory in Belarus and Ukraine, where alternately an increase as well as a decrease in snow height is apparent (black arrow). There is a tendency for a decrease in snow height near the Belarus-Russia border and an increase in the adjacent Russian territory. The difference in snow height in the Alps in Central Europe, does not show a clear signal and follows the rather chaotic patterns in precipitation. However, there are widespread areas where a modification in snow height can not be accounted for by the change in precipitation. They can be attributed to the disturbance in the optical properties of snow since they coincide with the decrease in surface albedo in SDS. Mainly a decrease in snow depth near the snow line is observed (blue arrow) with the exception of the area in Russia northeast of the Black Sea (red arrow).

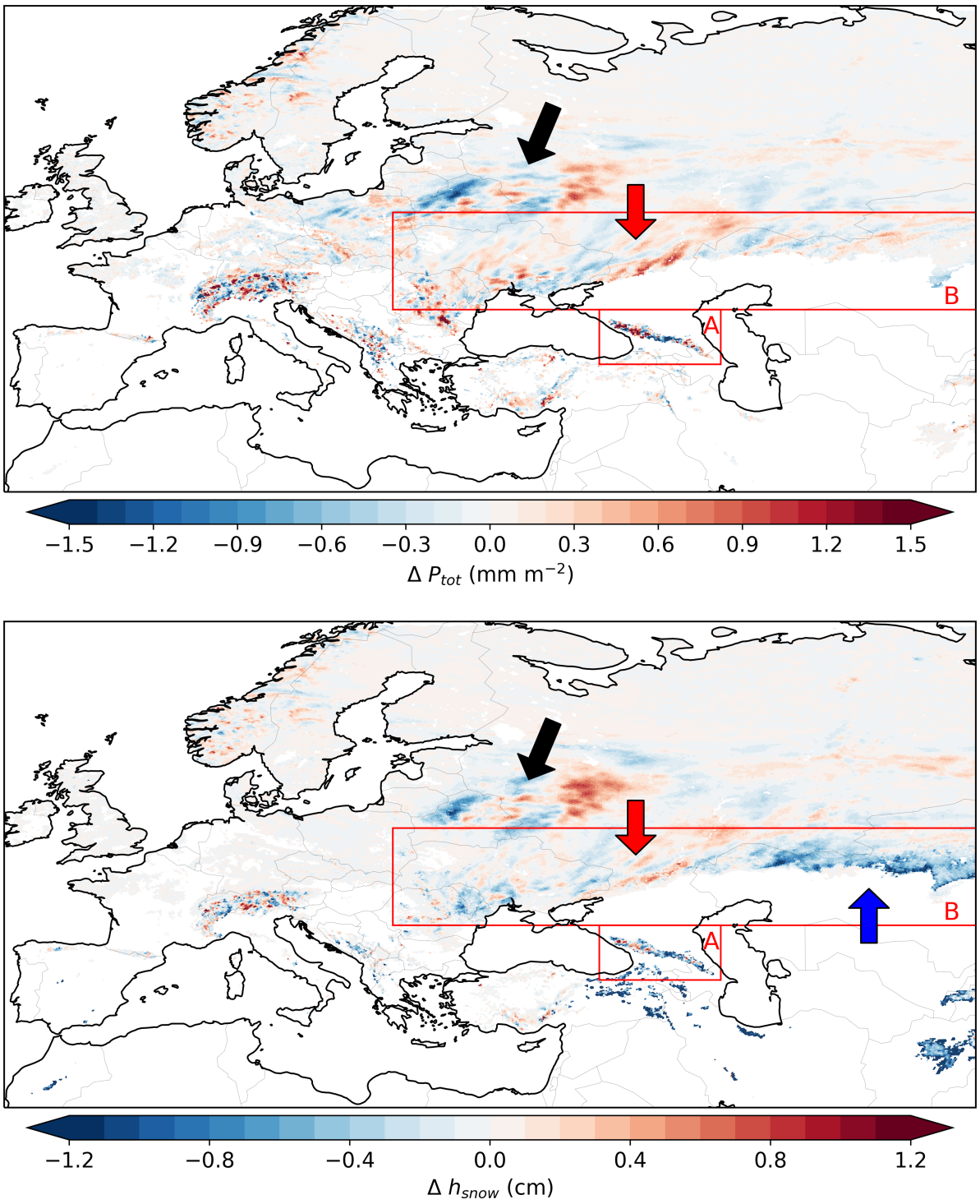

Figure 5.8: Ensemble mean difference between SDS and REF of snow height h_{snow} (top) and the total precipitation since simulation start P_{tot} (bottom) on March 29, 2018, 8 UTC.

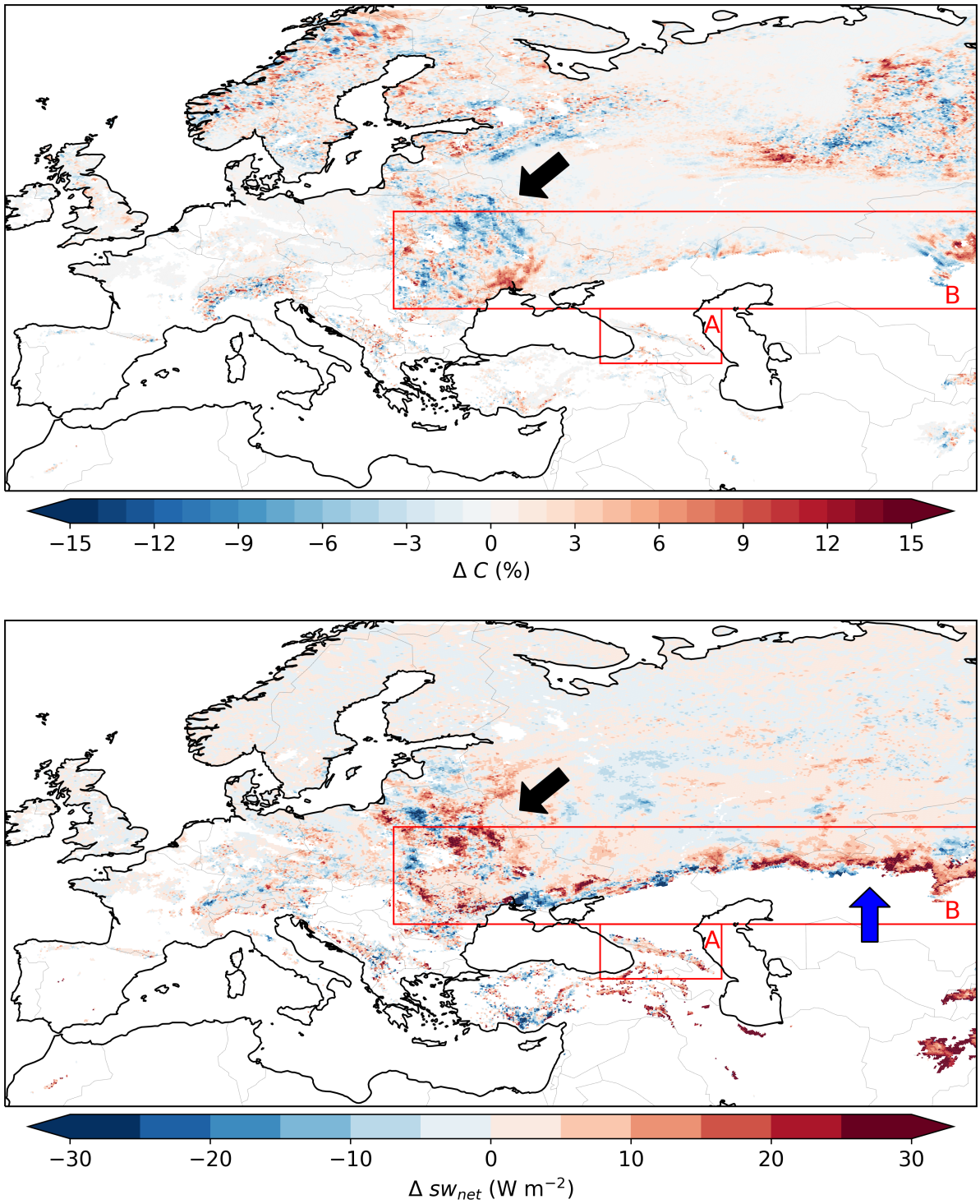

Figure 5.9: Ensemble mean difference between SDS and REF of cloud cover C in % (top) and the surface shortwave net radiation flux sw_{net} in W m^{-2} (bottom) on March 29, 2018, 8 UTC.

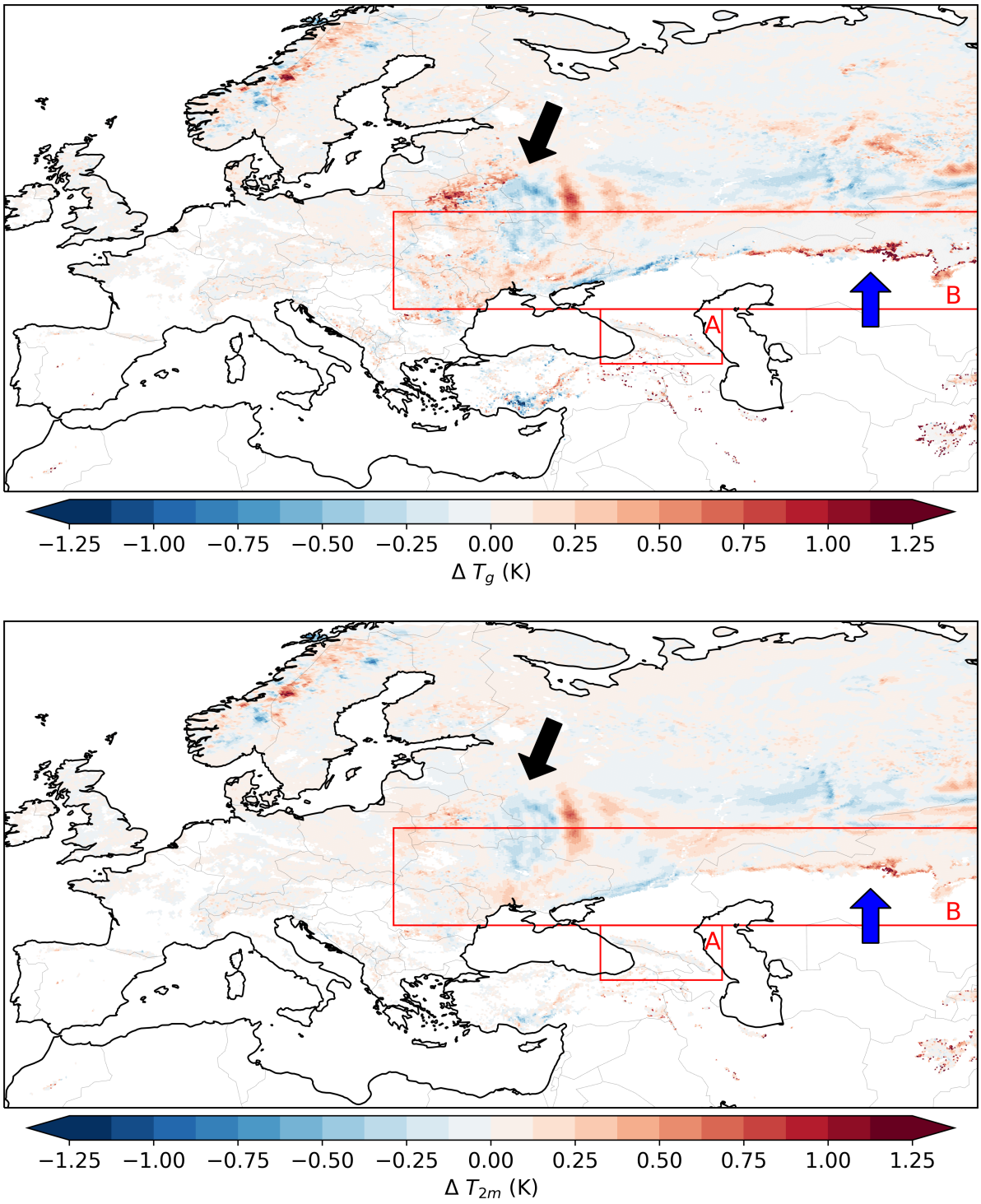

Figure 5.10: Ensemble mean difference between SDS and REF of surface temperature T_g (top) and 2m-temperature T_{2m} (bottom) on March 29, 2018, 8 UTC.

Also, a reduction in snow depth is mainly observed in the Caucasus Mountains and the mountains further south and east. The mean difference in snow height over the whole area at t_{176} is -0.05 cm in SDS with a local minimum of -10.15 cm (French Alps). The difference in total precipitation between SDS and REF since model start shows a patchy distribution. Both increase and decrease occurs side by side, implying a shift of precipitation (black arrow). On average, there is no tendency towards an increase or decrease in precipitation. However, there is mainly an increase in precipitation in SDS northeast of the Black Sea (red arrow), where snow height and diffuse surface albedo are increased.

The shortwave net radiation flux difference at t_{176} is a momentary snapshot, which can be connected to two different dependencies similarly to the case of the difference in snow height. Fig. 5.9 shows the difference in cloud cover and the difference in shortwave net radiation flux at t_{176}. The difference in cloud cover shows no particular tendency with a mean increase of only 0.04 % and a median of 0.00 %. Where larger differences appear, both positive and negative values are shown, indicating a simple shift of the clouds. This happens in the Scandinavian area, in Russia, East Kazakhstan, and in the Eastern European countries north of the Black Sea (black arrow). In these Eastern European countries, the pattern of the shortwave net radiation flux is similar to the inverse of the cloud cover (black arrow). Surprisingly the cloud cover changes do not affect the shortwave net radiation flux significantly at more northern parts. This is probably due to the fact that shortwave radiation generally decreases towards higher latitudes. Again, the areas close to the snow line are characterized by a strong increase in radiation flux (except northeast of the Black Sea), which matches the changes in albedo (blue arrow). There is an overall increase at t_{176} of 1.49 $\mathrm{W\,m^{-2}}$ in the whole domain, 7.41 $\mathrm{W\,m^{-2}}$ in region A and 3.20 $\mathrm{W\,m^{-2}}$ in region B in comparison of SDS to REF.

Fig. 5.10 shows the ensemble mean difference surface temperature and 2m-temperature at t_{176} between SDS and REF. The two properties show very similar patterns. The signal in surface temperature is often twice as strong or even greater than the signal in 2m-temperature. Both surface temperature and 2m-temperature are increased in SDS along the snow line in Kazakhstan. Northeast of the Black Sea, both variables are in turn lower in SDS and therefore match the inverse pattern of the decrease in snow albedo in these locations (blue arrows). But there are differences in those temperatures, especially on the Russian territory, that cannot be attributed to the change in albedo and do not exactly match the patterns of the other variables that have been shown (black arrows). A temporal analysis of the spatial distribution reveals that these patterns move. In this case from west towards east. During the simulation, such patterns are headed towards various directions and are most pronounced during the day. There is no explicit tendency to a decrease or increase here. It is assumed that these are influences of large-scale weather dynamics. Nevertheless, on average, a slightly higher surface temperature and 2m-temperature is apparent in SDS. The mean difference in surface temperature over the whole area is 0.03 K in SDS compared to REF and a mean difference in 2m-temperature of 0.01 K. The signal is strengthened when averaging over the smaller regions. The mean increase in SDS of surface temperature is 0.07 K in region A and 0.06 K in region B. The mean increase in SDS of 2m-temperature is less pronounced and reaches only 0.03 K in region A and 0.04 K in region B.

Fig. 5.11 shows the frequency distribution of the amount of dust in the top snow layer in SDS, as well as the differences between SDS and REF of the variables diffuse surface albedo, snow depth, and shortwave

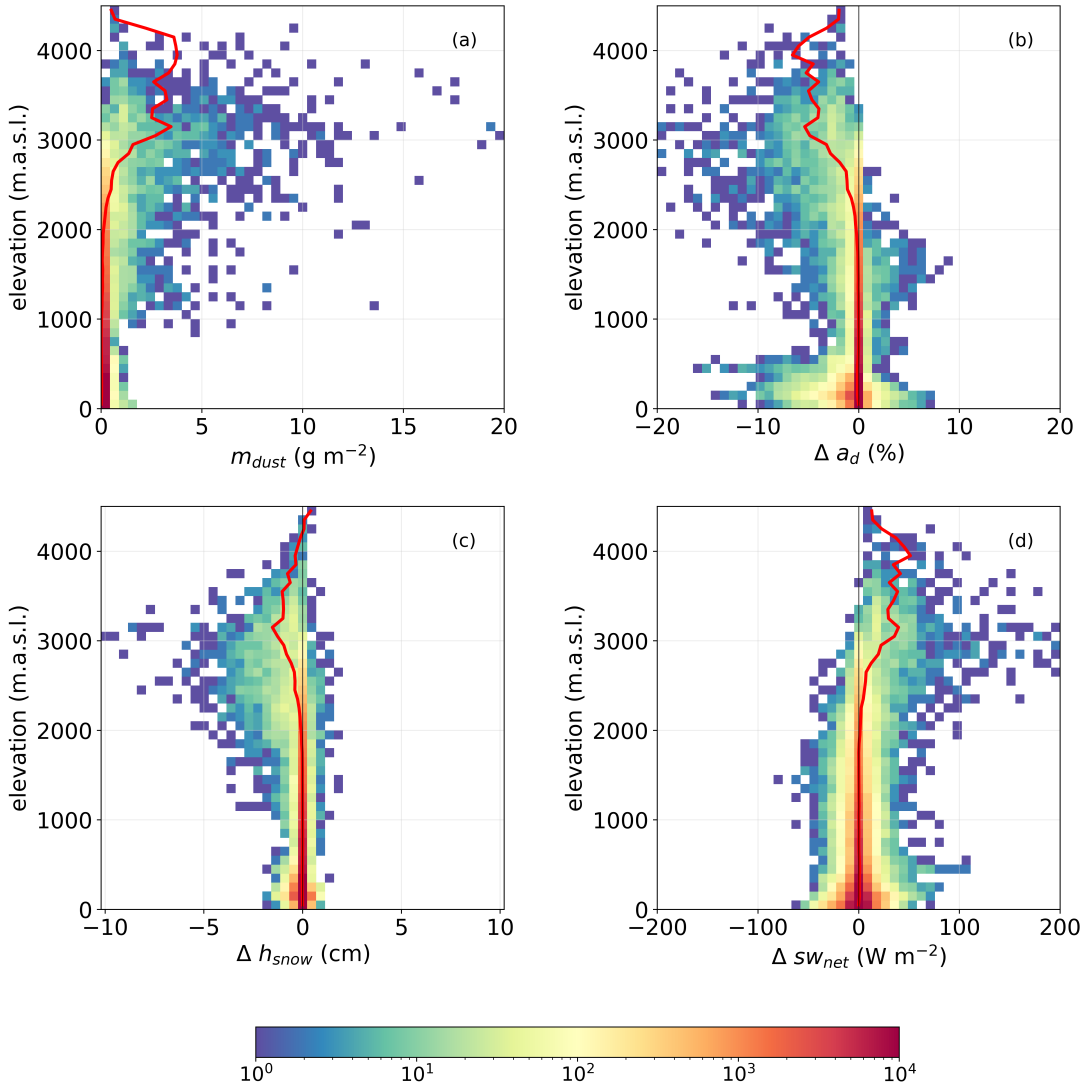

Figure 5.11: Density plots as height profiles of the ensemble mean (SDS) of dust loading in the top snow layer m_{dust} (a), the ensemble mean differences of REF and SDS in diffuse surface albedo a_d (b), snow height h_{snow} (c), and surface shortwave net radiation flux sw_{net} (d) on March 29, 2018, 8 UTC.

net radiation flux as a function of elevation. Fig. 5.12 shows the difference between SDS and REF of surface temperature and 2m-temperature as a function of elevation. The data are grouped along the y-axis in 100 m sections and the respective mean value of the sections are marked as a red line. Above a height of 3900 m, the amount of data in the LAM domain thins out and falls below 20 cells per 100 m section. Hence, above this height the data are possibly no longer representative.

The averaged amount of dust increases at higher elevations and exceeds 0.1 g m^{-2} beyond 2000 m and 1 g m^{-2} beyond 2800 m. Above this altitude, the mean amount of dust in the top snow layer continues to increase with elevation and reaches a maximum at 3100–3200 m with a dust loading of 3.47 g m^{-2}. Thereafter, the concentration of mineral dust in snow decreases again, but reaches another maximum (3.77 g m^{-2}) at 3900 m.

The influence of the deposited dust on the diffuse albedo also shows a strong height dependence corresponding to the deposition amount of dust in snow. The greatest reduction in surface albedo is

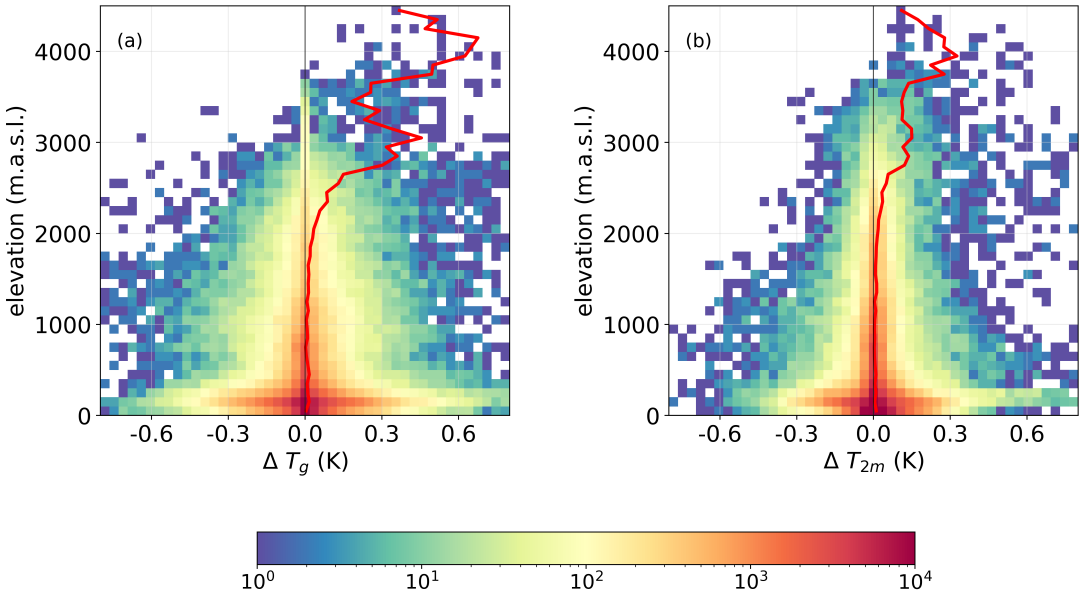

Figure 5.12: Density plots as height profiles of the ensemble mean differences of REF and SDS in surface temperature T_g (a) and 2m-temperature T_{2m} (b) on March 29, 2018, 8 UTC.

in accordance with the amount of mineral dust at the altitude between 3900–4000 m, where the amount of data is sparse. Here, the mean reduction in surface albedo is $-6.58\,\%$. A second local maximum of the difference in surface albedo is also located between 3100–3200 m with a mean reduction in SDS of $-5.36\,\%$. Up to the elevation of 3200 m, the amount of dust increases with altitude and the difference in diffuse surface albedo between SDS and REF increases as well. Above 2400 m, the mean reduction in diffuse surface albedo is always stronger than $-1\,\%$ in SDS compared to REF and above 2800 m even more than $-2.5\,\%$.

The mean difference in shortwave net radiation flux reflects the mean of the difference in surface albedo. The largest difference between SDS and REF is reached between 3900–4000 m with a maximum increase in SDS of $51.33\,\mathrm{W\,m^{-2}}$. From an altitude of 2400 m, the mean surface shortwave net radiation flux in SDS is $5.0\,\mathrm{W\,m^{-2}}$ larger than REF and from 2700 m the net flux is always larger than $10.00\,\mathrm{W\,m^{-2}}$. The first local maximum is reached between 3100–3200 m where the radiative forcing is larger than $39.53\,\mathrm{W\,m^{-2}}$.

A slightly different pattern is evident in the snow height and surface temperature as well as the 2m-temperature. The mean snow depth has the largest difference between 3100–3200 m with a mean difference of -1.53 cm in SDS compared to REF. Unlike the surface albedo and dust concentration, the snow heights in SDS and REF do not diverge above this elevation, but rather converge again. Between 2700–3800 m the reduction in snow height compared to REF is maintained at least at -0.5 cm. Therefore, this range of altitude can be characterized as a more sensitive zone concerning the impact of mineral dust on the snow height.

The difference in surface temperature between SDS and REF shows an interesting feature. Alike the other variables, the impact of mineral dust is small at low elevation due to the lack of dust in snow. However, a small increase in surface temperature is noticeable at lower altitudes. The increase is 0.02 K at an altitude between 400–500 m in SDS. After that, the deviation between the two scenarios diminishes

before the difference increases again above an altitude of 1700 m. From this point, the difference in surface temperature strongly increases with elevation. A local maximum of 0.45 K of the difference between SDS and REF is reached on an elevation of 3000 m. Beyond this point, the difference in surface temperature fluctuates strongly and reaches the absolute maximum at an altitude between 4100–4200 m. Here, the increase in surface temperature in SDS is 0.68 K. The 2m-temperature follows the same profile as the surface temperature to some degree, with the maxima of the difference between SDS and REF being smaller. At the height of 3000–3100 m the first maximum is 0.15 K and between 3900–4000 m the absolute maximum of 0.33 K is reached.

5.3.1 Region A: The Caucasus Mountains

Region A includes Georgia and the Caucasus Mountains, where the dust event was reported in the media at this time. In order to investigate the small-scale impact, region A is studied in detail during the extreme event. Since the terrain in this area is of great importance, and in the following the elevation dependency will be presented, the topography is shown in Fig. 5.13.

The spatial patterns of the dust mass in the uppermost snow layer and the mean differences between SDS and REF of the variables surface albedo, snow depth, shortwave net radiation flux, surface temperature, and 2m-temperature at t_{176} are illustrated in Fig. 5.14. The dust concentration in the top snow layer of region A is very high on the southwestern slopes of the mountains in North Georgia. In the Russian area of the same mountains, which includes the north facing slopes, the amount of dust is also slightly higher. But even higher amounts of dust are located in the mountains on the Turkish territory. There is the largest inclusion of dust with a total mass of 11.67 $\mathrm{g\,m^{-2}}$ in the top snow layer. The amount of dust is reflected in the changes in surface albedo. In region A, a reduction in surface albedo exists in almost every cell where snow is present. The largest difference is visible on the Turkish side with $-13.42\,\%$. At the eastern end of the Caucasus Mountains, there is a larger reduction in albedo, although the amount of dust is not very high compared to the rest of this region (black arrow). The same applies to a few cells of the slopes exposed to the northeast.

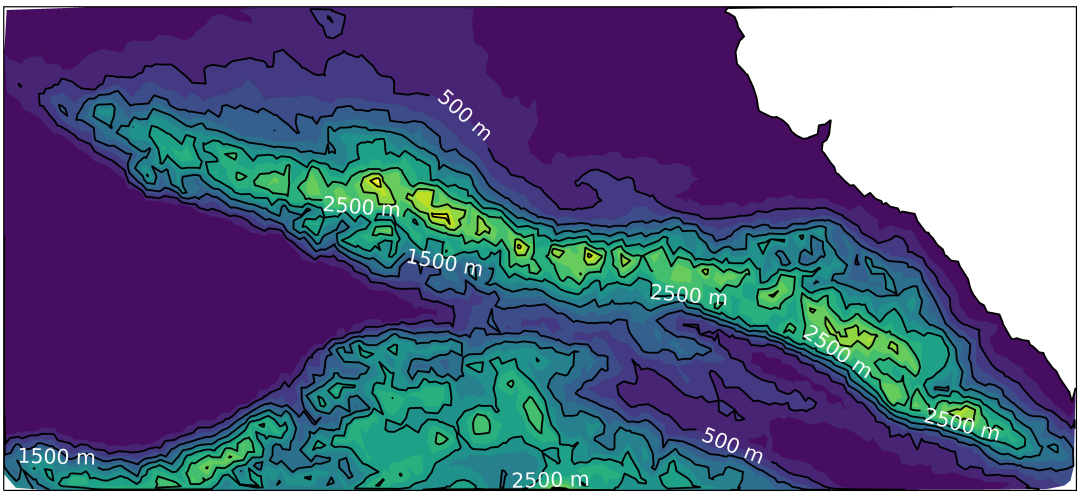

Figure 5.13: Topography of region A covering the Caucasus Mountains.

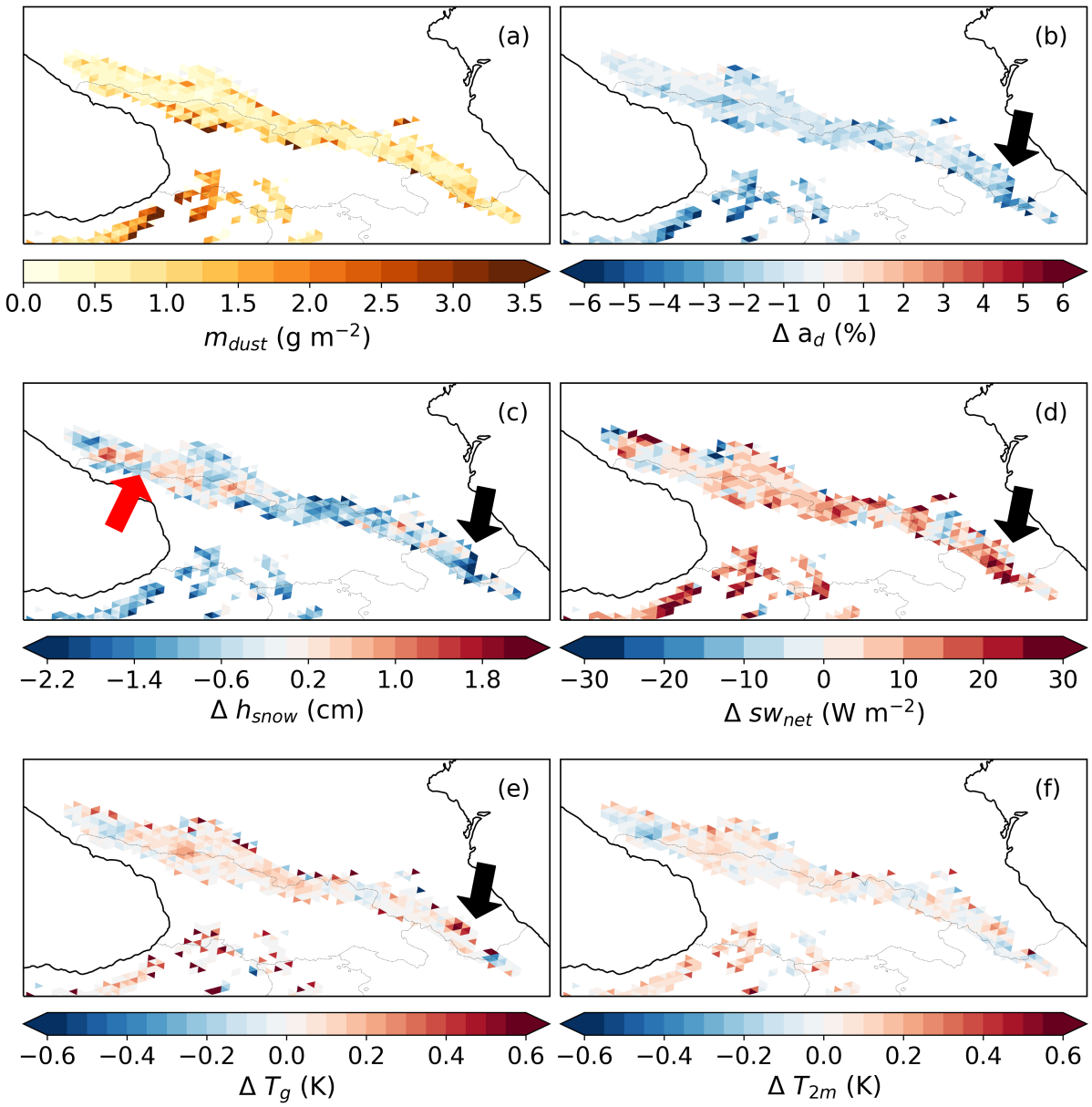

Figure 5.14: Ensemble mean (SDS simulations) of dust loading m_{dust} in the top snow layer (a) and the corresponding ensemble mean differences of diffuse surface albedo a_d (b), snow height h_{snow} (c), surface shortwave net radiation flux sw_{net} (d), surface temperature T_g (e), and 2m-temperature T_{2m} (f) on March 29, 2018, 8 UTC in region A.

Despite the general decrease in surface albedo in SDS, alongside the reduction in snow depth, there are also areas where snow cover increases. This mainly takes place in the center of the western part of the Caucasus Mountains in closer proximity to the Black Sea (red arrow) and at a few spots in the eastern part of the Caucasus Mountains. The edges of the mountain range do not show an increase in snow depth, nor do the mountains on the Turkish side. The strongest decrease is on the eastern edge of the Caucasus Mountains (-3.12 cm), where a strong albedo reduction is also evident, despite moderate dust intrusion (black arrow). The shortwave net radiation flux in most cells, especially on the Turkish side, represents the inverse of the surface albedo pattern. In the same region, the largest increase in radiative flux is found in SDS compared to REF with 92.45 $\mathrm{W\,m^{-2}}$. The pattern is more complicated in the Caucasus Mountains, where negative and positive signs alternate in a rather dense spatial area. It should be noted here that the radiation flux is a snapshot which strongly depends on the current cloud cover. A strong decrease in shortwave net radiation flux is observed especially at the western edge and eastern corner (black arrow) of the Caucasus Mountains.

At first impression, the change of the surface temperature seems to be relatively small if only the mean value is taken into account. However, Fig. 5.14 shows that local significant changes can occur. Surface temperature is increased in SDS especially on the northern side of the Caucasus Mountains and at the eastern edge, where a large decrease in snow depth is apparent (black arrow). Furthermore, higher values appear in the mountains at the southern edge of Georgia, which extends into Turkey. Here, the maximum difference between SDS and REF is 2.01 K. The 2m-temperature shows almost the same pattern as the surface temperature. However, the 2m-temperature differences show a significantly weaker signal. The largest difference between SDS and REF is located close to the largest difference in surface temperature, but reaches only 0.62 K.

Fig. 5.15 shows the frequency distribution of the amount of dust in the top snow layer in SDS, as well as the differences between SDS and REF of the variables diffuse surface albedo, snow depth, and shortwave net radiation flux as a function of elevation in region A. Accordingly, Fig. 5.16 shows the difference between SDS and REF in surface temperature and 2m-temperature. For an estimate of the ambient snow conditions in region A, the mean snow height and snow cover fraction of SDS are illustrated as well. The data are grouped along the y-axis in 100 m sections, and the respective mean of the sections is marked as a red line. The number of cells below 1300 m and above 3200 m is less than 10 per 100 m section. Therefore, the results should be considered with caution, and it should be noted that they may not be representative.

The largest concentration of mineral dust in region A is at the altitude of about 1800–1900 m with a maximum mean dust loading of 1.47 $\mathrm{g\,m^{-2}}$ (red arrow). There is another slightly smaller maximum at the altitude between 2100–2200 m with an average dust loading of 1.28 $\mathrm{g\,m^{-2}}$. Further above, the mean mineral dust loading in snow decreases. The impact on surface albedo is greatest on an elevation between 2000–2100 m (red arrow). Although the mineral dust loading only amounts 1.05 $\mathrm{g\,m^{-2}}$, the decrease in surface albedo reaches a value of $-2.06\,\%$ in SDS in comparison to REF. Above this altitude, the difference between the scenarios becomes slightly smaller, but persists up to an altitude of 3100 m. From an altitude of 1600 m the mean reduction in surface albedo is always less than $-1\,\%$ up to an elevation of 3100 m. Between 1900–3100 m, the mean reduction in surface albdeo exceeds even $-1.5\,\%$. The

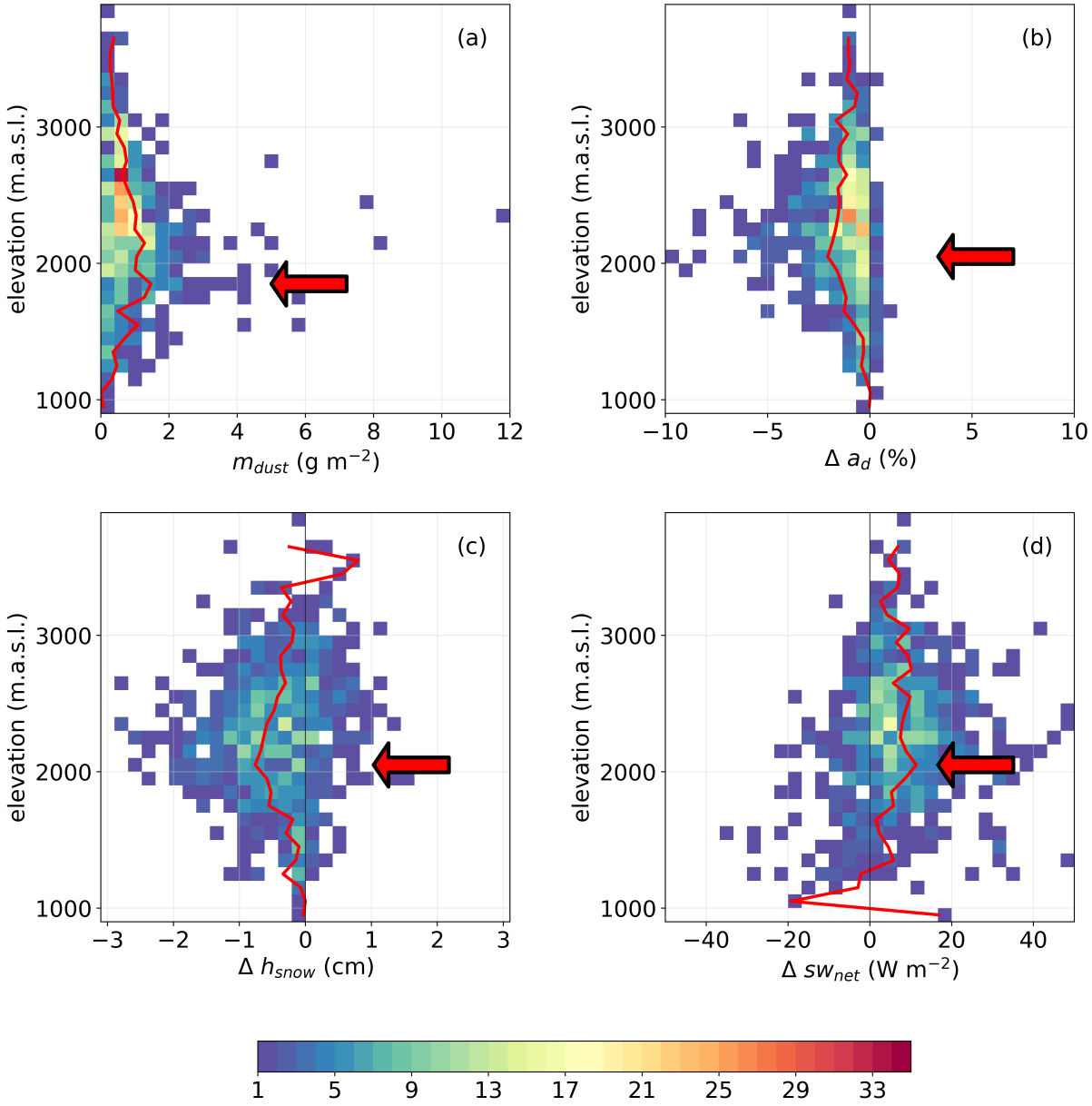

Figure 5.15: Density plots as height profiles of the ensemble mean (SDS simulations) of dust loading in the top snow layer m_{dust} (a), the ensemble mean differences between REF and SDS in diffuse surface albedo a_d (b), snow height h_{snow} (c), and surface shortwave net radiation flux sw_{net} (d) on March 29, 2018, 8 UTC in region A.

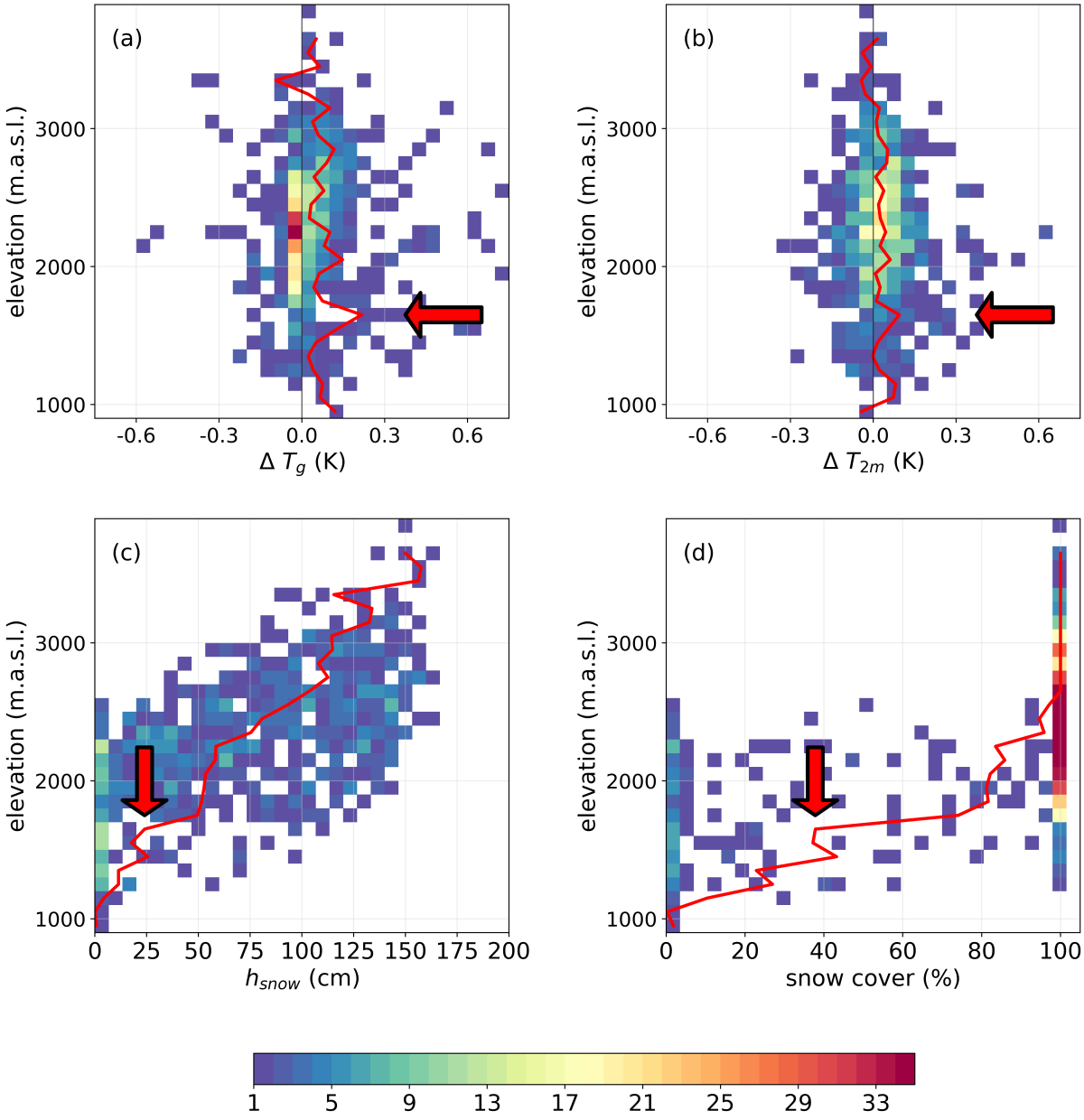

Figure 5.16: Density plots as height profiles of the ensemble mean differences between SDS and REF of surface temperature T_g (a) and 2m-temperature T_{2m} (b), as well as the SDS ensemble mean of snow height h_{snow} (c) and snow cover fraction (d) on March 29, 2018, 8 UTC in region A.

reduction in surface albedo relative to the dust loading is stronger at higher altitudes. For example, the mean dust loading at an altitude of 1500–1600 m is 1.08 $g\,m^{-2}$, and the difference in SDS to REF in surface albedo is $-0.75\,\%$. At an elevation of 2300–2400 m, the dust concentration is comparable (1.04 $g\,m^{-2}$), but the difference in surface albedo is about twice as large ($-1.55\,\%$).
The absorption of shortwave radiation increases with altitude as the albedo decreases. The largest difference between SDS and REF is between 2000–2100 m of altitude (red arrow), where a mean positive radiative forcing is as large as 11.34 $W\,m^{-2}$. Between 1700–3100 m, the shortwave net radiation flux is at least 5.00 $W\,m^{-2}$ increased in SDS. Interestingly, there is another small maximum at an altitude between 1300–1400 m where the mean net radiation flux in SDS is 5.80 $W\,m^{-2}$ higher compared to REF. This impact can also be found in the difference in snow height between SDS and REF. Between 1300–1400 m, snow depth in SDS is -0.34 cm less than REF. After that, the snow depths converge again before they diverge from 1700 m upwards. Between 1700–2400 m, the snow height in SDS always stays -0.5 cm lower than REF and reaches the largest difference with -0.76 cm between 2000–2100 m (red arrow). Above the 3200 m line, the snow depth varies greatly and reaches even an increase in snow height in SDS compared to REF (0.80 cm, 3500–3600 m).
The mean difference in surface temperature shows a strong discrepancy at a different elevation than the variables described above. The maximum of the difference is at a relatively low altitude between 1600–1700 m (0.22 K) (red arrow). At 2000–2100 m there is a smaller maximum of the difference with 0.15 K in SDS. Beyond that, these maxima are not exceeded. Also, the difference in 2m-temperature reaches the maximum of 0.09 K at the relatively low elevation of 1600 to 1700 m (red arrow). The impact of dust on the 2m-temperature is comparatively small at the other altitudes, and the difference between SDS and REF always remains below 0.07 K. It is worth noting that up to an altitude of 1700 m the snow height is less than 25 cm and the snow cover fraction is below 40 % (red arrows). After the 1700 m line, the fraction jumps over 75 % and further increases. A similar offset is apparent in the snow height. The average snow depth reaches more than 50 cm above 1700 m and further increases towards higher elevations.

5.3.2 Region B: The Extended Region With Retreating Snow Cover

Region B covers a larger area than region A and focuses on the impact of aerosols on the retreat of snow in parts of Eastern Europe, Russia, and Central Asia. The terrain, in contrast to the Caucasus region, is much flatter and mostly limited to an elevation of a few hundred meters above sea level, as can be seen in Fig. 5.17. In the preceding figure, that covered the entire simulation area, it was already recognizable that an interaction due to the dust deposition is nevertheless formed here. Lau et al. (2018) also detected a strong influence in this area at a rather coarse resolution on the climate scale. In the following, we take a closer look at different processes in this area.
Fig. 5.18 indicates that the amount of dust in snow does not entirely depend on the terrain. The Carpathians in the Ukraine and Romania stand out from the background concentration with slightly higher amounts. Similarly, there are higher accumulations in the west of Kazakhstan, where the Kazakh Uplands are located. However, the largest accumulation of dust in snow is further to the west of Kazakhstan, close to the Caspian Sea. There, the dust mass in the top layer of snow reaches an amount

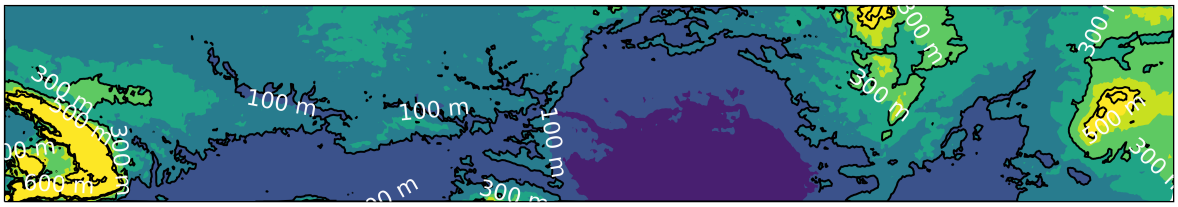

Figure 5.17: Topography of region B.

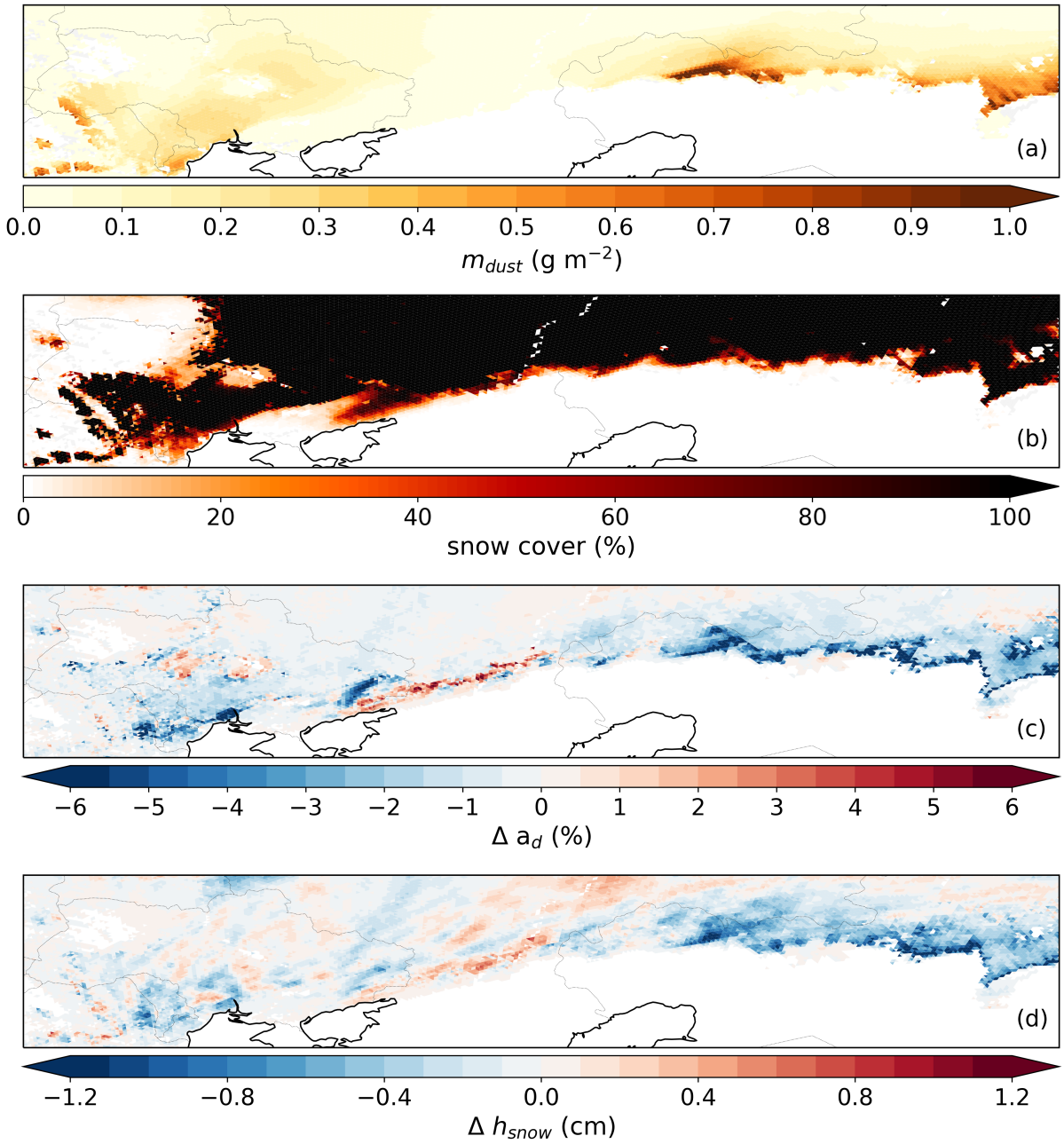

Figure 5.18: Ensemble mean (SDS simulations) of dust loading in the top snow layer m_{dust} (a) and the mean snow cover fraction (b), as well as the respective ensemble mean differences between SDS and REF of diffuse surface albedo a_d (c) and snow height h_{snow} (d) on March 29, 2018, 8 UTC in region B.

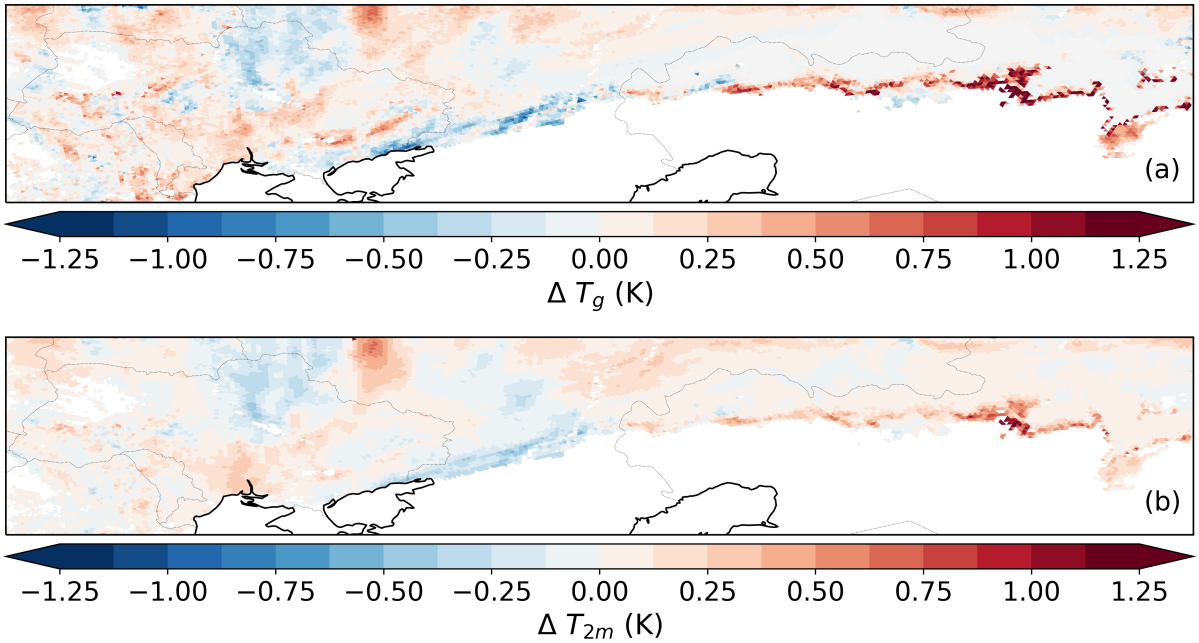

Figure 5.19: Ensemble mean differences of surface temperature T_g (a) and 2m-temperature T_{2m} (b) on March 29, 2018, 8 UTC in region B.

of 1.66 g m^{-2}. A reduction in albedo is particularly strong entirely along the snow line in Kazakhstan, not only where dust concentration is the most severe. The albedo in SDS is strongly reduced in Ukraine, Moldova, and Romania, especially near the Black Sea. The map of the snow cover fraction reveals that the snow cover is especially sparse here. As mentioned earlier, an increase in the surface albedo up to 6.68 % in SDS can be found in the Russian region northeast of the Black Sea. The behavior of the surface albedo is well mirrored in the distribution of the snow depth. The snow cover is increased up to 0.88 cm at those locations with higher surface albedo. This increase is associated with a higher amount of total precipitation (Fig. 5.8). There is only little dust in snow which could result from a lack of dust deposition or the covering up by the additional precipitation. In contrast to that, a strong reduction occurs almost everywhere at the snow line. This decrease in snow depth reaches locally to a maximum decrease of −1.73 cm in Kazakhstan. On average, the snow depth is −0.11 cm lower in SDS compared to REF for the whole region B.

Fig. 5.19 shows the effects of the albedo perturbation on surface temperature and 2m-temperature at t_{176} in region B. On the one hand, temperatures increase significantly in the eastern part, at the edges of the snow line, where the decrease in surface albedo occurs. However, this effect is almost exclusively at the edges of the snow cover and not further north, where the snow cover is more dense. On the other hand, temperatures are lower east of the Black Sea, where the albedo in SDS is higher. North of the snow line the patterns become quite complicated and show changes with both positive and negative tendencies. On average, the magnitude of the difference in surface temperature is greater than the 2m-temperature. I region B, the maximum change of surface temperature and 2m-temperature is 2.72 K and 1.29 K, respectively and both maxima are located in Kazakhstan.

5.3.3 Discussion

The impact of mineral dust deposition on snow albedo and its feedback is overlaid by model internal variability which was already mentioned by Rahimi et al. (2020). For example, natural changes in the patterns of precipitation that redistribute the snow fall (clean and dust contaminated), modify the snow height in several regions. Considering all regions, the mean decrease in snow height caused by the mineral dust contamination is always less than half a centimeter after 176 hours of simulation. In contrast, a shifted snow fall event can cause a change in snow height of several centimeters. In respect of the impact of surface shortwave net radiation flux, the position of clouds is crucial and varies quite easily with little changes in the atmosphere. Even the albedo itself varies throughout the day with the position of the sun and the cloud cover as shown in section 4. Therefore, the investigation of a single SDS simulation and a single REF simulation is difficult to interpret (Fig. 5.5). The major interfering factor in studying the change in snow depth due to aerosol is the variation in the patterns of precipitation. In addition, the change in cloud patterns has proven to be the largest disrupting element when examining the shortwave net radiation flux. Regarding surface and 2m-temperature, large scale weather systems interfere with the responses to the snow-darkening. The result of the ensemble mean (Fig. 5.6) shows a very homogeneous pattern, and the noise is significantly reduced. Such an ensemble set up is therefore recommended when investigating the impact of mineral dust on the snow albedo. Certainly, the signal in the variables are a lot less pronounced because of the averaging over all ensemble members. By having more ensemble members, the results get more robust but also diminish the intensity of the feedback.

At Roza Pik on March 27, 2018, Dumont et al. (2020) found a dust concentration in snow of 606 and 786 ppm, which was considered comparable to a mineral dust loading of $7.3\,\mathrm{g\,m^{-2}}$. For that day, the simulated ensemble mean dust loading for Roza Pik varies between $0.97\,\mathrm{g\,m^{-2}}$ and $1.25\,\mathrm{g\,m^{-2}}$. Thus, there is an underestimation by at least a factor of 5.8. This could be a result of the averaging over 40 ensemble members where the main deposition of mineral dust is probably more spread out. For instance, on March 27, daily ensemble mean values of dust in snow up to $8.4\,\mathrm{g\,m^{-2}}$ still appear in region A. These values are found further south, on Turkish territory (41°3′ N 41°57′ E). One explanation for this might be that the mineral dust in the simulation was not transported as far north and that the dust deposited slightly earlier. Furthermore, in a single ensemble member, the dust loading in the top 10 cm varies on that day for Roza Pik between $1.88\,\mathrm{g\,m^{-2}}$ and $2.33\,\mathrm{g\,m^{-2}}$, which is more close to the observation. It must also be borne in mind that the model results are averaged over cells with a horizontal resolution of 10 km, whereby extreme values may be averaged out.

Moreover, it must be pointed out that currently only the ICON-ART AOD has been tested against measurements and not yet the amount of deposition. Therefore, it is recommended to evaluate deposition amounts with different measurements in future studies. Furthermore, due to the resolution of 10 km, the slopes follow only approximately the accurate profile. The slopes of the mountains are especially important in terms of the deposition processes. Dumont et al. observed larger concentrations of mineral dust on the southwest facing slopes. This is consistent with the results of this study. After the dust deposition event, the largest dust loads are on the southwest slopes and in the more southern mountains on Turkish territory.

This study is one of the first to show the complete elevation dependence of mineral dust deposition as well as the associated feedback and the resulting vulnerability of particular locations. In terms of elevation, there are different zones where different feedback predominates. During the dust event in the Caucasus, the largest concentration is between 1800–1900 m. However, the largest differences in region A among the other variables are often at other altitudes. For example, the reduction in albedo is much greater above 1900 m, despite lower dust concentrations. This means that the snow albedo above 1900 m is much more sensitive to even smaller amounts of mineral dust. Furthermore, since the radiative forcing is directly tied to the surface albedo, it means that the positive radiative forcing is also enhanced at higher altitudes. The positive radiative forcing is more sensitive to albedo change because of less atmospheric extinction of solar radiation at higher altitudes (Usha et al., 2020).

Dumont et al. (2020) showed four sites at different altitudes (1600, 1700, 1925, and 2200 m) above sea level. The conclusion of their study was that the earlier melt occurs especially at the higher elevations. Since the station at 2200 m is the most elevated study site, their study does not consider all altitudes. The strongest influence on the snow depth is at the altitude between 1700–2400 m. Thus, Dumont et al. captured the most relevant altitude range concerning the impact on snow height. However, the influence of mineral dust above this region is slightly diminished in the case of this dust event in the Caucasus. Moreover, it was found that the surface temperature as well as the 2m-temperature, are mostly increased at lower elevations. The differences between SDS and REF in both temperatures are highest at 1600 to 1700 m in the Caucasus. The reason for this phenomenon is that the snow depth in this zone is relatively small (on average 24 cm) in contrast to the higher elevations, and a fairly patchy snow cover (38 %) prevails. This means that snow cover is most likely thinned out here so that the surface albedo below the snow further darkens the surface albedo (apart from the direct snow albedo reduction). And beyond that, the snow cover partially melts away completely, allowing the revealed ground to enhance the absorption of solar energy. As a result, there is an average radiative forcing due to mineral dust deposition of 5.80 $\mathrm{W\,m^{-2}}$ at this altitude which results in higher surface temperature and 2m-temperature. This implies that even small amounts of mineral dust can have a large impact on the temperature in regions where there is only partial snow cover. When the snow coverage is largely closed, only small impacts are found on the surface and air temperature and the main consequence of an increased shortwave radiation absorption is the snow melt. This is consistent with the spatial distribution of the difference in temperatures between SDS and REF (Fig. 5.14). Increased temperatures are mainly found at the edges of the mountains and at the snow line.

With consideration of the whole simulation domain, even higher mountains with close proximity to dust sources are included. Therefore, the position of the most vulnerable zones shift towards higher elevations. For example, the impact of mineral dust deposition on snow height is most relevant between 2700–3800 m. This is due to the fact that the mineral dust is transported to even higher altitudes. However, even when considering the entire area, the influence on snow height does not steadily increase to the highest altitudes, but decreases again above 3200 m. Similar to the dust loading and the impact on the surface albedo, the responses of surface temperature and 2m-temperature shift towards higher altitudes (3000–3100 m) when averaged over the whole simulation domain. There are several regions where the snow cover is still patchy at those altitudes. The mean increase in surface temperature and 2m-

temperature is much higher at these altitudes as well as the increase in surface shortwave net radiation flux (39.53 $\mathrm{W\,m^{-2}}$). This implies that a vanishing of the snow cover at higher altitudes triggers stronger impacts. Therefore, the patchiness of the snow cover as well as the altitude must be considered when investigating the impact of dust deposition on the surface temperature and 2m-temperature.

Sarangi et al. (2020) found out that the reduction in snow albedo is stronger at higher altitudes with a vertical gradient of $-0.2\,\%\,\mathrm{km^{-1}}$. This results in an increase in radiative forcing of $3\,\mathrm{W\,m^{-2}\,km^{-1}}$ over Western Himalaya. The intensification of the albedo reduction at higher altitudes is observed but rather fluctuates above 3000 m. Considering the snow albedo reduction in the whole simulation area between 2000–4000 m, there is an average decrease in surface albedo which is an order of magnitude larger ($-2.83\,\%\,\mathrm{km^{-1}}$). The respective increase in radiative forcing towards higher elevations is $21.73\,\mathrm{W\,m^{-2}\,km^{-1}}$. The slopes mentioned by Sarangi et al. (2020) are temporal averages (March–August), whereas this study presents the short-term impacts during a dust event. Moreover, the results of this section focus on a specific time around noon when the impacts reach their daily maximum. Averaged over the entire day, the impacts would be smaller, which could explain the large discrepancy. Furthermore, Sarangi et al. (2020) found a decrease in the strength of the radiative forcing to dust above an altitude of 4500 m. In the case of this study region, areas that are located in such altitudes are not included. However, a decrease in the radiative forcing is also observed above 4000 m.

Another finding of this study is that the amount of dust is not the most important factor for the degree of response to dust in snow, nor is topography alone. This has been shown in the study of region B. The terrain is relatively flat and the amount of dust in contrast to region A is significantly lower (maximum value compared to region A about one seventh). But even here, the mineral dust has a strong influence on surface albedo, surface temperature, 2m-temperature and snow depth. Here, a major factor is the fraction of the snow coverage. At the snow line, the snow layer becomes thinner and more patchy. These areas exhibit the largest differences in the examined variables between SDS and REF.

Another interesting finding is that far-reaching changes in large-scale atmospheric conditions develop due to the changes in surface properties caused by the deposition of mineral dust on the snow. In region B, a redistribution of precipitation takes place. A lake effect seems to form, which leads to an increased precipitation northeast of the Sea of Azov (northern extension of the Black Sea). Also, in region A, a slight increase in precipitation was observed in the proximity to the Black Sea. This effect is evident in the mean of the ensemble simulation and is therefore a consistent change in atmospheric conditions. A possible explanation for this would be that even the relatively small rise in surface temperature and 2m-temperature in the west of the Black Sea is sufficient to increase the relative humidity and thereby induces a more rapid precipitation of snow when the westerly wind passes over the Sea of Azov. The increased snow fall is located directly at the snow line and counteracts the mineral dust effect. Dust concentrations are covered by clean and fresh snow which has a very high albedo. However, it will be discussed in the next section that this change in precipitation is not significant and could be caused by model internal variability.

In conclusion, despite the averaging over the ensemble, there are still interfering phenomena that persist due to consistent changes in weather conditions on a large scale. Therefore, in the following section,

another tool is applied to eliminate the interfering effects and to investigate the feedback of the mineral dust on snow in more detail.

5.4 Relationships Between Surface Albedo and the Feedback

Previously in this section, mean values and standard deviations of the ensemble simulation have been presented. The ensemble technique was applied in a first attempt to oppose the noise of natural variability. However, it became apparent that even with this approach, effects develop that do not result directly from the reduction in snow albedo at a specific location. Possibly, these effects are triggered by the mineral dust deposition but might evolve and strengthen through other influencing factors. To investigate the local and instantaneous effects, and to obtain a high confidence that the effects can actually be attributed to the aerosol deposition on snow, a significance test is performed.

The method that is applied here focuses on the significance of individual cells in the context of all paired simulations. The Wilcoxon signed-rank test (Wilcoxon, 1945) is applied, testing each cell of the 40 ensemble members including the aerosol-snow-albedo interaction against the 40 members without the interaction. The Wilcoxon signed-rank test is applicable for related data. The difference between the two samples does not have to be uniformly distributed. The test evaluates whether the two samples originate from the same distribution and returns a p-value which describes the probability of obtaining these results if the two sets originate from the same distribution.

In most studies, all values where $p < 0.05$ are declared as significant results and $p < 0.01$ as highly significant results. This 'naive-stippling' approach leads to many false detection of seemingly significant cells (Wilks, 2016). To minimize the false detection rate (FDR), the approach of Wilks (2016) is applied here. In contrast to the stippling method, where the condition for significance is fixed to a constant p-value, this method uses a variable threshold p^*_{FDR}. This means that the p-values for every cell are ranked from smallest to largest and then tested against the condition

$$p_r \leq \frac{r}{N_p}\alpha_{FDR}, \tag{5.2}$$

where N_p is the total amount of p-values, p_r the p-value with rank r and α_{FDR} a chosen control level that is set to 0.2 in this study. The threshold p^*_{FDR} is the highest p-value that falls into this condition. A larger size of the statistics increases the probability for the occurrence of extremely small p-values. This phenomenon is represented in the approach of Wilks, 2016.

5.4.1 Summary of Statistical Characteristics

First of all, this section lists the statistical characteristics of the ensemble simulation without significance test, so that the impact of the applied method can be discussed in the following section. Tab. 5.1 summarizes the arithmetic average and the median of dust loading (top snow layer) as well as the differences in diffuse surface albedo, shortwave net radiation flux, snow height, surface temperature, and 2m-temperature between SDS and REF. The statistical characteristics are shown for the whole simulation area, region A and region B at t_{176}. Furthermore, the maximum and minimum value of the cells in the respective regions are listed, as well. The table summarizes the statistics regarding figures

Table 5.1: Mean, median (Med), standard deviation (σ), minimum and maximum value of the entire simulation area, the region A and B, regarding the amount of mineral dust in the top snow layer (SDS), the differences between SDS and REF of surface albedo a_d, surface shortwave net radiation flux sw_{net}, snow height h_{snow}, surface temperature T_g, and 2m-temperature T_{2m} on March 29, 2018, 8 UTC.

Var	Unit	Dom	Mean	Med	σ	Min	Max
			0.10	0.00	58.00	0.00	32.94
m_{dust}	$\mathrm{g\,m^{-2}}$	A	0.90	0.64	0.96	0.00	11.67
		B	0.11	0.06	0.14	0.00	1.66
			−0.38	−0.03	1.23	−38.36	8.81
Δa_d	%	A	−1.42	−0.94	1.50	−13.42	0.92
		B	−0.62	−0.25	1.45	−15.97	6.86
			1.49	0.23	9.23	−76.49	303.40
Δsw_{net}	$\mathrm{W\,m^{-2}}$	A	7.41	5.96	11.76	−34.95	92.46
		B	3.20	2.23	10.82	−60.31	108.24
			−0.05	0.00	0.32	−10.15	1.87
Δh_{snow}	m	A	−0.47	−0.39	0.67	−3.12	1.60
		B	−0.09	−0.04	0.24	−1.73	0.88
			0.03	0.01	0.23	−2.06	9.31
ΔT_g	K	A	0.07	0.01	0.22	−0.56	2.01
		B	0.06	0.01	0.23	−1.09	2.72
			0.01	0.01	0.13	−0.95	3.22
ΔT_{2m}	K	A	0.03	0.02	0.10	−0.31	0.63
		B	0.04	0.03	0.14	−0.59	1.29

5.6–5.10, 5.14, 5.18, and 5.19. Only cells with at least one ensemble member containing snow are included in the statistics.

The statistics show that on average the feedback appears small at first, but locally the values can be large. This was already observed in the spatial patterns. On average, the reduction in albedo in region A is more than twice as strong (than region B) with a mean value of −1.42 % (−0.62 %). However, there are locally larger differences in region B with a reduction in surface albedo up to −15.97 % (region A: −13.42 %). If the entire simulation area is considered, a reduction of up to −38.36 % can occur. Accordingly, the radiative forcing in region A is more than twice as large as in region B. Surprisingly, the average reduction in snow depth in region A appears 5 times higher. However, looking at the largest local reduction in snow depth, which is −3.12 cm in region A, it becomes clear that the maximum effect is also about twice compared to region B (−1.73 cm). In terms of surface temperature and 2m-temperature, stronger increases occur in region B, in each case. The maximum warming of the surface in SDS is 2.01 K in region A and 2.72 K in region B. The maximum warming of the 2m-temperature is 0.63 K in region A and 1.29 K in region B. The cloudiness as well as the precipitation show no considerable differences between SDS and REF. Therefore these variables are not listed in Tab. 5.1.

The correlation between diffuse surface albedo in snow cells and the amount of dust, snow depth, surface temperature, 2m-temperature, and shortwave net radiation flux at time t_{176} is shown as density plots in Fig. 5.20. In the comparison of the darkening of the surface albedo with the amount of dust in the uppermost snow layer, it becomes apparent that almost all values occur in the second quadrant. A large reduction in albedo is always associated with increased dust amounts. In contrast, an increase in surface albedo is never coupled with a higher dust contamination and thus, the data in the first quadrant are always close to the x-axis. It is worth noting that there is no linear relationship between albedo change and dust loading. The data are scattered over the entire second quadrant.
The difference in snow height with respect to the difference in surface albedo shows some linearity. The snow height decreases with the reduction in surface albedo in SDS compared to REF. A reduced surface albedo of $-20\,\%$, is linked to a reduction in snow height of at least $-2.5\,\mathrm{cm}$. However, areas with a slightly increased snow cover also occur in SDS. In these cases, there is usually an increase in snow albedo (first quadrant). In the second and fourth quadrants, there are very few occurrences that are close to the origin.
Similar to the dust mass, the surface temperature does not show a linear relationship to the change in surface albedo. However, in Fig. 5.20 it can be seen that with the decrease in albedo, a clear increase in surface temperature can be found in many cases. The majority of the occurrences are scattered in the second quadrant. A lower surface temperature is often associated with an increased albedo (fourth quadrant). Here, the extent is relatively small. Only few cases are in the first and third quadrant. This means that a lower surface temperature occurs only in extreme exceptions on surfaces that have a reduced surface albedo and vice versa. Higher surface temperatures occur very rarely with an increased albedo.
The 2m-temperature has a similar pattern, but still shows unique characteristics. The majority of the data points are located in the second quadrant. However, the impact on 2m-temperature is smaller than the impact on surface temperature. The increase in 2m-temperature does not exceed $3.22\,\mathrm{K}$. In addition to a warming due to a decrease in surface albedo and a cooling due to an increase in surface albedo, values in the third quadrant indicate that on several occasions a cooling happens though the surface albedo in SDS is lower.
The surface albedo is a factor in the radiation balance at the surface, so a linear relationship between surface albedo and shortwave net radiation flux is expected for the same atmospheric conditions. This is clearly shown by the comparison of the change in these two quantities. The radiative flux into the surface increases with the reduction in surface albedo. This relationship is particularly pronounced in the second quadrant when the albedo is extremely reduced.
In all cases, not only one or two quadrants are occupied in the comparison of the respective variables. Therefore, effects occur which are contrary to the expectations. Fig. 5.20 shows the results of the cells covering the whole simulation area. For a more detailed relationship in region A and region B, respective figures can be found in the appendix (Fig. B.1 and Fig. B.2).

5.4.2 Statistical Significance

This section presents the results with the non-significant data removed. For this purpose, the Wilcoxon signed-rank test was applied for each variable, and the condition according to Eq. 5.2 was examined.

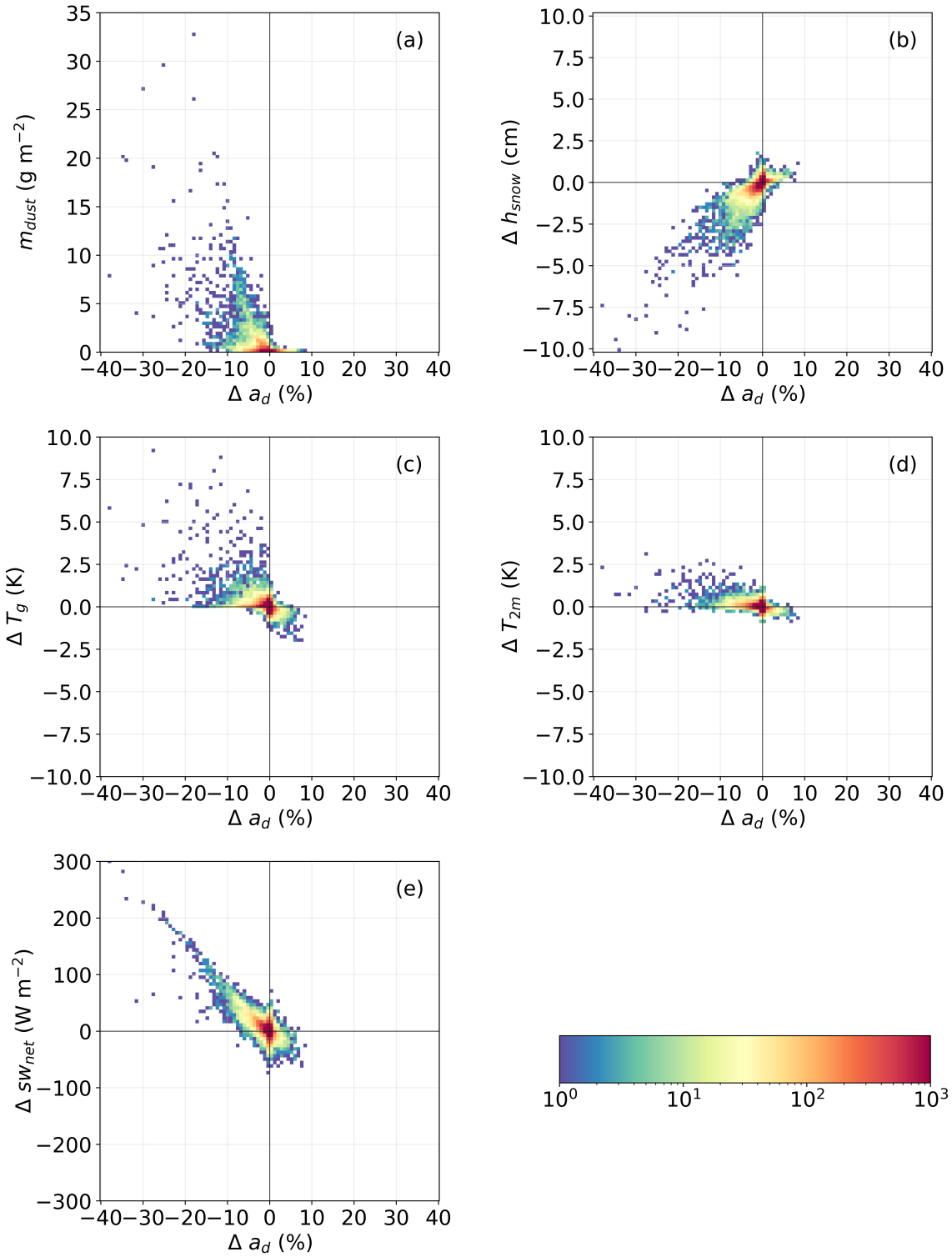

Figure 5.20: Density plots of the local SDS ensemble mean dust loading in the top snow layer m_{dust} (a) and the the local differences between SDS and REF of snow height h_{snow} (b), surface temperature T_g (c), 2m-temperature T_{2m} (d), surface shortwave net radiation flux sw_{net} (e) in comparison to the difference in diffuse snow albedo between SDS and REF on March 29, 2018, 8 UTC.

The resulting data set is considerably smaller than the original dataset, and the size depends on the corresponding variable. The largest amount of significant cells is obtained by the analysis of surface albedo, followed by the snow height.

Fig. 5.21 shows the results of the significance test of diffuse surface albedo and surface shortwave net radiation flux. They correspond to Fig. 5.6 and Fig. 5.9 but the non-significant values are masked. It is clear that mainly the results in complex terrain, where the amount of dust is higher (Fig. 5.7), produce a significant result in the difference in albedo. Furthermore, a significant result appears at the snow line in Kazakhstan. The shortwave net radiation flux mirrors the difference pattern of the surface albedo at the snow line, northwest of the Black Sea and in the mountains. However, seemingly random distributed significant values also occur in a few cases within the entire simulation area.

A situation similar to the surface albedo arises for the difference in snow height (Fig. 5.22), but far fewer significant cells are present in this case. For example, there are some significant results for the change in surface albedo in the Alps, the Pyrenees, and the Ukraine. However, the change in snow depth, located at the same spots, are not considered significant. The change in snow depth is mostly significant in the Caucasus, in the mountains of Turkey and Central Asia, and at the snow line in Kazakhstan.

Fig. 5.23 illustrates the corresponding figure for the surface temperature and 2m-temperature. Here, it is particularly remarkable that the data set was strongly depleted by the significance analysis. There are hardly any significant differences in region A. Only in the eastern half of region B temperature differences are recognized as being significant. These findings are also located at the snow line in Kazakhstan. However, the feedback to mineral dust is largely formed with a certain sign in the significant results of the respective variables. Surface albedo and snow depth are reduced due to the deposition. The surface shortwave net radiation flux, the surface temperature, and 2m-temperature, however, are increased. For a more detailed view of region A and region B, supplementary figures are provided in the appendix (Fig. C.1 and Fig. C.2).

Fig. 5.24 corresponds to Fig. 5.20, and presents the frequency of significant differences between SDS and REF of the following variables: surface albedo, shortwave net radiation flux, snow depth, surface temperature, and 2m-temperature. The mineral dust mass of the top snow layer is plotted against the corresponding significant changes in surface albedo and the significant changes of the other variables are plotted against the corresponding changes in surface albedo. Considered are all cells of the whole simulation domain at t_{176}. Clearly, many quadrants have been purged by the selection process, and only one quadrant dominates in each case. For example, in the comparison of the difference in snow depth and surface albedo, almost all values appear in the third quadrant. This means that almost all significant cells experience a reduction in snow depth, and this is coupled to a reduction in surface albedo.

For the difference in surface temperature, 2m-temperature, and also shortwave net radiation flux, it is the second quadrant that is predominant in each case. This means that increased values of the respective variables occur on surfaces associated with a lower surface albedo. There is no linear relationship between the differences of the two temperatures and the difference in albedo. There are also a few spots in the fourth quadrant which suggest a significant increase on surfaces associated with a decrease in albedo. In turn, a linear relationship between the difference in shortwave net radiation flux and the difference in surface albedo is evident. On the y-axis, some points are in the negative as well as in

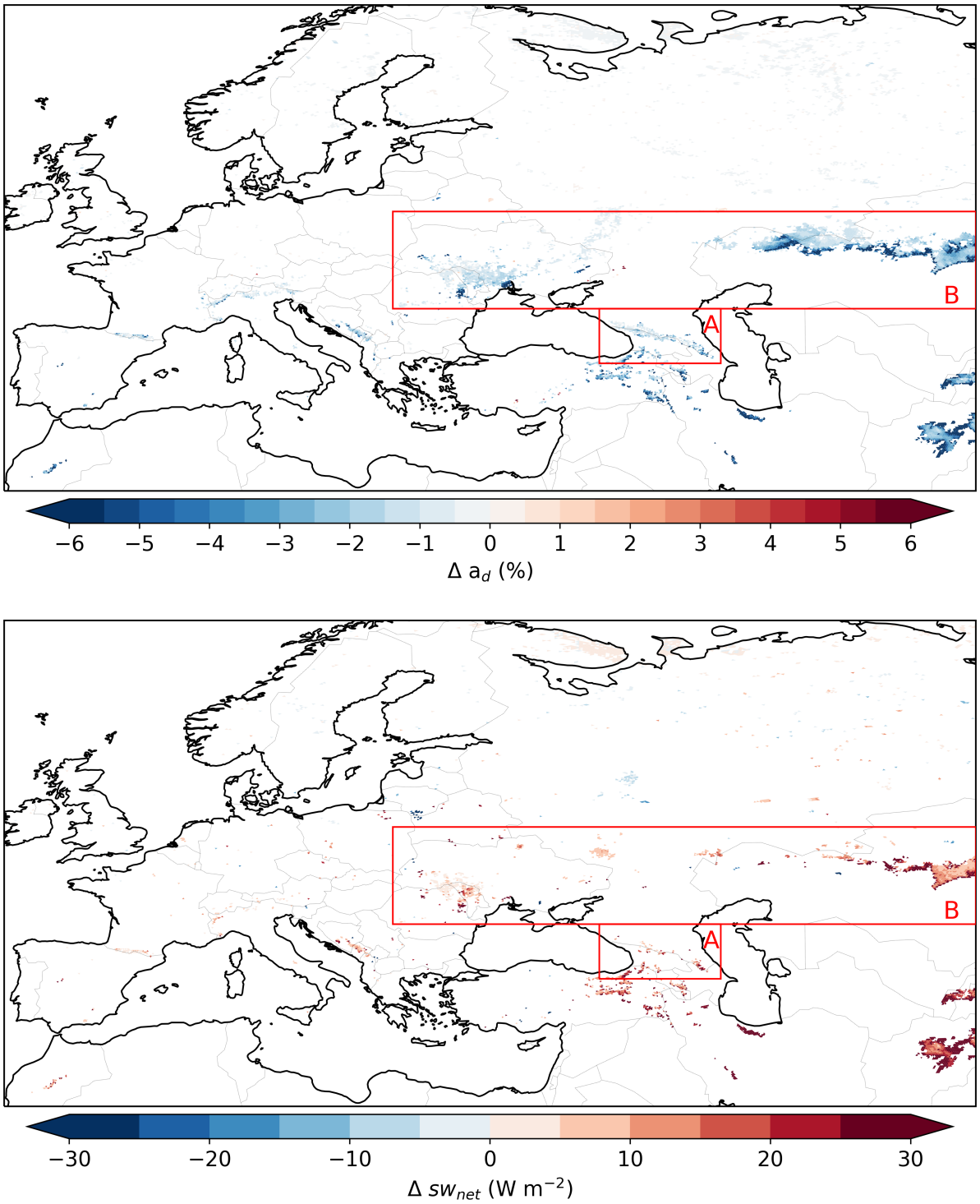

Figure 5.21: Significant ensemble mean differences between SDS and REF of diffuse surface albedo a_d (top) surface shortwave net radiation flux sw_{net} (bottom) on March 29, 2018, 8 UTC.

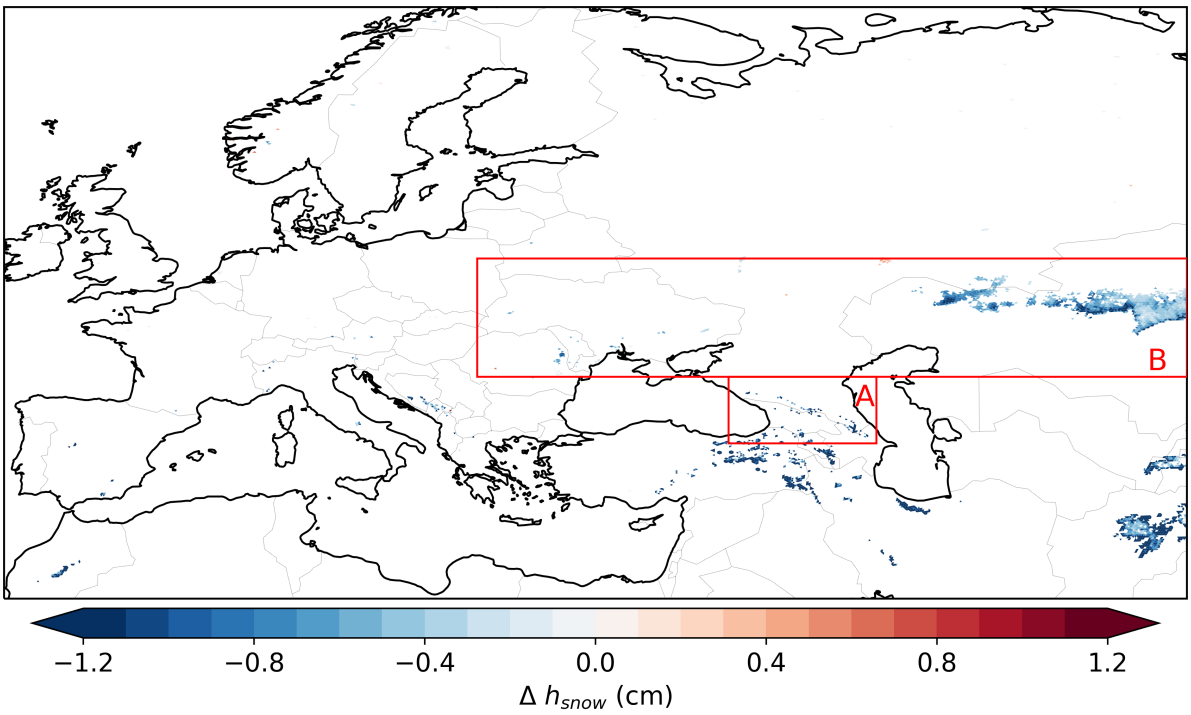

Figure 5.22: Significant ensemble mean differences between SDS and REF of snow height h_{snow} on March 29, 2018, 8 UTC.

the positive range. These indicate increases and decreases of the radiation flux which are not attributed to changes in the surface properties, but rather to atmospheric conditions, such as cloud cover. The relationship between the significant changes in surface temperature and the percentage of snow cover are shown in Fig. 5.25. It is evident that with smaller fractions of snow cover larger effects on the surface temperature occur.

To investigate the relationship between the reduction in surface albedo and the respective variables, the averages of the significant results are listed in Tab. 5.2. In the other column, the according mean difference in surface albedo of the corresponding cells is listed. Since the signal of natural variability was reduced by the significance analysis, it can be assumed that the change is related to the disturbance of the surface albedo. With this assumption, the result is that a decrease of $-2.93\,\%$ in albedo already leads to an average positive radiative forcing of $19.15\,\mathrm{W\,m^{-2}}$. A reduction in albedo of $-4.28\,\%$ results in a loss of snow depth of $-1.14\,\mathrm{cm}$. The surface temperature is more sensitive than the 2m-temperature to the reduction in albedo, as noted in the previous results. Surface temperature increases on average by $0.96\,\mathrm{K}$ with a surface albedo reduction of $-4.78\,\%$, while the 2m-temperature increases by $0.44\,\mathrm{K}$ with a similar reduction in albedo of $-4.47\,\%$.

Regarding the shortwave radiation, the mean values of the smaller regions are of the same order of magnitude. For example, the mean positive radiative forcing in region A is $18.47\,\mathrm{W\,m^{-2}}$ with a reduction in surface albedo by $-2.72\,\%$. In region B, the radiative forcing is slightly lower ($15.96\,\mathrm{W\,m^{-2}}$), but the reduction in albedo is also not as strong ($-2.50\,\%$). The reason is that this region was not as heavily affected by the dust event.

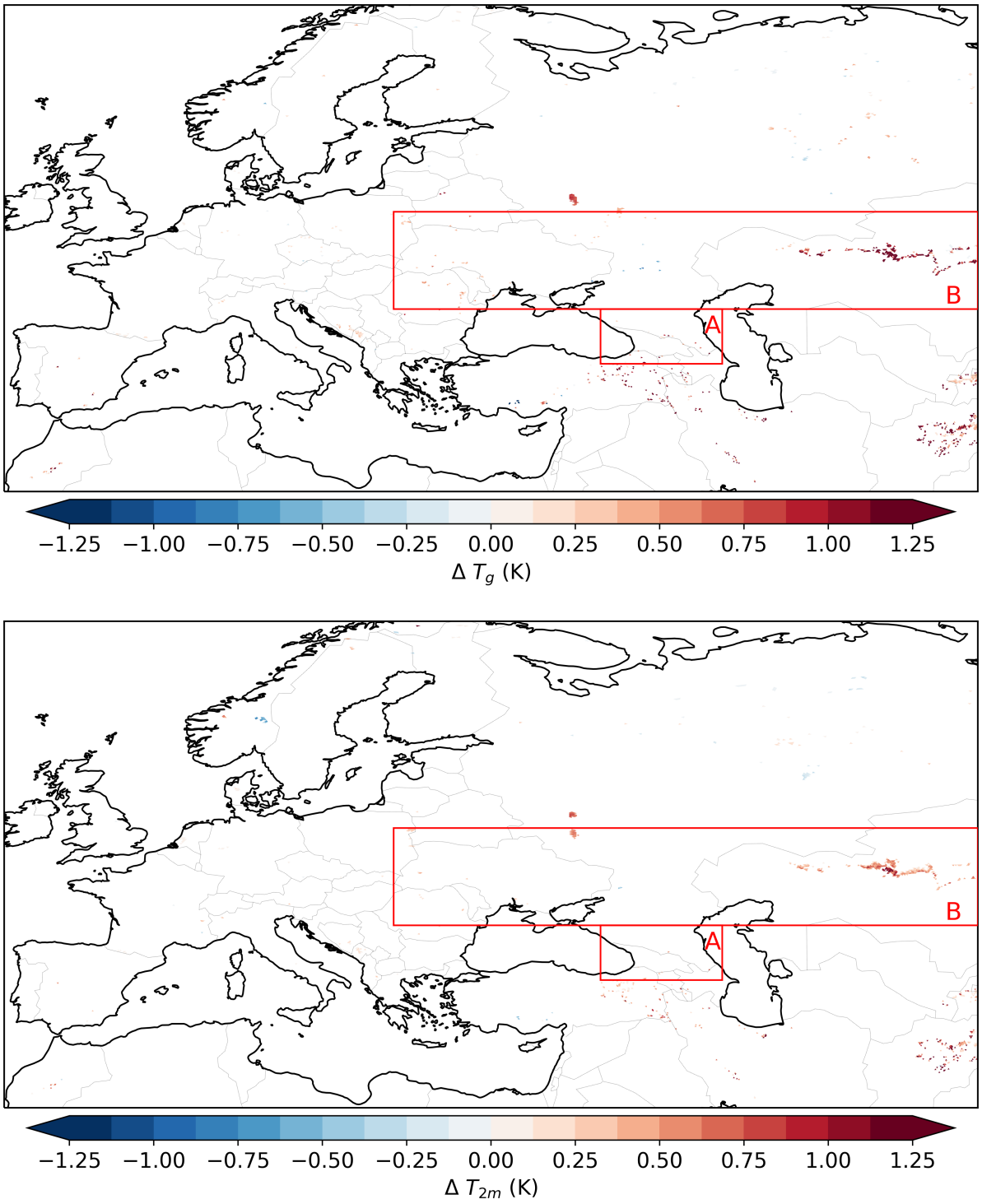

Figure 5.23: Significant ensemble mean differences between SDS and REF of surface temperature T_g (top) and 2m-temperature T_{2m} (bottom) on March 29, 2018, 8 UTC.

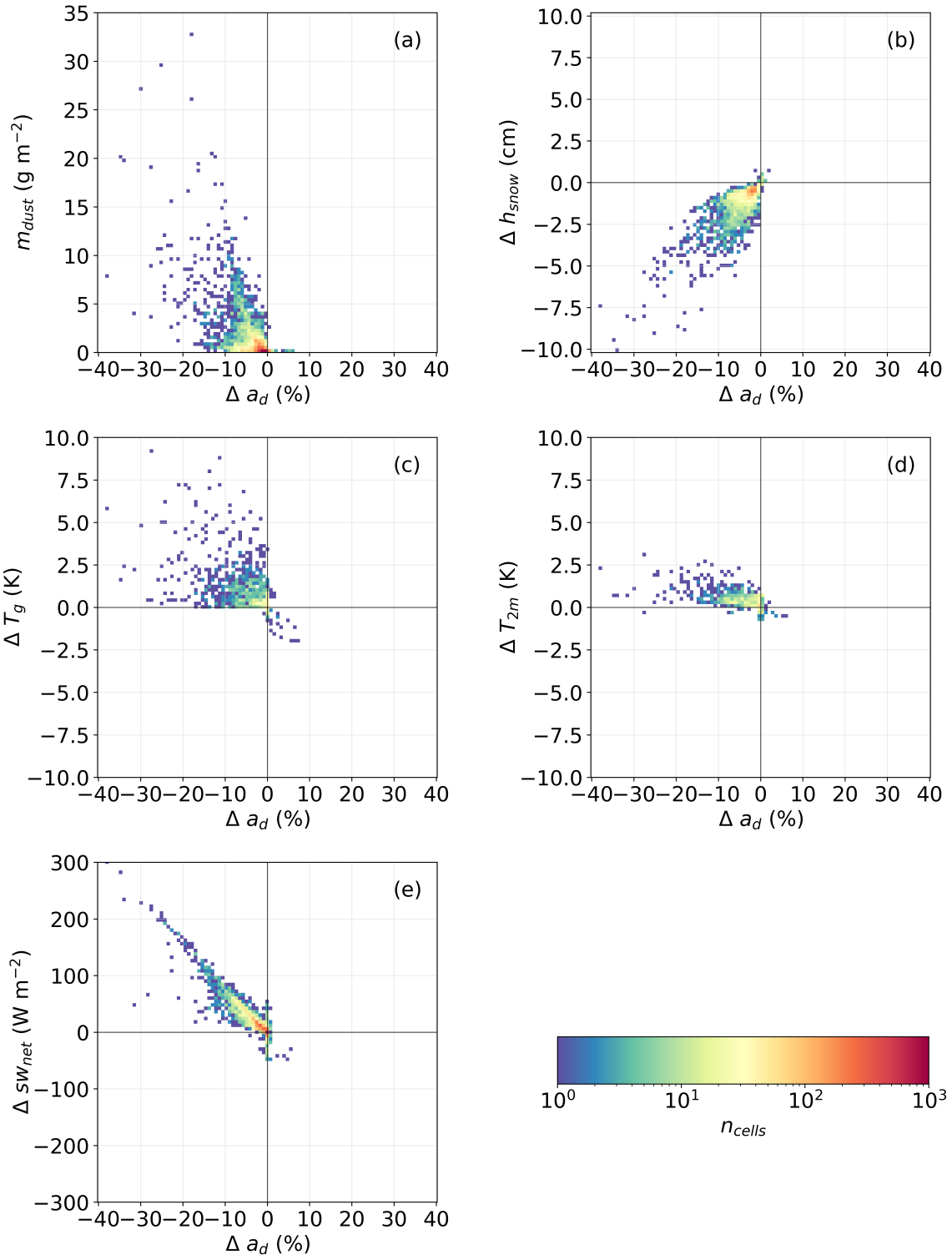

Figure 5.24: Density plots of the local ensemble mean dust loading m_{dust} in the top snow layer in SDS (a), the significant local differences of snow height h_{snow} (b), surface temperature T_g (c), 2m-temperature T_{2m} (d), surface shortwave net radiation flux sw_{net} (e) in comparison to the difference in diffuse snow albedo between SDS and REF on March 29, 2018, 8 UTC.

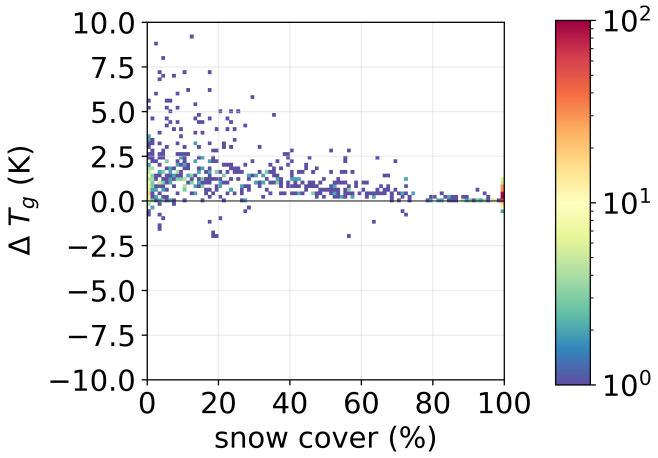

Figure 5.25: Density plot of the significant local mean differences between SDS and REF of surface temperature T_g in comparison to mean snow cover fraction in SDS on March 29, 2018, 8 UTC.

Table 5.2: Average of the statistically significant feedback in surface shortwave net radiation flux sw_{net}, snow height h_{snow}, surface temperature T_g, and 2m-temperature T_{2m} due to the snow albedo perturbation by mineral dust and the associated disturbance in diffuse surface albedo on March 29, 2018, 8 UTC.

Var	Dom	Mean of significant differences		Mean of associated surface albedo difference
		19.15	$\mathrm{W\,m^{-2}}$	−2.93 %
Δsw_{net}	A	18.47	$\mathrm{W\,m^{-2}}$	−2.72 %
	B	15.96	$\mathrm{W\,m^{-2}}$	−2.50 %
		−1.14	cm	−4.28 %
Δh_{snow}	A	−1.36	cm	−2.83 %
	B	−0.60	cm	−3.41 %
		0.96	K	−4.78 %
ΔT_g	A	0.69	K	−3.96 %
	B	0.92	K	−4.50 %
		0.44	K	−4.47 %
ΔT_{2m}	A	0.30	K	−4.57 %
	B	0.49	K	−4.20 %

In addition, it is also noticeable in this table that the additional radiation absorption is converted differently in the particular regions. For instance, in region A, the largest snow reduction is present with -1.36 cm (region B: -0.6 cm) and in region B there is a larger increase in surface temperature of 0.92 K and 2m-temperature of 0.49 K compared to region A (0.69 K and 0.3 K). The feedback shows some consistency for half of the variables. It increases with larger perturbation in surface albedo. This behavior is apparent for the shortwave net radiation flux and for surface temperature. Snow depth, on the other hand, does not show this consistency. Although the mean reduction in albedo is stronger on average in region B and over the entire simulation area, the strongest reduction in snow depth is nevertheless evident in region A. The values for 2m-temperature can also not simply be transferred. Therefore, the analysis shows that the additional radiation absorption due to the mineral dust can be estimated to some extent, but the feedback is strongly dependent on snow cover and responds differently in the particular regions.

5.4.3 Discussion

An ensemble simulation has already been used in the study of Dumont et al. (2020) using a one-dimensional snow model (CROCUS). Lafaysse et al. (2017) had previously found out that such a set up for the applied snow model with 35 members was sufficient to explain the simulation errors of 50 to 70 %. The problem of model internal variability is well known (Rahimi et al., 2020; Usha et al., 2020), but so far only minor attempts have been made to account for it. For example, Usha et al., 2020 created a composite of an ensemble consisting of 3 members, disturbing their reference run (without snow albedo effect) at the beginning, in order to assess the variations in meteorology. When considering a large area, such as the entire simulation area, it is difficult to filter out the influences of natural variability. This can be seen in the low mean values in the different variables. There are large areas, where the amount of dust is too small to see a feedback. However, if one wants to study the relationship between dust and feedback, the method applied has turned out to be an appropriate approach.
Regarding the albedo, the snow-darkening effect is dominating in region A, because of the large amount of dust and only little interfering noise. For the other regions, the effect is only properly visible after the data set has been processed. For example, region B covers a large area that does not experience a large dust accumulation and therefore has a reduced chance to properly capture the impacts of the dust. After the significance test, the amount of the mean difference in surface albedo due to the mineral dust is in a similar range in all regions. It can be concluded that the additional energy resulting from this instance is converted differently and varying feedback can be observed. Most of the additional shortwave radiation absorbed due to the dust in region A results in the melting of snow, whereas the radiative forcing in region B leads to a heating of the surface and the air temperature instead. The reason for this is that the surfaces in A, where dust deposits, is mostly covered by a thick snow cover, whereas the dust deposition coincides with patchy and thin snow at the snow line (B). There is still snow melt happening in region B but the solar energy is more likely to hit the surface and to transfer into it instead of the snow layer. Still, it has to be mentioned that this conclusion is drawn from results at a specific point of time and already melt out snow is not considered here. It is difficult to track the long term snow reduction in region B which could be investigated more thoroughly by conducting simulations over the whole season.

However, sorting out the non-significant differences also poses challenges in interpreting the results for some variables. In some areas, such as region A, only a few significant changes occur, so that the number is too small to draw a reliable conclusion. Especially the surface temperature and the 2m-temperature are critical since they are easily influenced by changed atmospheric conditions.

6 Summary and Conclusions

In order to answer the questions raised in section 1, the model ICON-ART was improved by implementing a new snow albedo parametrization following Wiscombe and Warren (1980) and Warren and Wiscombe (1980). For this purpose, a new prognostic variable, the optical equivalent snow grain radius, and the corresponding Mie coefficients in form of LUTs were implemented. In many weather prediction and climate models, a fairly simple albedo parametrization is used for snow. Often, this snow albedo consists only of a broadband albedo that applies to the entire spectrum of shortwave radiation. Typically, this value oscillates between a fixed maximum and minimum value and decreases at a defined rate over time. The parameterization implemented here enables the computation of a spectral snow albedo. This allows the modification of the snow albedo in certain spectral ranges by atmospheric conditions. Furthermore, the aerosol optical properties provided by the ART module were included in the new parametrization of the snow albedo to allow the simulation of the influence of mineral dust deposition on the optical properties of the snow surface. The mineral dust deposited on snow is transferred to the top layer on account of the new developments and migrates to deeper snow layers over time. When the snow melts, these aerosols can also resurface. At the top of the snow pack, the interaction of the optical properties of snow and aerosol takes place.

Two case studies were conducted to analyze the properties of this albedo parametrization and the resulting feedback to a perturbation. The first is a simulation of the optical properties of clean snow during the PAMARCMiP measurement campaign in March 2018. This case study focused on snow aging processes in an evaluation of simulated optical equivalent snow grain radius and snow albedo versus the observations. It was shown that the model captures the snowfall events well compared to observations and therefore drives metamorphism at the proper periods. By using the data of Kaempfer and Schneebeli (2007), the parametrization according to Essery et al. (2001) could be adjusted and a reasonable prediction of snow metamorphism could be performed which is consistent with the observations in Greenland. There was a good agreement with the observation of the snow albedo under cloudy conditions. However, the clear sky snow albedo was overestimated. Further measurement data on snow albedo and atmospheric composition are needed to clarify the deviations between model and observation under cloud-free conditions.

The second case study focused on the impact of mineral dust deposition on the newly implemented spectral snow albedo during a large Saharan dust deposition event. This event occurred in spring 2018 and affected snow surfaces in Eastern Europe and western parts of Asia. The dust was emitted, transported, and deposited online in the experiment, as was the interaction of the optical properties of snow and dust particles. Therefore, the feedback with the snow cover and the atmosphere were also calculated online. Unlike an one dimensional model, often used to study the dust on snow events, the influence of dust is much more difficult to capture with a fully coupled three dimensional land and

atmosphere model. As e.g., Rahimi et al. (2020) mentioned in their study, there exists model internal variability that overlaps the effect of the impurities in snow. To counteract this source of uncertainty, an ensemble simulation set up with a total of 80 ensemble members in a fully coupled three dimensional model was applied to investigate the impact of dust on snow albedo. The ensemble was composed by changing model internal tuning factors at the beginning of the simulation. Half of the members included the aerosol snow-darkening effect and for the other half, the snow was assumed to be clean. By averaging the results of the ensemble, the actual influence of the aerosol became detectable. Evidence of statistical significance was obtained by applying the Wilcoxon signed-rank test (Wilcoxon, 1945) and the significance evaluation described by Wilks (2016).
The scientific question which was addressed in the Greenland case study is:

Which processes have the most significant impact on the spectral albedo of pure snow which are not captured by a broadband albedo?

Interestingly, the evaluation with measurements revealed that the spectral albedo is very strongly dependent on the cloud cover and the presence of aerosols and gases. These atmospheric components selectively absorb within certain wavelength ranges and therefore actively change the value of the snow albedo which is spectrally highly variable. These processes are anything but negligible and can account for several percent of snow albedo on any given day. This study shows that a simplified broad band snow albedo parametrization, as they are used in many models, is inaccurate and disregards a number of influences. The diurnal variability and the dependence on the atmospheric composition are two of these important features. Another substantial impact on the albedo results from the snow metamorphism which has its impact on the near infrared albedo and greatly varies with snow temperature. At Arctic conditions the growth of the optical equivalent snow grain size proceeds very slowly. Therefore, the parametrization by Essery et al. (2001) had to be adjusted. However, it was found that the variability in the spectral albedo which is altered by the atmospheric condition is able to overlay the variability that comes with the snow metamorphism. It is therefore important that a proper representation of the atmospheric composition is achieved for the accurate prediction of the spectral snow albedo.
One of the questions that was addressed in the case study of the Saharan dust outbreak is:

What is the spatial and temporal distribution of mineral dust deposition during a major Saharan dust deposition event in Eurasia and how large is the feedback resulting from the modified snow albedo?

The dust loading in snow was found to be spatially highly variable and dependent on region, altitude, and slope orientation. Mostly mountainous regions are affected and a relatively flat area in Kazakhstan, the latter probably due to the proximity to dust sources. Furthermore, especially southwestern slopes are particularly contaminated with dust particles. It is therefore highly important to simulate the aerosol emission, transport and deposition online to achieve a proper distribution of the mineral dust on snow. The dust concentration increases and fluctuates according to the precipitation. The magnitude of the impact, however, continues to increase with simulation time. The dust loading in the top snow layer

exceeds 11 $g\,m^{-2}$ in the area around Georgia and the daily average of the ensemble mean over this region reaches a magnitude of the snow-darkening effect up to a reduction of $-1.50\,\%$. Furthermore, the albedo reduction reaches locally an intensity of $-13.00\,\%$. The relationship that was found between albedo reduction and shortwave radiation net flux is linear but not the relationship between albedo reduction and snow depth decrease, temperature increase or 2m-temperature increase. It was found that a reduction in surface albedo by $-2.93\,\%$ leads on average to a positive radiative forcing of $19.15\,W\,m^{-2}$. A snow-darkening of $-2.83\,\%$ in the Caucasus Mountains is associated with a decrease in snow height by $-1.36\,cm$. At the snow line, a decrease by $-4.5\,\%$ of the surface albedo leads on average to a surface warming by 0.92 K. The 2m-temperature is less affected and increases by 0.49 K with a darkening of the snow albedo by $-4.20\,\%$.
This leads to the question:

Which kind of interference results from model internal variability and how significant are the effects?

It was demonstrated that performing an ensemble simulation with consideration of the averaged results can contribute to separating the signals of the albedo perturbation from the signals of the model internal variability. Since the influences of natural variability occur randomly and are both positive and negative, they largely eliminate themselves upon averaging. However, signals that develop through a consistent perturbation, such as the snow-darkening, are not averaged out because they have a specific manifestation. The major interfering factor in studying the feedback to the snow-darkening effect regarding the shortwave radiation flux turned out to be the changes in the location of clouds. When it comes to surface and 2m-temperature large scale weather systems interfere with the responses to the snow-darkening. In addition, variations in the patterns of precipitation have proven to be the largest interfering element when examining the change in snow cover. However, there is a limiting factor for the method due to the severity of noise in the results. For a large part of the simulated domain, the significance could not be clearly determined, especially looking at the feedback. It becomes a problem especially when examining smaller regions that have only a few cells. However, when looking at larger areas, this method has proven useful as it allows a better insight into the relationship between the darkening of snow albedo and other variables. Another interesting question that was addressed is:

Are there large-scale atmospheric changes due to the disturbance of the snow albedo?

In the short-term simulation of 10 days it was found that a modification of the large-scale atmospheric conditions can be triggered by the perturbation in snow albedo leading to a consistent change in precipitation pattern, especially close to water bodies. This result appears consistent throughout the majority of the ensemble. However, the significance test showed that the precipitation changes and the induced changes in the other variables are not significant in these areas. The alteration could still be attributed to the model internal variability. Simulations of longer periods following this study can bring more insight into the nature of the changes in precipitation patterns. Hence, the effects in this short period of time are limited to local effects which are significant in snow depth, shortwave radiation net

flux, surface temperature and 2m temperature. The concluding question to this study is:

Are there regions in Western Eurasia that are particularly susceptible to impacts from mineral dust on snow?

There are just a few studies that investigated the height dependence of the impact of mineral dust on the surface albedo and the related radiative forcing. But in this study, a first attempt to resolve the continuous height profile of repercussions in snow height, surface temperature and 2m-temperature was conducted. The response of snow albedo as well as the radiative forcing is in agreement with previous studies (Dumont et al., 2020; Sarangi et al., 2020) regarding a stronger decrease in albedo and a stronger radiative forcing at higher altitudes. In both the spatial investigation and the elevation analysis, the maximum amount of dust does not necessarily coincide with the greatest reduction in surface albedo. In fact, there is no linear relationship between the deposition amount and the reduction in snow albedo. The effect turned out to be an interplay of the dust deposition amount, altitude, snow depth, and the fraction of the snow coverage.
Furthermore, it was found that the type of the feedback changes in different altitudes and that the influence on the snow albedo is not equally transferable to the magnitude of the feedback in other variables. For the snow depth, a strong influence at intermediate altitudes was found despite a strong darkening of the snow at higher altitudes. Towards the mountain peaks, the feedback on snow depth is weak. Also, the feedback on surface temperature and subsequently on the 2m-temperature has its peak not at higher altitudes, but mainly at the snow line, where the snow cover is patchy and thin. Here, the exposure and thinning of the snow occurs due to the mineral dust and the resulting strongest heating of the surface and 2m-temperature. The snow cover fraction was found to be most important in predicting the possibility of increased surface temperature.
In conclusion, to estimate the responses to the snow-darkening effect, it is important to consider the aspects of exposure to dust deposition, altitude and snow coverage of the study region. Mountain ranges are especially affected by mineral dust deposition, in particular the south facing slopes in this case. The resulting response is mainly the reduction in snow cover. Moreover, the snow line in Eurasia is one of the most sensible regions despite the flat area since the snow cover fraction is small. This leads mainly to a surface warming because of the accelerated retreat of the snow line to the north and exposure of the darker ground.

A Supplementary Figure: Temporal Evolution Across the Entire Simulation Area

In section 5.2, the temporal evolution of the Saharan dust event in 2018 and the feedback for regions A and B are presented. Due to the large size of the simulation area, there are different influences acting on certain areas. Therefore, it is reasonable to examine the temporal evolution in smaller regions. For the sake of completeness, this section briefly discusses the temporal development averaged over the entire simulation area.

Fig. A.1 shows the evolution of the mean ensemble differences (lines) and respective standard deviations (shading) of diffuse surface albedo, snow height, surface temperature, 2m-temperature, shortwave radiation net flux on the snow surfaces, and the overall cloud cover between SDS and REF during the whole simulation. The decrease in snow albedo is constantly present and increases throughout the simulation. There are some strong fluctuations in the mornings and evenings, probably model artifacts. The simulation area is large and covers 80 degrees of longitude. Consequently, the area is partially irradiated by the sun during the transition between day and night. This causes the large fluctuations in the albedo because the model uses dummy values for nighttime hours which are, however, irrelevant for the radiation.

The mean reduction in snow albedo in SDS compared to REF throughout the whole simulation is $-0.21\,\%$. The daily ensemble mean difference increases from day to day, reaching a daily mean reduction of $-0.36\,\%$ in SDS on the last simulation day. The difference in snow height between SDS and REF shows similar behavior, but needs more spin-up time. It takes 80 hours until the decrease in snow height reaches a reduction of $-0.10\,\mathrm{mm}$ in SDS. The differences between SDS and REF grow further until the mean difference reaches $-1.00\,\mathrm{mm}$ on March 31, 17 UTC.

The mean surface temperature is higher in SDS throughout the simulation except of the last day. The difference averaged over the whole domain is small with a mean value of 0.01 K and a maximum value of 0.03 K on March 31, 8 UTC. Towards the end of the simulation, there are 5 hours where the mean surface temperature of SDS drops below REF. The 2m-temperature shows a similar behavior as the surface temperature. It fluctuates over the whole simulation showing only very small differences between SDS and REF averaged over the whole domain. The mean difference is even smaller compared to the surface temperature with a mean difference of 0.01 K and a maximum value of 0.02 K in SDS.

The difference in shortwave net flux shows an increase in SDS during daytime, starting from the first simulation day. The daily difference between the scenarios enlarges over time with a mean of $0.26\,\mathrm{W\,m^{-2}}$ and a maximum of $1.64\,\mathrm{W\,m^{-2}}$ on March 31, 10 UTC, again on the last simulation day. The eighth simulation day (March 29) has a similar daily maximum difference in shortwave net flux of $1.60\,\mathrm{W\,m^{-2}}$. However, the ninth day (March 30) shows a reduced difference with daily maximum of only $1.04\,\mathrm{W\,m^{-2}}$ despite a comparable difference in snow albedo. This indicates that on March 30, the atmospheric

conditions have changed and other signals interfere with the albedo effect. The cloud coverage shows barely a difference between SDS and REF with a mean value of 0.01 % and a constant fluctuation around zero.

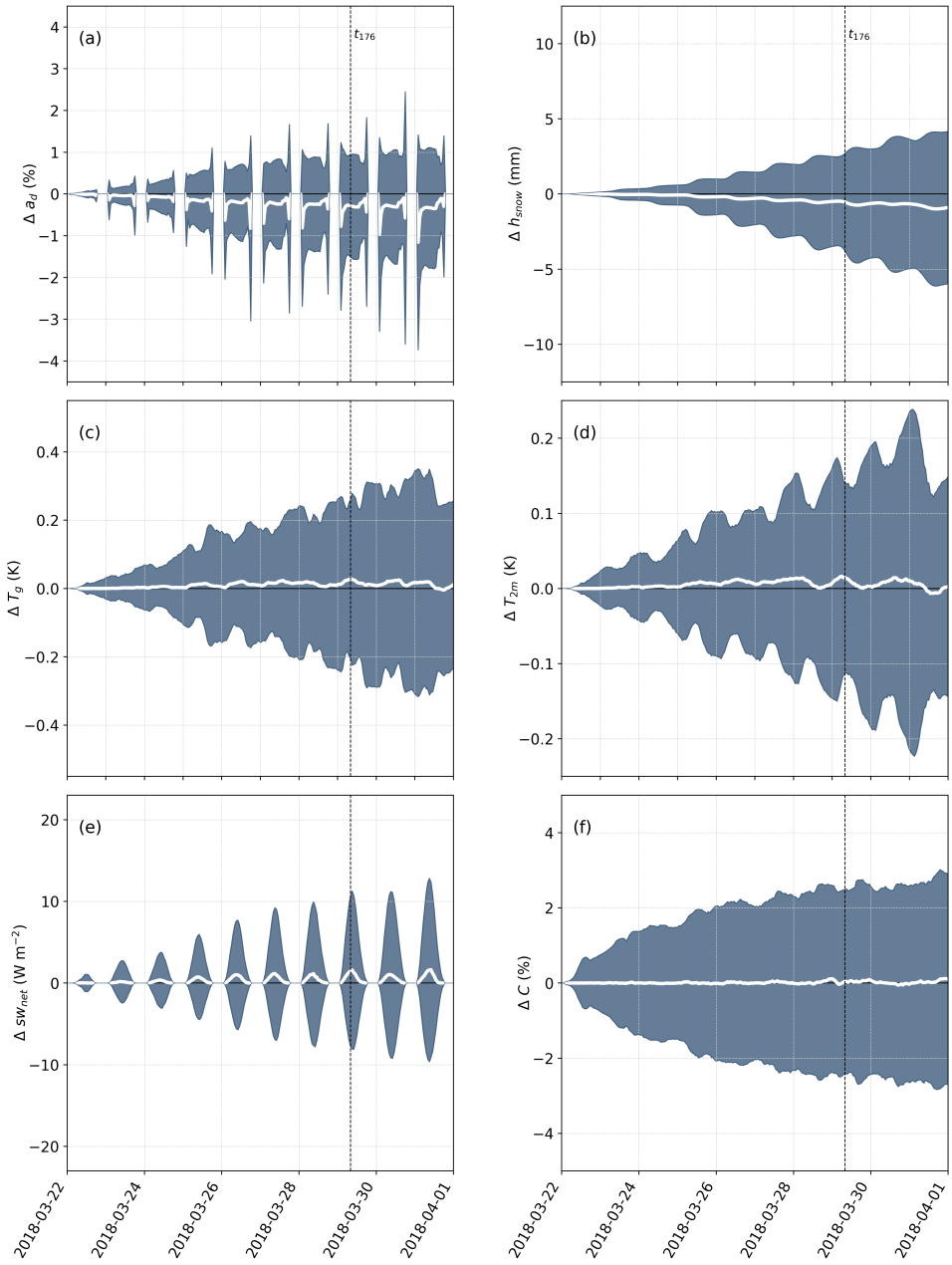

Figure A.1: Hourly ensemble mean differences (lines) and respective standard deviations (shading) of diffuse snow albedo a_d (a), snow height h_{snow} (b), surface temperature T_g (c), 2m-temperature T_{2m} (d), net shortwave radiation flux at surface sw_{net} between SDS and REF on snow covered surfaces (e) and mean difference and respective standard deviation of cloud cover C across the whole domain (f).

B Supplementary Figures: Density plots of the Feedback in Region A and B

This section provides additional figures on the relationship between the difference in albedo between SDS and REF and the feedbacks in the land surface and atmosphere. In section 5.4.1, this relationship was presented for the entire simulation area. Here the variables are split between regions A and B. Different responses to the disturbance in these areas can be identified, which were already found in the spatial analysis. Fig. B.1 shows the comparison of the dust loading, as well as the differences in the variables snow depth, surface temperature, 2m-temperature, and net shortwave radiation on March 29, 2018, 8 UTC versus the difference in surface albedo. This figure corresponds to Fig. 5.20 but covers only surfaces of region A.

The mean dust loading in the top snow layer is $0.90\,\mathrm{g\,m^{-2}}$. A relationship can be noted which is not linear. The largest reduction in surface albedo of $-13.42\,\%$ occurs where a dust amount of $1.72\,\mathrm{g\,m^{-2}}$ is apparent, although larger amounts do occur. Surprisingly, despite the general decrease in surface albedo, a decrease as well as an increase in snow depth is apparent in this area. Such cases occur up to a decrease in surface albedo of $-3.75\,\%$. The cells with a greater reduction in albedo are all associated with a decrease in snow depth. The surface temperature, 2m-temperature, and net shortwave radiation flux show similar patterns as already shown in Fig. 5.20. When comparing the change in surface temperature, most of the results are in the second quadrant, just like the 2m-temperature. However, the signal in the latter is not as strong. Even with strong decreases in surface albedo, the signal is much weaker. Regarding the shortwave radiation net flux, a rather linear relationship is apparent. The radiation flux increases with reduction in surface albedo. In the cells with the strongest reduction in shortwave radiation net flux ($-34.95\,\mathrm{W\,m^{-2}}$), only a slight amount of dust is apparent in the top snow layer ($0.07\,\mathrm{g\,m^{-2}}$), and a slight decrease in surface albedo ($-0.18\,\%$). This indicates that the reduction in shortwave radiation net flux are caused by changes in atmospheric conditions rather than in surface properties.

The correlation between the amount of dust and the differences in snow height, surface temperature, 2m-temperature, and shortwave radiation net flux with the difference in diffuse surface albedo between SDS and REF in region B are shown in Fig. B.2. The figure clearly shows that cells with higher amounts of dust are characterized by lower albedo. However, in individual cases the surface albedo can be increased despite dust deposition on snow. This only applies up to a dust amount of $0.8\,\mathrm{g\,m^{-2}}$. Large dust loads ($> 3\,\mathrm{g\,m^{-2}}$) always coincide with reductions in surface albedo. In contrast to region A, more cases appear in the first and fourth quadrants when comparing snow depth and albedo. These results are mainly due to the region northeast of the Black Sea. As already explained by means of Fig. 5.19, the increase of precipitation in SDS affects the snow depth in form of an increase. The surface temperature and the 2m-temperature, however, decrease in this area. This is also evident in the figure, as there are more results in the fourth quadrant. The change in shortwave radiation net flux shows a linear relationship to the change

in albedo in the second quadrant. The stronger the decrease in albedo, the greater the net radiation flux. But the relation in region B scatters more strongly into the other three quadrants.

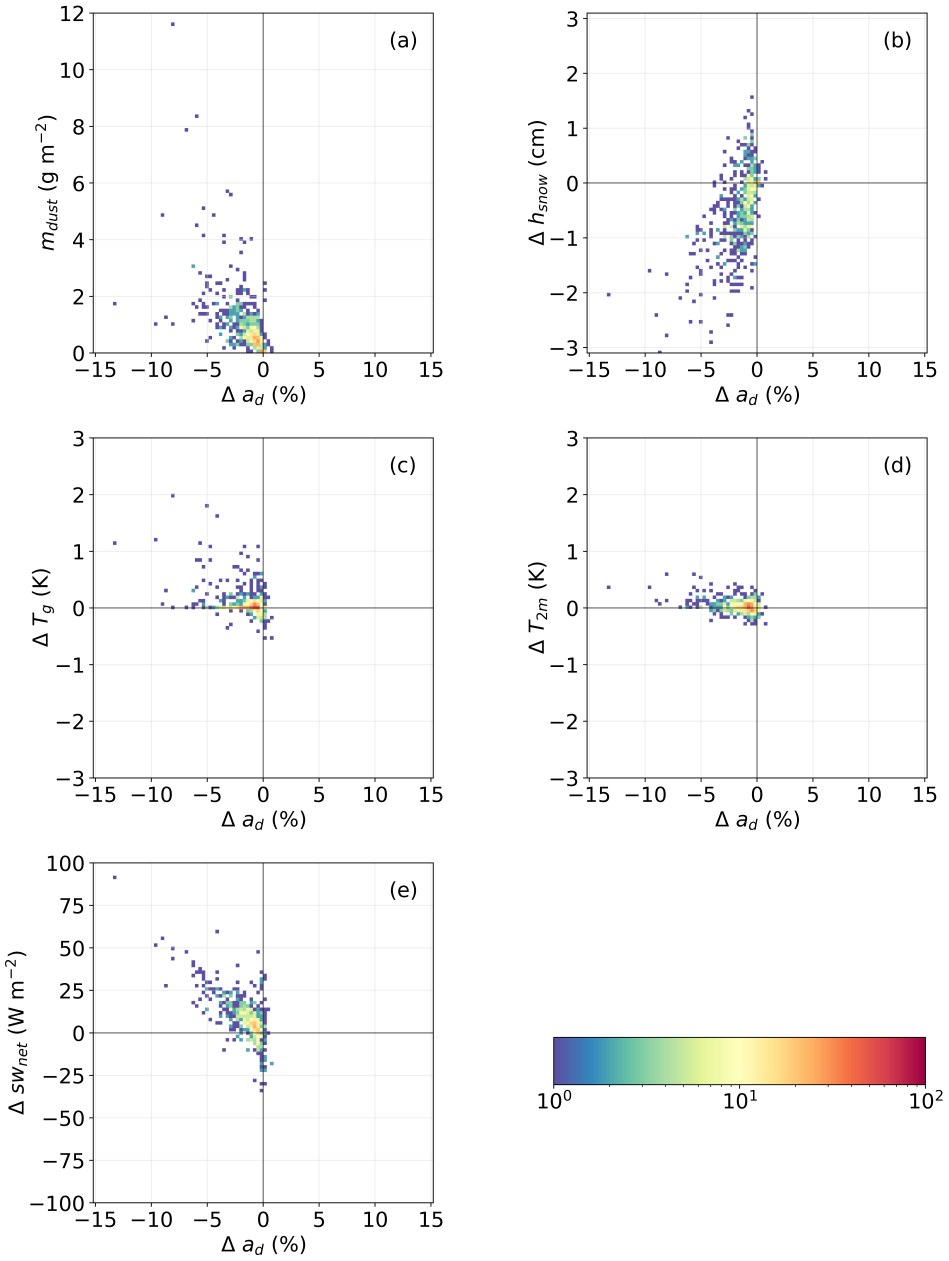

Figure B.1: Density plots of the local ensemble mean dust loading m_{dust} in the top snow layer in SDS (a), the local differences of snow height h_{snow} (b), surface temperature T_g (c), 2m-temperature T_{2m} (d), and shortwave radiation net flux sw_{net} (e) in comparison to the difference in diffuse snow albedo between SDS and REF in region A on March 29, 2018, 8 UTC.

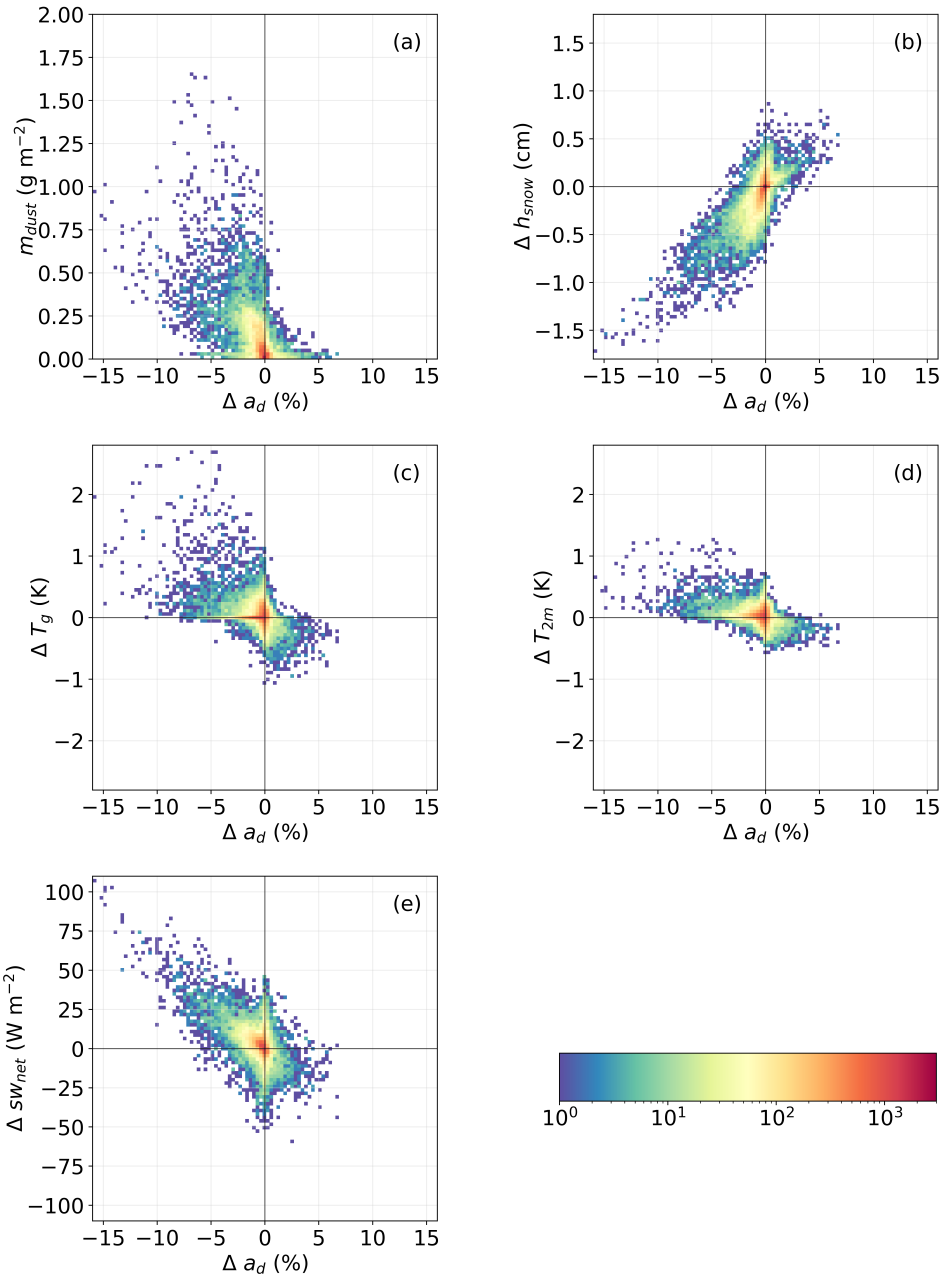

Figure B.2: Density plots of the local ensemble mean dust loading m_{dust} in the top snow layer in SDS (a), the local differences of snow height h_{snow} (b), surface temperature T_g (c), 2m-temperature T_{2m} (d), and shortwave radiation net flux sw_{net} (e) in comparison to the difference in diffuse snow albedo between SDS and REF in region B on March 29, 2018, 8 UTC.

C Supplementary Figures: Statistical Significance in Region A and B

In section 5.4.2 the result of the significance tests across the whole simulation domain is presented. It can be seen that many of the cells do not show statistical significance. Here are enlarged figures corresponding to the regions A and B, for a more detailed view. The significant ensemble mean differences in diffuse surface albedo, surface shortwave net radiation flux, snow height, surface temperature, and 2m-temperature of region A is illustrated in Fig. C.1 and region B in Fig. C.2. The remainder of the cells after the significant test show almost exclusively a decrease in surface albedo. However the amount of significant results are very rare especially when it comes to surface temperature and 2m-temperature in region A. The significant differences in snow height are limited to the mountain slopes in region A and to the eastern snow line of Kazakhstan. The same locations show significant increases in surface shortwave net radiation flux in region A. The changes in surface temperature and 2m-temperature are limited to a thin line along the snow line in region B.

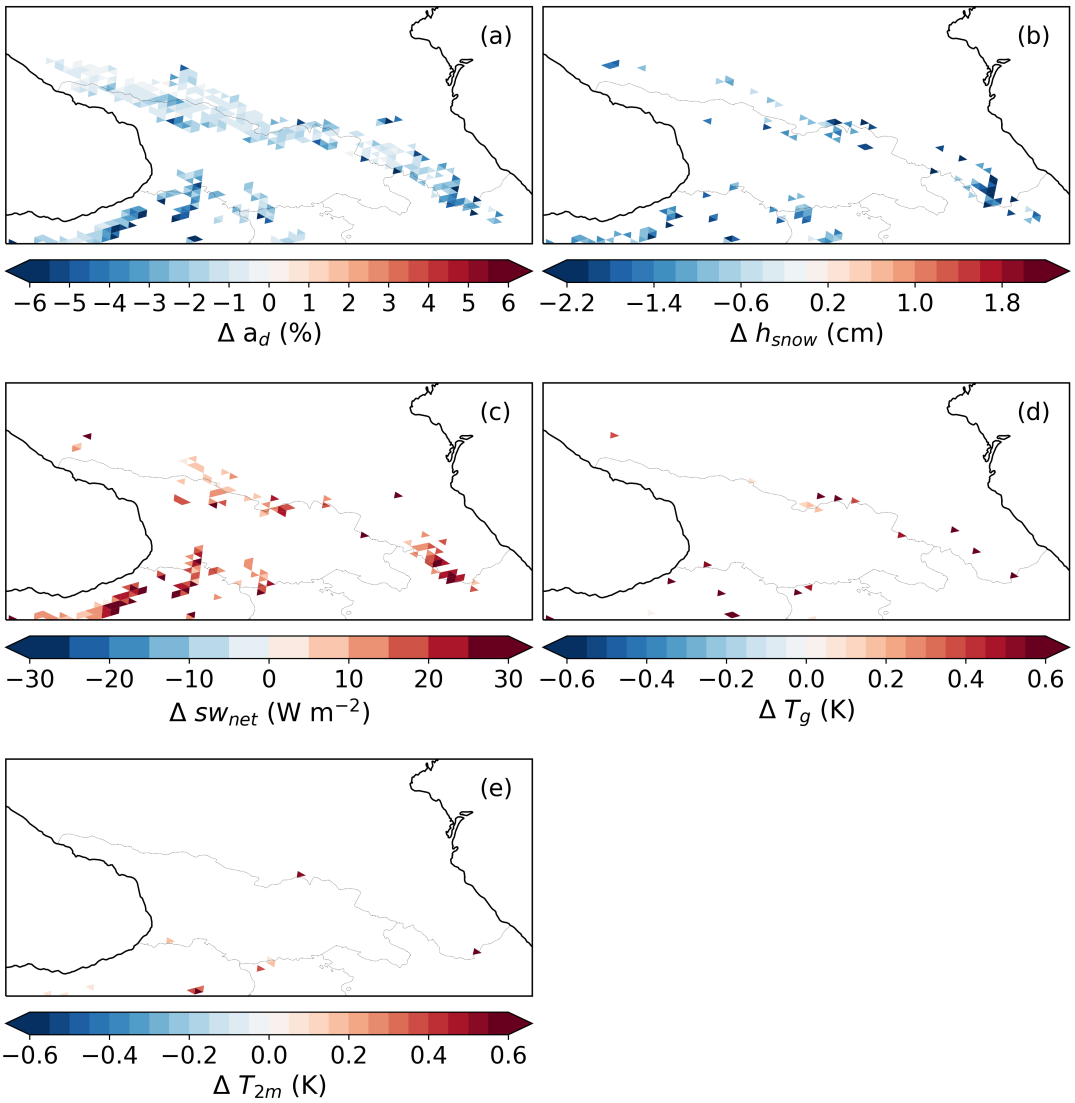

Figure C.1: Significant ensemble mean difference between SDS and REF of diffuse surface albedo a_d (a), surface temperature T_g (b), 2m-temperature T_{2m} (c), and shortwave radiation net flux sw_{net} (d) in region A on March 29, 2018, 8 UTC.

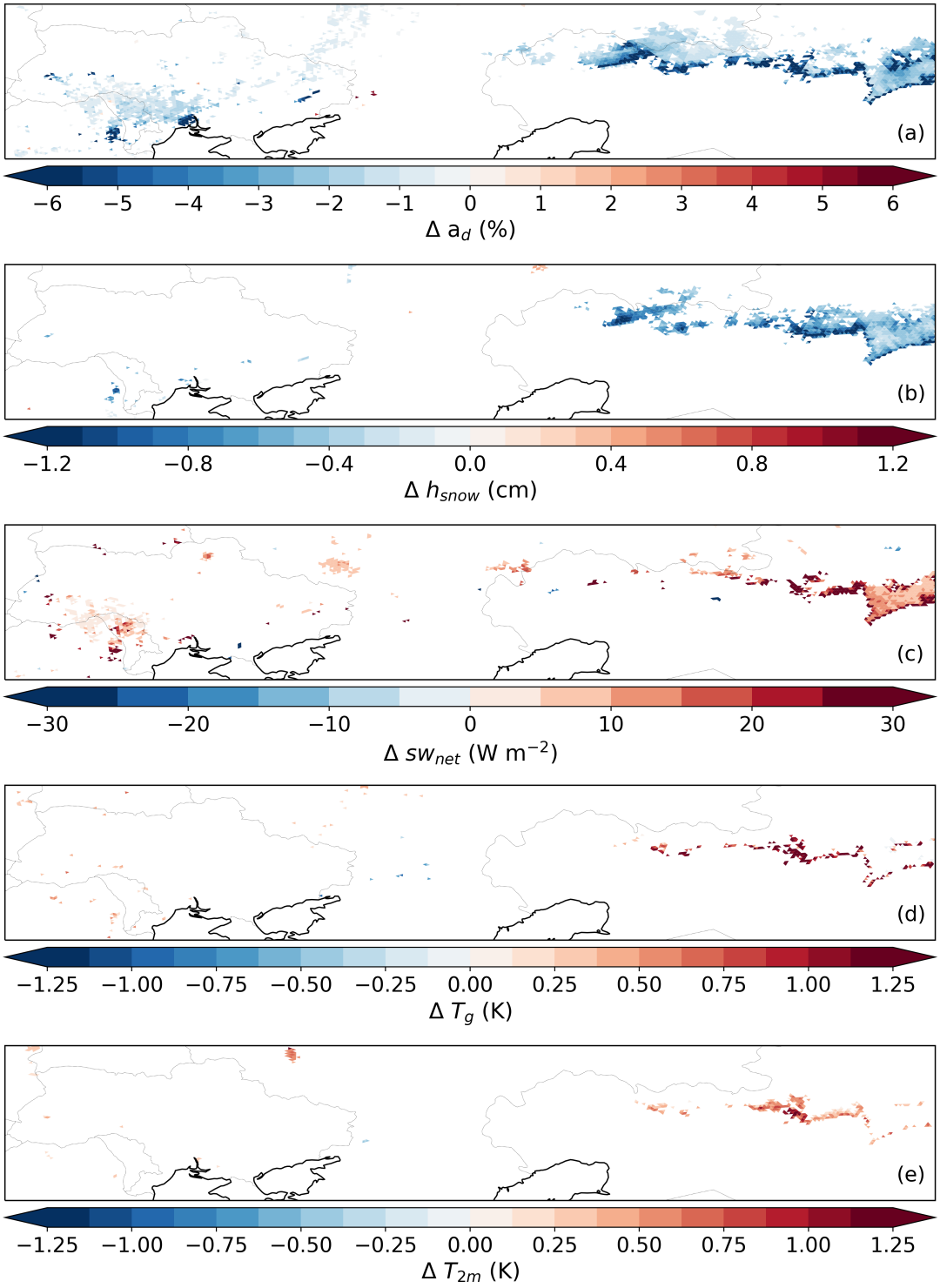

Figure C.2: Significant ensemble mean difference between SDS and REF of diffuse surface albedo a_d (a), surface temperature T_g (b), 2m-temperature T_{2m} (c), and shortwave radiation net flux sw_{net} (d) in region B on March 29, 2018, 8 UTC.

References

Aoki, T., Hachikubo, A., and Hori, M.: Effects of snow physical parameters on shortwave broadband albedos, Journal of Geophysical Research: Atmospheres, 108, 2003.

Aoki, T., Motoyoshi, H., Kodama, Y., Yasunari, T. J., Sugiura, K., and Kobayashi, H.: Atmospheric Aerosol Deposition on Snow Surfaces and Its Effect on Albedo, Scientific Online Letters on the Atmosphere, 2, 13–16, 2006.

Avissar, R. and Pielke, R. A.: A Parameterization of Heterogeneous Land Surfaces for Atmospheric Numerical Models and Its Impact on Regional Meteorology, Monthly Weather Review, 117, 2113–2136, 1989.

Barkan, J. and Alpert, P.: Red snow occurrence in Eastern Europe. A case study, Weather, 75, 45–48, 2020.

Bartelt, P. and Lehning, M.: A physical SNOWPACK model for the Swiss avalanche warning Part I: numerical model, Cold Regions Science and Technology, 35, 123–145, 2002.

Bond, T. C., Doherty, S. J., Fahey, D. W., Forster, P. M., Berntsen, T., DeAngelo, B. J., Flanner, M. G., Ghan, S., Kärcher, B., Koch, D., Kinne, S., Kondo, Y., Quinn, P. K., Sarofim, M. C., Schultz, M. G., Schulz, M., Venkataraman, C., Zhang, H., Zhang, S., Bellouin, N., Guttikunda, S. K., Hopke, P. K., Jacobson, M. Z., Kaiser, J. W., Klimont, Z., Lohmann, U., Schwarz, J. P., Shindell, D., Storelvmo, T., Warren, S. G., and Zender, C. S.: Bounding the role of black carbon in the climate system: A scientific assessment, Journal of Geophysical Research: Atmospheres, 118, 5380–5552, 2013.

Brun, E.: Investigation on Wet-Snow Metamorphism in Respect of Liquid-Water Content, Annals of Glaciology, 13, 22–26, 1989.

Brun, E., David, P., Sudul, M., and Brunot, G.: A numerical model to simulate snow-cover stratigraphy for operational avalanche forecasting, Journal of Glaciology, 38, 13–22, 1992.

Bryant, A. C., Painter, T. H., Deems, J. S., and Bender, S. M.: Impact of dust radiative forcing in snow on accuracy of operational runoff prediction in the Upper Colorado River Basin, Geophysical Research Letters, 40, 3945–3949, 2013.

Carlsen, T., Birnbaum, G., Ehrlich, A., Helm, V., Jäkel, E., Schäfer, M., and Wendisch, M.: Parameterizing anisotropic reflectance of snow surfaces from airborne digital camera observations in Antarctica, The Cryosphere, 14, 3959–3978, 2020.

Colbeck, S.: A review of the metamorphism and classification of seasonal snow cover crystals, IAHS Publication, 162, 3–24, 1987.

Dang, C., Fu, Q., and Warren, S. G.: Effect of Snow Grain Shape on Snow Albedo, Journal of the Atmospheric Sciences, 73, 3573–3583, 2016.

Deems, J. S., Painter, T. H., Barsugli, J. J., Belnap, J., and Udall, B.: Combined impacts of current and future dust deposition and regional warming on Colorado River Basin snow dynamics and hydrology, Hydrology and Earth System Sciences, 17, 4401–4413, 2013.

Di Mauro, B., Fava, F., Ferrero, L., Garzonio, R., Baccolo, G., Delmonte, B., and Colombo, R.: Mineral dust impact on snow radiative properties in the European Alps combining ground, UAV, and satellite observations, Journal of Geophysical Research: Atmospheres, 120, 6080–6097, 2015.

Di Mauro, B., Garzonio, R., Rossini, M., Filippa, G., Pogliotti, P., Galvagno, M., Morra di Cella, U., Migliavacca, M., Baccolo, G., Clemenza, M., Delmonte, B., Maggi, V., Dumont, M., Tuzet, F., Lafaysse, M., Morin, S., Cremonese, E., and Colombo, R.: Saharan dust events in the European Alps: role in snowmelt and geochemical characterization, The Cryosphere, 13, 1147–1165, 2019.

Doherty, S. J., Warren, S. G., Grenfell, T. C., Clarke, A. D., and Brandt, R. E.: Light-absorbing impurities in Arctic snow, Atmospheric Chemistry and Physics, 10, 11 647–11 680, 2010.

Domine, F., Cabanes, A., Taillandier, A. S., and Legagneux, L.: Specific surface area of snow samples determined by CH4 adsorption at 77 K and estimated by optical, microscopy and scanning electron microscopy, Environmental Science & Technology, 35, 771–780, 2001.

Domine, F., Lauzier, T., Cabanes, A., Legagneux, L., Kuhs, W. F., Techmer, K., and Heinrichs, T.: Snow metamorphism as revealed by scanning electron microscopy, Microscopy Research and Technique, 62, 33–48, 2003.

Domine, F., Taillandier, A. S., and Simpson, W. R.: A parameterization of the specific surface area of seasonal snow for field use and for models of snowpack evolution, Journal of Geophysical Research: Earth Surface, 112, 2007.

Doms, G., Förstner, J., Heise, E., Herzog, H., Mironov, D., Raschendorfer, M., Reinhardt, T., Ritter, B., Schrodin, R., Schulz, J.-P., et al.: A description of the nonhydrostatic regional COSMO model. Part II: Physical parameterization, Deutscher Wetterdienst, Offenbach, Germany, 2018, (available at http://www.cosmo-model.org/content/model/documentation/core/default.htm).

Donth, T., Jäkel, E., Ehrlich, A., Heinold, B., Schacht, J., Herber, A., Zanatta, M., and Wendisch, M.: Combining atmospheric and snow radiative transfer models to assess the solar radiative effects of black carbon in the Arctic, Atmospheric Chemistry and Physics, 20, 8139–8156, 2020.

Dumont, M., Brun, E., Picard, G., Michou, M., Libois, Q., Petit, J. R., Geyer, M., Morin, S., and Josse, B.: Contribution of light-absorbing impurities in snow to Greenland's darkening since 2009, Nature Geoscience, 7, 509–512, 2014.

Dumont, M., Tuzet, F., Gascoin, S., Picard, G., Kutuzov, S., Lafaysse, M., Cluzet, B., Nheili, R., and Painter, T. H.: Accelerated Snow Melt in the Russian Caucasus Mountains After the Saharan Dust

Outbreak in March 2018, Journal of Geophysical Research: Earth Surface, 125, e2020JF005 641, 2020.

Ebner, P. P., Schneebeli, M., and Steinfeld, A.: Metamorphism during temperature gradient with undersaturated advective airflow in a snow sample, Cryosphere, 10, 791–797, 2016.

Essery, R., Best, M., and Cox, P.: MOSES 2.2 Technical Documentation, Report, Hadley Centre, Met Office, 2001.

Flanner, M. G. and Zender, C. S.: Snowpack radiative heating: Influence on Tibetan Plateau climate, Geophysical Research Letters, 32, 2005.

Flanner, M. G. and Zender, C. S.: Linking snowpack microphysics and albedo evolution, Journal of Geophysical Research: Atmospheres, 111, 2006.

Flanner, M. G., Zender, C. S., Randerson, J. T., and Rasch, P. J.: Present-day climate forcing and response from black carbon in snow, Journal of Geophysical Research: Atmospheres, 112, 2007.

Flanner, M. G., Zender, C. S., Hess, P. G., Mahowald, N. M., Painter, T. H., Ramanathan, V., and Rasch, P.: Springtime warming and reduced snow cover from carbonaceous particles, Atmospheric Chemistry and Physics, 9, 2481–2497, 2009.

Flanner, M. G., Liu, X., Zhou, C., Penner, J. E., and Jiao, C.: Enhanced solar energy absorption by internally-mixed black carbon in snow grains, Atmospheric Chemistry and Physics, 12, 4699–4721, 2012.

Freese, D. and Kottmeier, C.: Radiation Exchange Between Stratus Clouds and Polar Marine Surfaces, Boundary-Layer Meteorology, 87, 331–356, 1998.

Fujita, K.: Effect of dust event timing on glacier runoff: sensitivity analysis for a Tibetan glacier, Hydrological Processes, 21, 2892–2896, 2007.

Gabbi, J., Huss, M., Bauder, A., Cao, F., and Schwikowski, M.: The impact of Saharan dust and black carbon on albedo and long-term mass balance of an Alpine glacier, The Cryosphere, 9, 1385–1400, 2015.

Gallet, J. C., Domine, F., Zender, C. S., and Picard, G.: Measurement of the specific surface area of snow using infrared reflectance in an integrating sphere at 1310 and 1550 nm, The Cryosphere, 3, 167–182, 2009.

Gardner, A. S. and Sharp, M. J.: A review of snow and ice albedo and the development of a new physically based broadband albedo parameterization, Journal of Geophysical Research: Earth Surface, 115, 2010.

Gautam, R., Hsu, N. C., Lau, W. K. M., and Yasunari, T. J.: Satellite observations of desert dust-induced Himalayan snow darkening, Geophysical Research Letters, 40, 988–993, 2013.

Giorgetta, M. A., Brokopf, R., Crueger, T., Esch, M., Fiedler, S., Helmert, J., Hohenegger, C., Kornblueh, L., Kohler, M., Manzini, E., Mauritsen, T., Nam, C., Raddatz, T., Rast, S., Reinert, D., Sakradzija, M., Schmidt, H., Schneck, R., Schnur, R., Silvers, L., Wan, H., Zangl, G., and Stevens, B.: ICON-A, the Atmosphere Component of the ICON Earth System Model: I. Model Description, Journal of Advances in Modeling Earth Systems, 10, 1613–1637, 2018.

Grenfell, T. C., Perovich, D. K., and Ogren, J. A.: Spectral albedos of an alpine snowpack, Cold Regions Science and Technology, 4, 121–127, 1981.

Hagenmuller, P., Flin, F., Dumont, M., Tuzet, F., Peinke, I., Lapalus, P., Dufour, A., Roulle, J., Pezard, L., Voisin, D., Ando, E., du Roscoat, S. R., and Charrier, P.: Motion of dust particles in dry snow under temperature gradient metamorphism, Cryosphere, 13, 2345–2359, 2019.

Hansen, J.: Efficacy of climate forcings, Journal of Geophysical Research: Atmospheres, 110, 2005.

Hansen, J. and Nazarenko, L.: Soot climate forcing via snow and ice albedos, Proceedings of the National Academy of Sciences of the United States of America, 101, 423–428, 2004.

He, C., Liou, K.-N., Takano, Y., Chen, F., and Barlage, M.: Enhanced Snow Absorption and Albedo Reduction by Dust-Snow Internal Mixing: Modeling and Parameterization, Journal of Advances in Modeling Earth Systems, 11, 3755–3776, 2019.

Heintzenberg, J. and Rummukainen, M.: Airborne particles in snow, Journal of Glaciology, 39, 239–244, 2017.

Hoff, J. T., Gregor, D., Mackay, D., Wania, F., and Jia, C. Q.: Measurement of the specific surface area of snow with the nitrogen adsorption technique, Environmental Science & Technology, 32, 58–62, 1998.

Hoshyaripour, G. A., Bachmann, V., Förstner, J., Steiner, A., Vogel, H., Wagner, F., Walter, C., and Vogel, B.: Effects of Particle Nonsphericity on Dust Optical Properties in a Forecast System: Implications for Model-Observation Comparison, Journal of Geophysical Research: Atmospheres, 124, 7164–7178, 2019.

Jacobi, H. W., Lim, S., Ménégoz, M., Ginot, P., Laj, P., Bonasoni, P., Stocchi, P., Marinoni, A., and Arnaud, Y.: Black carbon in snow in the upper Himalayan Khumbu Valley, Nepal: observations and modeling of the impact on snow albedo, melting, and radiative forcing, The Cryosphere, 9, 1685–1699, 2015.

Jacobi, H.-W., Obleitner, F., Da Costa, S., Ginot, P., Eleftheriadis, K., Aas, W., and Zanatta, M.: Deposition of ionic species and black carbon to the Arctic snowpack: combining snow pit observations with modeling, Atmospheric Chemistry and Physics, 19, 10 361–10 377, 2019.

Jacobson, M. Z.: Climate response of fossil fuel and biofuel soot, accounting for soot's feedback to snow and sea ice albedo and emissivity, Journal of Geophysical Research: Atmospheres, 109, 2004.

Kaempfer, T. U. and Schneebeli, M.: Observation of isothermal metamorphism of new snow and interpretation as a sintering process, Journal of Geophysical Research: Atmospheres, 112, 2007.

Kaspari, S., Painter, T. H., Gysel, M., Skiles, S. M., and Schwikowski, M.: Seasonal and elevational variations of black carbon and dust in snow and ice in the Solu-Khumbu, Nepal and estimated radiative forcings, Atmospheric Chemistry and Physics, 14, 8089–8103, 2014.

Key, J. R. and Schweiger, A. J.: Tools for atmospheric radiative transfer: Streamer and FluxNet, Computers & Geosciences, 24, 443–451, 1998.

Kokhanovsky, A. A. and Breon, F. M.: Validation of an Analytical Snow BRDF Model Using PARASOL Multi-Angular and Multispectral Observations, IEEE Geoscience and Remote Sensing Letters, 9, 928–932, 2012.

Kuhn, M., Nickus, U., Pichlmayer, F., Blochberger, K., Staudinger, M., Schöner, W., Puxbaum, H., and Böhm, R.: High Alpine Snow Pack Chemistry, pp. 203–224, Springer Berlin Heidelberg, Berlin, Heidelberg, 1997.

Kutuzov, S., Shahgedanova, M., Mikhalenko, V., Ginot, P., Lavrentiev, I., and Kemp, S.: High-resolution provenance of desert dust deposited on Mt. Elbrus, Caucasus in 2009-2012 using snow pit and firn core records, The Cryosphere, 7, 1481–1498, 2013.

Lafaysse, M., Cluzet, B., Dumont, M., Lejeune, Y., Vionnet, V., and Morin, S.: A multiphysical ensemble system of numerical snow modelling, The Cryosphere, 11, 1173–1198, 2017.

Lau, W. K. M., Sang, J., Kim, M. K., Kim, K. M., Koster, R. D., and Yasunari, T. J.: Impacts of Snow Darkening by Deposition of Light-Absorbing Aerosols on Hydroclimate of Eurasia During Boreal Spring and Summer, Journal of Geophysical Research: Atmospheres, 123, 8441–8461, 2018.

Lee, W.-L., Liou, K. N., He, C., Liang, H.-C., Wang, T.-C., Li, Q., Liu, Z., and Yue, Q.: Impact of absorbing aerosol deposition on snow albedo reduction over the southern Tibetan plateau based on satellite observations, Theoretical and Applied Climatology, 129, 1373–1382, 2016.

Legagneux, L., Cabanes, A., and Dominé, F.: Measurement of the specific surface area of 176 snow samples using methane adsorption at 77 K, Journal of Geophysical Research: Atmospheres, 107, 2002.

Lehning, M., Bartelt, P., Brown, B., Russi, T., Stockli, U., and Zimmerli, M.: SNOWPACK model calculations for avalanche warning based upon a new network of weather and snow stations, Cold Regions Science and Technology, 30, 145–157, 1999.

Lehning, M., Bartelt, P., Brown, B., and Fierz, C.: A physical SNOWPACK model for the Swiss avalanche warning Part III: meteorological forcing, thin layer formation and evaluation, Cold Regions Science and Technology, 35, 169–184, 2002a.

Lehning, M., Bartelt, P., Brown, B., Fierz, C., and Satyawali, P.: A physical SNOWPACK model for the Swiss avalanche warning Part II: Snow microstructure, Cold Regions Science and Technology, 35, 147–167, 2002b.

Li, X., Kang, S., He, X., Qu, B., Tripathee, L., Jing, Z., Paudyal, R., Li, Y., Zhang, Y., Yan, F., Li, G., and Li, C.: Light-absorbing impurities accelerate glacier melt in the Central Tibetan Plateau, Science of The Total Environment, 587-588, 482–490, 2017.

Libois, Q., Picard, G., France, J. L., Arnaud, L., Dumont, M., Carmagnola, C. M., and King, M. D.: Influence of grain shape on light penetration in snow, The Cryosphere, 7, 1803–1818, 2013.

Linow, S., Hörhold, M. W., and Freitag, J.: Grain-size evolution of polar firn: a new empirical grain growth parameterization based on X-ray microcomputer tomography measurements, Journal of Glaciology, 58, 1245–1252, 2017.

Machulskaya, E. E. and Lykosov, V. N.: An advanced snow parameterization for models of atmospheric circulation, COSMO Newsletter, 8, 10–16, 2008.

Marmureanu, L., Marin, C. A., Andrei, S., Antonescu, B., Ene, D., Boldeanu, M., Vasilescu, J., Vitelaru, C., Cadar, O., and Levei, E.: Orange Snow-A Saharan Dust Intrusion over Romania During Winter Conditions, Remote Sensing, 11, 2019.

Meinander, O., Kazadzis, S., Arola, A., Riihelä, A., Räisänen, P., Kivi, R., Kontu, A., Kouznetsov, R., Sofiev, M., Svensson, J., Suokanerva, H., Aaltonen, V., Manninen, T., Roujean, J. L., and Hautecoeur, O.: Spectral albedo of seasonal snow during intensive melt period at Sodankylä, beyond the Arctic Circle, Atmospheric Chemistry and Physics, 13, 3793–3810, 2013.

Mie, G.: Beiträge zur Optik trüber Medien, speziell kolloidaler Metallösungen, Annalen der Physik, 330, 377–445, 1908.

Mlawer, E. J., Taubman, S. J., Brown, P. D., Iacono, M. J., and Clough, S. A.: Radiative transfer for inhomogeneous atmospheres: RRTM, a validated correlated-k model for the longwave, Journal of Geophysical Research: Atmospheres, 102, 16 663–16 682, 1997.

Morcrette, J. J., Barker, H. W., Cole, J. N. S., Iacono, M. J., and Pincus, R.: Impact of a New Radiation Package, McRad, in the ECMWF Integrated Forecasting System, Monthly Weather Review, 136, 4773–4798, 2008.

Nagorski, S. A., Kaspari, S. D., Hood, E., Fellman, J. B., and Skiles, S. M.: Radiative Forcing by Dust and Black Carbon on the Juneau Icefield, Alaska, Journal of Geophysical Research: Atmospheres, 124, 3943–3959, 2019.

Nakoudi, K., Ritter, C., Böckmann, C., Kunkel, D., Eppers, O., Rozanov, V., Mei, L., Pefanis, V., Jäkel, E., Herber, A., Maturilli, M., and Neuber, R.: Does the Intra-Arctic Modification of Long-Range Transported Aerosol Affect the Local Radiative Budget? (A Case Study), Remote Sensing, 12, 2020.

Narita, H.: Measurement of the specific surface of the deposited snow. II, Low Temperature Science, Series A, 29, 69–79, 1971.

Negi, H. S., Singh, S. K., Kulkarni, A. V., and Semwal, B. S.: Field-based spectral reflectance measurements of seasonal snow cover in the Indian Himalaya, International Journal of Remote Sensing, 31, 2393–2417, 2010.

O'Brien, H. W. and Munis, R. H.: Red and near-infrared spectral reflectance of snow, vol. 332, Corps of Engineers, US Army, Cold Regions Research and Engineering Laboratory, 1975.

Painter, T. H., Deems, J. S., Belnap, J., Hamlet, A. F., Landry, C. C., and Udall, B.: Response of Colorado River runoff to dust radiative forcing in snow, Proceedings of the National Academy of Sciences of the United States of America, 107, 17 125–17 130, 2010.

Peltoniemi, J. I., Gritsevich, M., Hakala, T., Dagsson-Waldhauserová, P., Arnalds, O., Anttila, K., Hannula, H. R., Kivekäs, N., Lihavainen, H., Meinander, O., Svensson, J., Virkkula, A., and de Leeuw, G.: Soot on Snow experiment: bidirectional reflectance factor measurements of contaminated snow, The Cryosphere, 9, 2323–2337, 2015.

Pinzer, B. R. and Schneebeli, M.: Snow metamorphism under alternating temperature gradients: Morphology and recrystallization in surface snow, Geophysical Research Letters, 36, 2009.

Qian, Y., Gustafson, W. I., Leung, L. R., and Ghan, S. J.: Effects of soot-induced snow albedo change on snowpack and hydrological cycle in western United States based on Weather Research and Forecasting chemistry and regional climate simulations, Journal of Geophysical Research: Atmospheres, 114, 2009.

Rahimi, S., Liu, X., Zhao, C., Lu, Z., and Lebo, Z. J.: Examining the atmospheric radiative and snow-darkening effects of black carbon and dust across the Rocky Mountains of the United States using WRF-Chem, Atmospheric Chemistry and Physics, 20, 10 911–10 935, 2020.

Rieger, D., Bangert, M., Bischoff-Gauss, I., Förstner, J., Lundgren, K., Reinert, D., Schröter, J., Vogel, H., Zängl, G., Ruhnke, R., and Vogel, B.: ICON–ART 1.0 – a new online-coupled model system from the global to regional scale, Geoscientific Model Development, 8, 1659–1676, 2015.

Riemer, N.: Numerische Simulationen zur Wirkung des Aerosols auf die troposphärische Chemie und die Sichtweite, Ph.D. thesis, Institut für Meteorologie und Klimaforschung der Universität Karlsruhe, fak. f. Physik, Diss. v. 15.2.2002 und Karlsruhe 2002. (Wissenschaftliche Berichte des Instituts für Meteorologie und Klimaforschung der Universität Karlsruhe. 29.), 2002.

Rinke, R.: Parametrisierung des Auswaschens von Aerosolpartikeln durch Niederschlag, Ph.D. thesis, Institut für Meteorologie und Klimaforschung der Universität Karlsruhe, 2008.

Sarangi, C., Qian, Y., Rittger, K., Bormann, K. J., Liu, Y., Wang, H., Wan, H., Lin, G., and Painter, T. H.: Impact of light-absorbing particles on snow albedo darkening and associated radiative forcing over high-mountain Asia: high-resolution WRF-Chem modeling and new satellite observations, Atmospheric Chemistry and Physics, 19, 7105–7128, 2019.

Sarangi, C., Qian, Y., Rittger, K., Ruby Leung, L., Chand, D., Bormann, K. J., and Painter, T. H.: Dust dominates high-altitude snow darkening and melt over high-mountain Asia, Nature Climate Change, 10, 1045–1051, 2020.

Schneebeli, M. and Sokratov, S. A.: Tomography of temperature gradient metamorphism of snow and associated changes in heat conductivity, Hydrological Processes, 18, 3655–3665, 2004.

Schröter, J., Rieger, D., Stassen, C., Vogel, H., Weimer, M., Werchner, S., Forstner, J., Pril, F., Reinert, D., Zangl, G., Giorgetta, M., Ruhnke, R., Vogel, B., and Braesicke, P.: ICON-ART 2.1: a flexible tracer framework and its application for composition studies in numerical weather forecasting and climate simulations, Geoscientific Model Development, 11, 4043–4068, 2018.

Shi, T., Cui, J., Chen, Y., Zhou, Y., Pu, W., Xu, X., Chen, Q., Zhang, X., and Wang, X.: Enhanced light absorption and reduced snow albedo due to internally mixed mineral dust in grains of snow, Atmospheric Chemistry and Physics, 21, 6035–6051, 2021.

Skeie, R. B., Berntsen, T., Myhre, G., Pedersen, C. A., Ström, J., Gerland, S., and Ogren, J. A.: Black carbon in the atmosphere and snow, from pre-industrial times until present, Atmospheric Chemistry and Physics, 11, 6809–6836, 2011.

Skiles, S. M. and Painter, T. H.: Assessment of Radiative Forcing by Light-Absorbing Particles in Snow from In Situ Observations with Radiative Transfer Modeling, Journal of Hydrometeorology, 19, 1397–1409, 2018.

Skiles, S. M. and Painter, T. H.: Toward Understanding Direct Absorption and Grain Size Feedbacks by Dust Radiative Forcing in Snow With Coupled Snow Physical and Radiative Transfer Modeling, Water Resources Research, 55, 7362–7378, 2019.

Skiles, S. M., Painter, T. H., Belnap, J., Holland, L., Reynolds, R. L., Goldstein, H. L., and Lin, J.: Regional variability in dust-on-snow processes and impacts in the Upper Colorado River Basin, Hydrological Processes, 29, 5397–5413, 2015.

Skiles, S. M., Flanner, M., Cook, J. M., Dumont, M., and Painter, T. H.: Radiative forcing by light-absorbing particles in snow, Nature Climate Change, 8, 964–971, 2018a.

Skiles, S. M., Mallia, D. V., Hallar, A. G., Lin, J. C., Lambert, A., Petersen, R., and Clark, S.: Implications of a shrinking Great Salt Lake for dust on snow deposition in the Wasatch Mountains, UT, as informed by a source to sink case study from the 13-14 April 2017 dust event, Environmental Research Letters, 13, 2018b.

Slaughter, A. E., Adams, E. E., Staron, P. J., Shertzer, R. H., Walters, D. J., McCabe, D., Catherine, D., Henninger, I., Leonard, T., Cooperstein, M., and Munter, H.: Field investigation of near-surface metamorphism of snow, Journal of Glaciology, 57, 441–452, 2011.

Solomos, S., Kalivitis, N., Mihalopoulos, N., Amiridis, V., Kouvarakis, G., Gkikas, A., Binietoglou, I., Tsekeri, A., Kazadzis, S., Kottas, M., Pradhan, Y., Proestakis, E., Nastos, P., and Marenco, F.:

From Tropospheric Folding to Khamsin and Foehn Winds: How Atmospheric Dynamics Advanced a Record-Breaking Dust Episode in Crete, Atmosphere, 9, 2018.

Sommerfeld, R. and LaChapelle, E.: The Classification of snow Metamorphism, Journal of Glaciology, 9, 3–18, 1970.

Svensson, J., Virkkula, A., Meinander, O., Kivekas, N., Hannula, H. R., Jarvinen, O., Peltoniemi, J. I., Gritsevich, M., Heikkila, A., Kontu, A., Neitola, K., Brus, D., Dagsson-Waldhauserova, P., Anttila, K., Vehkamaki, M., Hienola, A., de Leeuw, G., and Lihavainen, H.: Soot-doped natural snow and its albedo - results from field experiments, Boreal Environment Research, 21, 481–503, 2016.

Svensson, J., Ström, J., Kivekäs, N., Dkhar, N. B., Tayal, S., Sharma, V. P., Jutila, A., Backman, J., Virkkula, A., Ruppel, M., Hyvärinen, A., Kontu, A., Hannula, H.-R., Leppäranta, M., Hooda, R. K., Korhola, A., Asmi, E., and Lihavainen, H.: Light-absorption of dust and elemental carbon in snow in the Indian Himalayas and the Finnish Arctic, Atmospheric Measurement Techniques, 11, 1403–1416, 2018.

Tuzet, F., Dumont, M., Lafaysse, M., Picard, G., Arnaud, L., Voisin, D., Lejeune, Y., Charrois, L., Nabat, P., and Morin, S.: A multilayer physically based snowpack model simulating direct and indirect radiative impacts of light-absorbing impurities in snow, The Cryosphere, 11, 2633–2653, 2017.

Tuzet, F., Dumont, M., Arnaud, L., Voisin, D., Lamare, M., Larue, F., Revuelto, J., and Picard, G.: Influence of light-absorbing particles on snow spectral irradiance profiles, The Cryosphere, 13, 2169–2187, 2019.

Usha, K. H., Nair, V. S., and Babu, S. S.: Modeling of aerosol induced snow albedo feedbacks over the Himalayas and its implications on regional climate, Climate Dynamics, 54, 4191–4210, 2020.

Vionnet, V., Brun, E., Morin, S., Boone, A., Faroux, S., Le Moigne, P., Martin, E., and Willemet, J. M.: The detailed snowpack scheme Crocus and its implementation in SURFEX v7.2, Geoscientific Model Development, 5, 773–791, 2012.

Vogel, B., Hoose, C., Vogel, H., and Kottmeier, C.: A model of dust transport applied to the Dead Sea Area, Meteorologische Zeitschrift, 15, 611–624, 2006.

Warren, S. G.: Optical-Properties of Snow, Reviews of Geophysics, 20, 67–89, 1982.

Warren, S. G.: Optical constants of ice from the ultraviolet to the microwave, Applied Optics, pp. 1206–1225, 1984.

Warren, S. G.: Can black carbon in snow be detected by remote sensing?, Journal of Geophysical Research: Atmospheres, 118, 779–786, 2013.

Warren, S. G. and Brandt, R. E.: Optical constants of ice from the ultraviolet to the microwave: A revised compilation, Journal of Geophysical Research: Atmospheres, 113, 2008.

Warren, S. G. and Wiscombe, W. J.: A Model for the Spectral Albedo of Snow 2. Snow Containing Atmospheric Aerosols, Journal of the Atmospheric Sciences, 37, 2734–2745, 1980.

White, J. R., Cerveny, R. S., and Balling, R. C.: Seasonality in European Red Dust/"Blood" Rain Events, Bulletin of the American Meteorological Society, 93, 471–476, 2012.

Wilcoxon, F.: Individual Comparisons by Ranking Methods, Biometrics Bulletin, 1, 1945.

Wilks, D. S.: "The Stippling Shows Statistically Significant Grid Points": How Research Results are Routinely Overstated and Overinterpreted, and What to Do about It, Bulletin of the American Meteorological Society, 97, 2263–2273, 2016.

Wiscombe, W. J. and Warren, S. G.: A Model for the Spectral Albedo of Snow 1. Pure Snow, Journal of the Atmospheric Sciences, 37, 2712–2733, 1980.

Wu, L., Gu, Y., Jiang, J. H., Su, H., Yu, N., Zhao, C., Qian, Y., Zhao, B., Liou, K.-N., and Choi, Y.-S.: Impacts of aerosols on seasonal precipitation and snowpack in California based on convection-permitting WRF-Chem simulations, Atmospheric Chemistry and Physics, 18, 5529–5547, 2018.

Xu, B., Cao, J., Hansen, J., Yao, T., Joswia, D. R., Wang, N., Wu, G., Wang, M., Zhao, H., Yang, W., Liu, X., and He, J.: Black soot and the survival of Tibetan glaciers, Proceedings of the National Academy of Sciences of the United States of America, 106, 22 114–22 118, 2009.

Yasunari, T. J., Koster, R. D., Lau, K.-M., Aoki, T., Sud, Y. C., Yamazaki, T., Motoyoshi, H., and Kodama, Y.: Influence of dust and black carbon on the snow albedo in the NASA Goddard Earth Observing System version 5 land surface model, Journal of Geophysical Research: Atmospheres, 116, 2011.

Yasunari, T. J., Tan, Q., Lau, K. M., Bonasoni, P., Marinoni, A., Laj, P., Menegoz, M., Takemura, T., and Chin, M.: Estimated range of black carbon dry deposition and the related snow albedo reduction over Himalayan glaciers during dry pre-monsoon periods, Atmospheric Environment, 78, 259–267, 2013.

Yasunari, T. J., Koster, R. D., Lau, W. K. M., and Kim, K.-M.: Impact of snow darkening via dust, black carbon, and organic carbon on boreal spring climate in the Earth system, Journal of Geophysical Research: Atmospheres, 120, 5485–5503, 2015.

Zängl, G., Reinert, D., Rípodas, P., and Baldauf, M.: The ICON (ICOsahedral Non-hydrostatic) modelling framework of DWD and MPI-M: Description of the non-hydrostatic dynamical core, Quarterly Journal of the Royal Meteorological Society, 141, 563–579, 2015.

Zhang, Y., Kang, S., Sprenger, M., Cong, Z., Gao, T., Li, C., Tao, S., Li, X., Zhong, X., Xu, M., Meng, W., Neupane, B., Qin, X., and Sillanpää, M.: Black carbon and mineral dust in snow cover on the Tibetan Plateau, The Cryosphere, 12, 413–431, 2018.

Zhao, C., Hu, Z., Qian, Y., Ruby Leung, L., Huang, J., Huang, M., Jin, J., Flanner, M. G., Zhang, R., Wang, H., Yan, H., Lu, Z., and Streets, D. G.: Simulating black carbon and dust and their

radiative forcing in seasonal snow: a case study over North China with field campaign measurements, Atmospheric Chemistry and Physics, 14, 11 475–11 491, 2014.

Zhong, E., Li, Q., Sun, S., Chen, W., Chen, S., and Nath, D.: Improvement of a snow albedo parameterization in the Snow–Atmosphere–Soil Transfer model: evaluation of impacts of aerosol on seasonal snow cover, Advances in Atmospheric Sciences, 34, 1333–1345, 2017.

List of Figures

List of Tables

Acronyms

AOD	Aerosol optical depth
ART	Aerosol and Reactive Tracegases
BC	Black carbon
Chem	Chemistry
COSMO	Community Consortium Small-scale Modelling
DWD	German Weather Service
ECMWF	European Centre for Medium-Range Weather Forecasts
FDR	False detection rate
GATOR-GCMOM	Gas, Aerosol, Transport, Radiation, General-Circulation, Mesoscale, and Ocean Model
GEOS-5	Goddard Earth Observing System, Version 5
GISS	Goddard Institute for Space Studies
ICON	ICOsahedral Nonhydrostatic
IFS	Integrated Forecast System
KIT	Karlsruhe Institute of Technology
LAI	Light-absorbing impurities
LAM	Limited Area Mode
LAP	Light-absorbing impurities
LUT	Look-up-table
MODIS	Moderate Resolution Imaging Radiospectrometer
MOSES	Met Office Surface Exchange Scheme
MPI-M	Max Planck Institute for Meteorology
NASA	National Aeronautics and Space Administration
NCAR	National Center for Atmospheric Research
NIR	Near infrared
OC	Organic carbon
PAMARCMiP	Polar Airborne Measurements and Arctic Regional Climate Model Simulation Project

ppm	Parts per million
REF	Reference simulation
RMSE	Root-mean-square error
RRTM	Rapid Radiative Transfer Model
SAF	Snow albedo effect
SDS	Snow-darkening simulation
SNICAR	SNow, ICe, and Aerosol Radiation
SWE	Snow water equivalent
TARTES	Two-stream Analytical Radiative TransfEr in Snow model
UTC	Coordinated Universal Time
VIS	Visible
WRF	Weather Research and Forecasting

Symbols

A_{ice}	Surface area of an ice crystal
$A = 0.23\,10^6\,\mu m^2\,s^{-1}$	Constant
a_d	Diffuse albedo
a_{gr}	Ground albedo
a_s	Direct albedo
$a_{snow,max}$	Maximum of snow albedo
$a_{snow,min}$	Minimum of snow albedo
a^∞	Albedo of a semi-infinite snow layer
a_d^∞	Diffuse albedo of a semi-infinite snow layer
a_s^∞	Direct albedo of a semi-infinite snow layer
a_{snow}	Snow albedo
C	Cloud cover
d_0	Amount of snow fall that sets the optical equivalent snow grain radius to the minimum value
$\overline{d}_{0,l}$	Median diameter of number distribution
$\overline{d}_{3,l}$	Median diameter of mass distribution
d_p	Tracer diameter
dz_{max}	Threshold depth of top snow layer
dzh_{snow}	Depth of snow layer considered in the interaction between snow and mineral dust
$E_{0,l}$	Emission of specific number of a tracer with mode l
$E_{3,l}$	Emission of mass mixing ratio of a tracer with mode l
Ei	Exponential integral
$E = 3700\,J\,mol^{-1}$	Constant
g	Asymmetry parameter
g_i	Asymmetry parameter of component i
g_{mix}	Mixed asymmetry parameter (dust and snow)
G_r	Snow aging growth rate

h_{snow}	Snow height
I	Irradiance at entry of an medium
I_0	Irradiance at exit of an medium
k	Bisections of the ICON triangles
k_e	Mass-specific extinction coefficient
$k_{e,l}$	Mass-specific extinction coefficient for tracer mode l
L	Liquid water in snowpack
l	Tracer mode
M	Mass mixing ratio
M_{ice}	Mass of an ice crystal
M_l	Mass mixing ratio of mode l
m_{dust}	Mineral dust mass in the top snow layer
m_{im}	Imaginary refractive index of ice
m_{re}	Real refractive index of ice
N_i	Number of particle of component i
N_l	Number concentration of mode l
N_{mix}	Number of dust and snow particles
N_{snow}	Amount of optical snow grains
N	Tracer number
N_p	Total amount of p-values
n	Equal sections of the ICON icosahedron edges
P	Precipitation rate
P_{tot}	Total precipitation since model start
p	Probability of obtaining a result in a null hypothesis significance test
p_{def}	Default tuning parameter
p^*_{FDR}	Threshold value
p_{pert}	Perturbed tuning parameter
p_r	Cell specific p-value with rank r of the significance test
Q_{back}	Mie backscatter efficiency
Q_{ext}	Mie extinction efficiency
Q_{sca}	Mie scatter efficiency
$R = 8.314472\,\mathrm{J\,K^{-1}\,mol^{-1}}$	Universal gas constant

R_{pears}	Pearson correlation coefficient
R_{seed}	Random number drawn from a uniform distribution
r	Rank of p-value in the specific cell in comparison of the p-values of all cells
r_0	Minimum of optical equivalent snow grain radius
r_{pert}	Variable specific perturbation threshold
r_{snow}	Optical equivalent snow grain radius
$r_{snow,t-1}$	Optical equivalent snow grain radius of the last time step
S_{age}	Age of snow in top of snow layer
S_f	Snow fall rate
SSA	Specific surface area
SSA_M	Mass specific surface area
SSA_V	Volume specific surface area
sw_{net}	Surface shortwave net radiation flux
t_{176}	Simulation hour 176 (2018-03-29, 8 UTC)
T_{2m}	2m-temperature
T_g	Surface temperature
T_{snow}	Snow temperature
V_{ice}	Volume of an ice crystal
$W_{0,l}$	Loss of specific number of a tracer with mode l
$W_{3,l}$	Loss of mass mixing ratio of a tracer with mode l
x	Dimensionless size parameter
z_{rain}	Rain fall rate
$z_{rain,max}$	Amount of snow fall that sets the optical equivalent snow grain radius to the maximum value
α_{FDR}	Control level of false detection rate
Δt	Timestep
λ	Wavelength
λ_{max}	Maximum wavelength of respective spectral band
λ_{min}	Minimum wavelength of respective spectral band
μ_0	Solar zenith angle
ρ_a	Air density
ρ_{ice}	Density of ice

ρ_{snow}	Density of snow
σ	Standard deviation
σ_l	Standard deviation of a mode l
σ_{ext}	Extinction cross section
$\sigma_{ext,mix}$	Averaged extinction cross section of a snow-dust mixture
$\sigma_{ext,snow}$	Scatter cross section of snow
σ_{sca}	Scatter cross section
$\sigma_{sca,i}$	Scatter cross section of component i
$\sigma_{sca,mix}$	Averaged scatter cross section of a snow-dust mixture
τ_0	Optical depth
υ	Wind velocity
$\upsilon_{sed,0,l}$	Sedimentation velocity of specific number of a tracer with mode l
$\upsilon_{sed,3,l}$	Sedimentation velocity of mass mixing ratio of a tracer with mode l
Ψ	Tracer
$\widehat{\Psi_{0,l}}$	Barycentric mean of specific number of a tracer with mode l
$\widehat{\Psi_{3,l}}$	Barycentric mean of mass mixing ratio of a tracer with mode l
$\widetilde{\omega}$	Single-scattering albedo
$\widetilde{\omega}_{mix}$	Averaged single-scattering albedo of a snow-dust mixture
$\nabla(\overline{\rho_a \upsilon'' \Psi''_{0,l}})$	Turbulent flux of specific number
$\nabla(\overline{\rho_a \upsilon'' \Psi''_{3,l}})$	Turbulent flux of mass mixing ratio
CO_2	Carbon dioxid
CH_4	Methane
CFC-11	Trichlorofluoromethane
CFC-12	Dichlorodifluoromethane
H_2O	Water vapor
N_2O	Nitrous oxide
O_3	Ozone

Acknowledgment

I would like to take this opportunity to thank all the people and institutions that have supported me in completing my dissertation. First of all, I would like to thank Prof. Jan Cermak and Prof. Christoph Kottmeier for supervising my dissertation. Thank you that I could turn to you with questions at any time. The discussions were always fruitful and helpful.
My deepest gratitude goes to Dr. Bernhard Vogel, who always supported and motivated me from day one until the completion of this research project. Your many ideas and suggestions were essential to the completion of this work. Thank you for having my back and constantly encouraging me to explore my own ideas. Thank you for your profound belief in my work and the valuable advice along the way. I would also like to extend my deepest gratitude to Dr. Heike Vogel. You were an invaluable help in learning all the technical aspects of the model, especially when I first started. On the rare occasions that you could not help me straight away, you were always ready to contact the right people and get me some assistance. Also, thanks for getting the initialization and boundary data for my simulations. I am extremely grateful for your assistance and your motivations.

Next, I would like to thank Dr. Evelyn Jäkel from the University of Leipzig. Thank you very much for this wonderful collaboration. Your expertise regarding the snow properties and the related discussions were very helpful to improve the parametrization in the model. Thanks to you I was given the opportunity to do the evaluation of snow aging, as you provided me with the data of the measurements from Greenland. In this regard, many thanks to the community of the DFG funded Transregio project ArctiC Amplification: Climate Relevant Atmospheric and SurfaCe Processes, and Feedback Mechanisms $(AC)^3$. The PAMARCMiP measurement campaign was part of this project. In this context, I would also like to thank Dr. Gerit Birnbaum, who was responsible for the measurements, and Dr. Tobias Donth, who was also involved and explained the details of the measurements to me.
I acknowledge the ICON model community, in particular Dr. Jochen Förster and Dr. Daniel Reinert from the DWD. Thank you for the many hours you spent to help me get over technical obstacles. In addition, I would like to thank Dr. Andrea Steiner (former member of DWD) and Vanessa Bachmann from DWD. Thanks for providing the initialization data of the mineral dust and the help in understanding the technical implementation of the deposition in ICON-ART. Furthermore, I extend my thanks to Ekaterina Machulskaya from DWD, whose experimental multilayer snow model I used as a basis for my developments and who was helpful in answering technical questions in this regard.

Furthermore, I would like to express my sincere thanks to Dr. Ali Hoshyaripour, my former office room mate, moral support and guide in scientific as well as other matters. In particular, you helped me understand how to perform Mie calculations and the technical realization of optical properties in

ICON-ART. Thank you for the great time and your always honest opinions. I would also like to thank a lot Sven Werchner, who selflessly spends a lot of time to take care of technical problems in our group. Thanks a lot for helping me with programming difficulties every now and then. Your willingness to help is admirable and your advice invaluable. I am also extremely grateful to have such a great teammate as Lukas Muser. Thank you Lukas, for accompanying me (almost) the whole way here. Thank you so much for the great time and your support with everything. You have become a good friend to me that I know I can rely on. I am very much looking forward to seeing you at the finish line as well. I would like to thank Julia Bruckert who initiated the discussion of significance analysis and was very helpful in the process. In this sense, I would also like to thank Lisa Muth and Sascha Bierbauer, who also make a great contribution to making the working atmosphere in the group so sincere and productive. I would also like to thank Dr. Philipp Gasch, who has always been helpful with questions about the optical properties of mineral dust in ICON-ART. In addition, I would like to thank the former group members Dr. Konrad Deetz, Dr. Frank Wagner, and Dr. Simon Gruber very much. They always gave me good advice and were always open to questions. Furthermore, I thank Dr. Ingeborg Bischoff-Gauss (formerly with the Steinbuch Centre for Computing), who helped me several times with technical related issues on the high performance computer ForHLR II. Also many thanks to Gabi Klinck, who assisted me with many IT-related matters at the institute.

I acknowledge the Advanced Earth System Modelling Capacity (ESM) community who provided the funding for this research (http://www.esm-project.net). Furthermore, I would like to express my gratitude to the Graduate School for Climate and Environment (GRACE), that provided financial support for the attendance of the 5th Snow Science Winter School in Finland. During this training, I was given the opportunity to learn a lot about my research topic up close and get hands-on experience in measuring snow properties. This brought me closer to the subject and made me enjoy working on it even more. Furthermore, I would like to express a general thank you to all members of the Department Troposphere Research of the Institute of Meteorology and Climate Research (IMK-TRO) at the Karlsruhe Institute of Technology (KIT). I feel fortunate to be a member and have always admired the supportive spirit among the community.

Last but not least, I would like to thank my boyfriend Julian, my brother Michael and my mother Li-Chun, who have always supported and encouraged me to make the best of myself. Without your encouragement, all this would not have been possible.